The Dissertation Committee for Christopher Timothy Curry
certifies that this is the approved version of the following dissertation:

Transport in Higher Dimensional Phase Spaces

Committee:

Philip J. Morrison, Supervisor

Claude Wendell Horton, Jr.

Richard Hazeltine

Richard Matzner

Irene Gamba

Transport in Higher Dimensional Phase Spaces

by

Christopher Timothy Curry, B.S.; M.S. Bioengineering

DISSERTATION
Presented to the Faculty of the Graduate School of
The University of Texas at Austin
in Partial Fulfillment
of the Requirements
for the Degree of

DOCTOR OF PHILOSOPHY

THE UNIVERSITY OF TEXAS AT AUSTIN
December 2016

Acknowledgments

I wish to thank my parents, family, and friends for their love and support over the many, many years. I am especially grateful to my advisor, Phil Morrison, for his guidance and wisdom, and to The University of Texas at Austin and the Department of Physics for financial support.

Transport in Higher Dimensional Phase Spaces

Publication No. ________________

Christopher Timothy Curry, Ph.D.
The University of Texas at Austin, 2016

Supervisor: Philip J. Morrison

We use a four dimensional symplectic mapping, the coupled cubic-quadratic map, to provide evidence of Arnol'd Diffusion in phase space. We use the method of frequency analysis for dynamical systems to demonstrate the existence of regular orbits, and show that these orbits enclose weakly chaotic orbits which escape in finite time around the tori. A new collocation method for frequency analysis is employed by adapting it to allow for higher precision results. Arbitrary precision numerics are used to obtain highly accurate orbits for long timescales, and the adapted frequency method is used to obtain highly accurate frequencies of the mapping. We review the method of frequency analysis, demonstrate its effectiveness and accuracy in determining frequencies and finding tori in simple systems and low-dimensional mappings, and extend the results to higher dimensions. In the four dimensional mapping, we find several regular orbits with irrational frequency ratios, indicating the existence of tori in the phase space, as well as interior orbits that escape around these tori.

Table of Contents

Acknowledgments **iv**

Abstract **v**

List of Tables **ix**

List of Figures **x**

Chapter 1. Preliminaries **1**

- 1.1 Hamiltonian Mechanics 1
- 1.2 The Poincaré Surface of Section 2
- 1.3 The KAM Theory 4
  - 1.3.1 Integrable Systems 4
  - 1.3.2 Action-Angle Variables and Canonical Transformations . 6
  - 1.3.3 Frequencies on the Torus 8
  - 1.3.4 A Note on Integrability 8
  - 1.3.5 The Failure of Classical Canonical Perturbation Theory 10
  - 1.3.6 The Destruction of Tori 12
- 1.4 The Arnol'd Diffusion 13
- 1.5 Symplectic Mappings 14
  - 1.5.1 Symplectic Maps and the Poincaré Surface of Section . . 14
  - 1.5.2 The Standard Map 15
    - 1.5.2.1 Rotation Numbers, Winding Numbers, and the Breakup of Tori 16
  - 1.5.3 Higher Dimensional Symplectic Mappings 24
    - 1.5.3.1 The Froeschlé Map and the Generalized Coupled Standard Mapping 24
    - 1.5.3.2 A Note on Higher Dimensional Poincaré Sections 31

Chapter 2. Stability of Equilibria and Negative Energy Modes 32

2.1 Types of Stability 33
2.2 Negative Energy Modes: Definition and Examples 34
  2.2.1 Cherry's Example: Wave-Wave Resonance 35
  2.2.2 Wave-Wave Problems in Plasma Physics 36
  2.2.3 FLR Stabilization 38

Chapter 3. The Coupled Cubic-Quadratic Mapping 40

3.1 Introduction 40
3.2 Generating the Cubic Map 41
3.3 Generating the Quadratic Map 41
3.4 Generating the Coupled Mapping 42
3.5 The Cubic Map 44
3.6 The Quadratic Map 48
3.7 Generalized Polynomial Mappings 48
3.8 The Geometry of Phase Space 59

Chapter 4. Frequency Analysis and Dynamical Systems 61

4.1 Introduction 61
4.2 The Method of Frequency Analysis 62
4.3 Frequency Analysis of Symplectic Mappings 63
  4.3.1 Area-Preserving Mappings: The Standard Map 63
  4.3.2 Higher Dimensional Mappings 67
    4.3.2.1 The Froeschlé Map 67
    4.3.2.2 The Coupled Cubic-Quadratic Map 67
4.4 Evidence of Arnol'd Diffusion and Generalized Transport Phenomena 70
  4.4.1 Example I 72
  4.4.2 Example II 74
  4.4.3 Regular Orbits 80
4.5 Accuracy and Precision 90
  4.5.1 Shadowing of Orbits 90
  4.5.2 Accuracy and Precision of Frequencies 92

Chapter 5. Visualizing Tori in Higher Dimensions **105**

5.1 Canonical Transformations and Higher Dimensional Symplectic Mappings . . . 105

5.2 Projections of Higher Dimensional Data: Unwinding the Torus 108

5.2.1 The Projection Matrix . . . 110

5.2.2 Unwinding the Torus via a Simple Canonical Transformation . . . 113

5.3 A Higher Dimensional Poincaré Section Method . . . 115

5.4 Discussion: Tori or Not Tori? . . . 119

Chapter 6. Numerical Explorations of Symplectic Mappings **124**

6.1 Escape Times for the Coupled Cubic-Quadratic Mapping . . . 124

6.2 The Escape Mapping: A Fast Tool for Visualizing Dynamics . 124

6.2.1 The Escape Mapping for the Hénon Map . . . 126

6.2.2 The Escape Mapping for Higher Dimensional Systems . 129

6.3 Toward Real-Time Frequency Maps . . . 129

6.4 Comparing the Frequency and Escape Mappings . . . 132

Chapter 7. Conclusion and Summary of Results **140**

Bibliography **145**

List of Tables

1.1 Initial conditions for Figure 1.8 30

3.1 Initial conditions for Figure 3.8 55
3.2 Initial conditions for Figure 3.9 58

4.1 Frequencies of the Integrable Standard Map, $k = 0$ (I) 66
4.2 Frequencies of the Integrable Standard Map, $k = 0$ (II) 68

List of Figures

1.1 The Poincaré surface of section 3
1.2 Flows on tori in phase space. 8
1.3 The standard map in polar coordinates ($k = 0.3$). 17
1.4 Phase portraits of the standard map 20
1.5 Lift of the standard map 22
1.6 Winding numbers and the devil's staircase 25
1.7 Phase portraits of the coupled standard map 29

2.1 Poincaré sections for Cherry's Hamiltonian 37

3.1 Phase portrait of the uncoupled cubic map 45
3.2 Rotation numbers (frequencies) of the uncoupled cubic map . 46
3.3 Phase portraits of the cubic map for increasing t 47
3.4 Phase portrait of the uncoupled quadratic map 49
3.5 Rotation numbers (frequencies) of the uncoupled quadratic map 50
3.6 Phase portraits of the quadratic map for increasing τ 51
3.7 The effect of coupling on the phase portrait 52
3.8 Phase portraits of the coupled cubic-quadratic map (I) 56
3.9 Phase portraits of the coupled cubic-quadratic map (II) 57

4.1 Frequencies and the devil's staircase 65
4.2 Frequency maps of the Froeschlé mapping 69
4.3 Phase portraits of the uncoupled cubic-quadratic mapping . . 70
4.4 Frequencies of the uncoupled cubic-quadratic mapping 71
4.5 Phase portraits of the coupled cubic-quadratic mapping 71
4.6 Frequencies of the coupled cubic-quadratic mapping 72
4.7 The frequency map for various a values 73
4.8 Escape orbit for Form_1 of the coupled map (I) 75

4.9 Escape orbit for Form_1 of the coupled map (II) 76
4.10 Frequencies of the coupled mapping, Example I 77
4.11 Frequency analysis of the uncoupled quadratic map, $n = 2^9, 2^{10}$ 78
4.12 Frequency analysis of the uncoupled cubic map, $n = 2^9, 2^{10}$ . . 79
4.13 Diffusion along resonances (I) 81
4.14 Diffusion along resonances (II) 82
4.15 Diffusion along resonances: orbits 83
4.16 Frequency scan near the irregular orbit 84
4.17 Resonance frequencies with tori 85
4.18 Frequency scan for the coupled mapping (I) 86
4.19 Frequency scan for the coupled mapping (II) 87
4.20 Frequency analysis of a possible torus (I) 88
4.21 Frequency analysis of a possible torus (II) 89
4.22 A regular orbit for Form_1 of the coupled map 90
4.23 Shadowing plots for the uncoupled cubic and quadratic mappings 93
4.24 Shadowing plot for the coupled cubic and quadratic mapping . 94
4.25 Shadowing of orbits 95
4.26 Shadowing plot for a regular orbit 96
4.27 Frequency shadowing for the coupled cubic-quadratic mappings (I) 97
4.28 Frequency shadowing for the coupled cubic-quadratic mappings (II) 98
4.29 Frequency shadowing for the coupled cubic-quadratic mappings (III) 99
4.30 Frequency shadowing for the coupled cubic-quadratic mappings (IV) 100
4.31 Frequency shadowing at different sample lengths (I) 102
4.32 Frequency shadowing at different sample lengths (II) 103
4.33 Normalized computation times for various precisions 104

5.1 The coupled cubic-quadratic map in GGOBI 109
5.2 Projection of the coupled cubic-quadratic map in GGOBI . . . 111
5.3 The coupled and transformed cubic orbit. 113

5.4 Symplectic transformation of the coupled cubic-quadratic mapping 114
5.5 Comparison of the uncoupled and transformed quadratic orbit 114
5.6 Unwinding the torus via a canonical transformation 116
5.7 Comparison of unwound coupled orbit and uncoupled orbit . . 117
5.8 A higher dimensional Poincaré section 120
5.9 Rotation number via Poincaré section 121

6.1 Exit times for the coupled cubic-quadratic mapping 125
6.2 Histograms of escape times 126
6.3 Escape times for the Hénon map. 127
6.4 Benchmarking the escape times of the Hénon mapping 128
6.5 Escape map sections for the cubic-quadratic (I) 130
6.6 Escape map sections for the cubic-quadratic (II) 131
6.7 Single vs. double precision Form_2 (I) 134
6.8 Single vs. double precision Form_2 (II) 135
6.9 Exploring the structure of phase space (I) 136
6.10 Exploring the structure of phase space (II) 137
6.11 Escape times of the frequency map (I) 138
6.12 Escape times of the frequency map (II) 139

Chapter 1

Preliminaries

1.1 Hamiltonian Mechanics

The Hamiltonian formalism[1] is an elegant formulation of the laws of mechanics that is entirely equivalent to to the laws of motion provided by Newton's equations for nondissipative systems. A dynamical system is often described by a set of differential equations

$$\dot{z}^i = V^i(z), \qquad i = 1, \ldots, N \tag{1.1}$$

where z^i are the coordinates of the configuration manifold $\mathcal{Z}$ and $V(z)$ is an appropriate vector field. It is customary to refer to the solution of (1.1) as the flow. If the system has a time-dependent vector field $V = V(z,t)$, it is referred to as non-autonomous. The time dependence of such systems can always be removed by increasing the dimension; therefore in this work, we deal only with autonomous, or time-independent systems.

The dynamics of a Hamiltonian system take place in the arena of phase space, a $2N$ dimensional symplectic manifold in which volume and all other Poincaré invariants [121] are inherently preserved under the Hamiltonian

---

[1] See, for example, [2, 7, 62, 82, 11, 103, 48, 112, 116, 126, 138]

flow. The phase space is described by a set of configuration coordinates q^α and their canonically conjugate momenta p^α. That is, for $z = z(q, p)$,

$$\dot{z}^\alpha = V^\alpha(z), \qquad \alpha = 1, \ldots, M \tag{1.2}$$

where $M = 2N$. In canonical coordinates, we have

$$\dot{z}^\alpha = V_H^\alpha = J_c^{\alpha\beta} \frac{\partial H}{\partial z^\beta}, \qquad \alpha, \beta = 1, \ldots, M \tag{1.3}$$

where

$$J_c = \begin{pmatrix} 0_N & I_N \\ -I_N & 0_N \end{pmatrix}. \tag{1.4}$$

In this case, V_H is a Hamiltonian vector field generated by the Hamiltonian function $H : \mathcal{Z} \to \mathbb{R}$, O_N is the $N \times N$ null matrix, and I_N is the $N \times N$ identity matrix.

It is customary to write Hamilton's equations as

$$\dot{q}^i = \frac{\partial H}{\partial p_i}, \qquad \dot{p}^i = -\frac{\partial H}{\partial p_i}, \tag{1.5}$$

for $H = H(q^i, p^i)$ and $i = 1, 2, \ldots, N$. The state of a dynamical system is completely determined by the configuration $(q^1, q^2, ..., q^n)$, the conjugate momentum vector $(p^1, p^2, ..., p^n)$, and the Hamiltonian H.

1.2 The Poincaré Surface of Section

The study of modern dynamics began with Jules Henri Poincaré in the late 1800s [120]. In addition to his remarkable abilities in virtually all areas of mathematics and physics, Poincaré is regarded as the father of chaos theory. This is due to his development of topological and qualitative approaches to dynamics, his discovery of the hyperbolic tangle and the sensitive dependence of trajectories on initial conditions, the Poincaré recurrence theorem, and the surface of section technique which also bears his name.

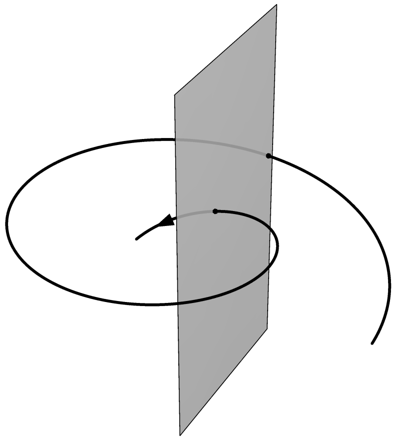

Figure 1.1: The Poincaré surface of section. A Poincaré section is obtained by the intersection of a surface with the flow in phase space.

The surface of section, also known as a Poincaré section, Poincaré surface, or Poincaré map, is essentially a means to reduce the dimensionality of the dynamics by one in order to better understand the higher-dimensional flow. Consider an integrable Hamiltonian system with N degrees of freedom. The dimension of phase space is $2N$, and the trajectories lie on an energy surface of dimension $2N-1$, and the dynamics lie on a manifold $\mathcal{M}$ of dimension N (see below). It is possible to choose a surface of section Σ_P that is transverse to the flow and that is of dimension $2N - 2$. The return map of the flow, denoted by $T : \Sigma_P \to \Sigma_P$, is obtained by successive intersections of the flow with the surface (Figure 1.1) [69, 88, 82, 116]. The Poincaré recurrence theorem guarantees that orbits reurn to the surface of section, and the map is invertible since the flow obeys time reversal. Importantly, the symplecticity of the Hamiltonian guarantees the symplecticity of the return map.

1.3 The KAM Theory

1.3.1 Integrable Systems

Integrability is a deep subject that forms the basis of much of the theoretical foundations of modern dynamics. In practice, roughly speaking an integrable system is one that can be integrated and for which analytical solutions exist in the form of quadrature. The dynamics of an integrable system in phase space lies on an N-dimensional torus. We begin with several definitions and examples.

Definition 1.3.1. An N degree of freedom Hamiltonian system is *Liouville integrable* if there exist N independent constants of motion, $I_i(z)$, $i = 1, 2, \ldots, N$ that are smooth, single-valued and in involution.

Definition 1.3.2. A function $I : \mathcal{Z} \to \mathbb{R}$ is said to be a constant of motion if

$$\dot{I} = \frac{\partial I}{\partial z^i} \dot{z}^i = \frac{\partial I}{\partial z^i} V^i(z) \equiv 0 \tag{1.6}$$

Corollary 1.3.1. *I is a constant of motion iff*

$$[I, H] = \frac{\partial I}{\partial z^\alpha} V_H^\alpha(z) = 0, \tag{1.7}$$

where [I,H] is the Poisson Bracket defined as follows.

Definition 1.3.3. The Poisson Bracket of two functions f and g is

$$[f, g] \equiv \frac{\partial f}{\partial z^\alpha} J_c^{\alpha\beta} \frac{\partial g}{\partial z^\beta}, \tag{1.8}$$

where α, $\beta = 1, 2, \ldots, 2N$.

Example 1.3.1. J_c is given by (1.4). Writing out (1.6) and (1.7), we see that

$$\dot{I} = \frac{\partial I}{\partial z^i}\dot{z}^i = \frac{\partial I}{\partial q^i}\dot{q}^i + \frac{\partial I}{\partial p^i}\dot{p}^i = \frac{\partial I}{\partial q^i}\frac{\partial H}{\partial p^i} - \frac{\partial I}{\partial p^i}\frac{\partial H}{\partial q^i} \equiv \frac{\partial I}{\partial z^\alpha} J_c^{\alpha\beta} \frac{\partial H}{\partial z^\beta} \tag{1.9}$$

Definition 1.3.4. Two functions I_i and I_j are said to be in *involution* if $[I_i, I_j] = 0$.

The constants of motion have important consequences on the geometry of phase space. If N constants of motion exist, the trajectories of the system can only explore an N-dimensional manifold $\mathcal{M}$ of the $2N$-dimensional phase space. For $N > 1$, the dimension of $\mathcal{M}$ is less than that of the energy surface $\mathcal{E}$. Therefore the trajectories cannot fully explore $\mathcal{E}$, demonstrating that the ergodic hypothesis is generally false. If the constants are in involution, $\mathcal{M}$ is an N-dimensional torus [11, 116]. The tori of integrable systems are invariant; an orbit or trajectory starting on an invariant torus remains on it forever.

1.3.2 Action-Angle Variables and Canonical Transformations

A natural description of tori is provided by action-angle variables. That is, we look for a transformation of coordinates $\bar{z}^\alpha = \bar{z}^\alpha(z^\alpha)$ yielding a new Hamiltonian $\bar{H}$ depending only on the new conjugate momenta $\bar{p}^\alpha$. There are many such choices. The most convenient is

$$\bar{p}^i \equiv J_i \equiv \oint_{\gamma_i} p_j dq^j, \qquad i = 1, 2, \ldots, N \tag{1.10}$$

where γ_i is a closed loop in phase space and J_i is the action. Conjugate to the new momenta are the new coordinates on the torus, the angles θ^i. These are obtained from the generating function (which ensures our new choice of coordinates is canonical),

$$S(q, J) = \int_{q_o}^{q} p_j dq^j. \tag{1.11}$$

Since our generating function is of type II, we have

$$\theta^i = \frac{\partial S}{\partial J_i} \tag{1.12}$$

and we can write Hamilton's equations in the new coordinates as

$$\dot{\theta}^i = \frac{\partial H}{\partial J_i}, \qquad \dot{J}_i = -\frac{\partial H}{\partial \theta^i}. \tag{1.13}$$

Since the new Hamiltonian is independent of θ^i, we have

$$J_i = const, \qquad \theta^i = \omega^i(J_i)t + \theta_o, \tag{1.14}$$

where

$$\omega^i(J_i) \equiv \frac{\partial H}{\partial J_i}. \tag{1.15}$$

As stated, a trajectory that starts on a torus (defined by J_i) stays on that torus for all time.

There is a useful result regarding canonical transformations that we will use later in Chap. 5. Consider the Poisson Bracket

$$[f, g] \equiv \frac{\partial f}{\partial z^i} J^{ij} \frac{\partial g}{\partial z^j} \tag{1.16}$$

Then, clearly,

$$[\bar{z}^l, \bar{z}^m] = \frac{\partial \bar{z}^l}{\partial z^i} J^{ij} \frac{\partial \bar{z}^m}{\partial z^j} = J^{lm}. \tag{1.17}$$

But for a coordinate transformation $\bar{z}^\alpha = S^\alpha_\beta z^\beta$, where S is a symplectic matrix, we have

$$[\bar{z}^l, \bar{z}^m] = \frac{\partial S^l_\beta z^\beta}{\partial z^i} J^{ij} \frac{\partial S^m_\gamma z^\gamma}{\partial z^j} = S^l_i J^{ij} S^m_j. \tag{1.18}$$

Therefore, we must have

$$S^l_i J^{ij} S^m_j = J^{lm}_c. \tag{1.19}$$

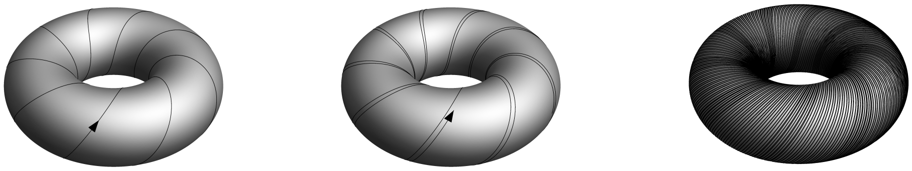

(a) Periodic (b) Quasiperiodic (c) Quasiperiodic

Figure 1.2: Flows on tori in phase space.

1.3.3 Frequencies on the Torus

From (1.14), we see that motion on the torus is governed by the frequency vector $\omega^i(J_i)$. That is, each angle on the N-dimensional torus has a corresponding frequency associated with it. If the frequencies are commensurate, then for $m_i \,\epsilon\, \mathbb{Z}$, they satisfy the relation

$$m_i \omega^i = 0, \tag{1.20}$$

and the orbit is periodic (Figure 1.2a), closing after some interval τ. If (1.16) does not hold, the frequencies are said to be incommensurate, and the trajectory is N-frequency quasiperiodic (Figure 1.2b). Since quasiperiodic trajectories do not close on themselves, these orbits eventually cover the entire surface of the torus (Figure 1.2c).

1.3.4 A Note on Integrability

What happens to an integrable system when it is perturbed? This is the central question at the heart of the KAM (Kolmorogov, Arnol'd, and Moser) theorem. On the one hand, if integrability is the general rule, then we could always reduce the motion to an N-torus phase space, given the appropriate coordinates, and assuming our ability to analytically find the constants of motion. On the other hand, if integrability is a rare exception, and most systems are in fact non-integrable, then one might expect a small perturbation of an integrable system to eliminate the constants of motion, destroy the tori, and allow the trajectory to wander throughout and eventually fill a manifold in phase space of dimension greater than $\mathcal{M}$. In this case, stability then becomes a question of how rare and how small, and a rigorous answer is provided by KAM. The KAM theorem guarantees that, although the set of integrable systems is of measure zero in the set of all Hamiltonian systems [110, 111], for sufficiently small perturbations satisfying a Diophantine condition, most of the invariant tori survive [68, 4, 108].

To achieve this result, Kolmorogov, Arnol'd, and Moser considered the effect of a perturbation on an integrable system. This is a question with deep physical implications and of significant practical importance. For example, the orbit of the Earth under the influence of the sun is integrable, a Keplerian orbit. What happens to this orbit under the influence of external perturbations, such as the the gravitational force from other planets and celestial objects? Is the orbit stable? For years, astronomers were plagued with this question. As we will see, seeking the solution to such a perturbed Hamiltonian system with classical perturbation theory fails because of the problem of small divisors, but KAM were able to guarantee convergence of solutions and the existence of tori for sufficient conditions. We do not provide details of the proof here, but refer readers to those works that provide further analysis. Details can be found in [11, 116, 126], and an elementary outline of the proof in [61].

The example of Earth's orbit and the survival of tori under weak perturbations represents one extreme of the problem at hand. On the other end of the spectrum is ergodicity, the fundamental ansatz of statistical mechanics that a system is equally likely to be found in a particular state as it is in any other. This is true if the system explores the entire energy surface available. One can imagine that a perturbation might sufficiently destroy the tori in phase space such that a trajectory could wander in such a way. If so, there would be no long term stability, but for a small perturbation a trajectory might be able to remain near a torus for a very long time. Although false in general, the ergodic theorem holds for two or more interacting hard spheres, so the foundations of statistical mechanics seem to be safe.

1.3.5 The Failure of Classical Canonical Perturbation Theory

Here we illustrate the problem of small divisors and the failure of classical perturbation theory [11, 116]]. Consider the perturbed Hamiltonian

$$H(J_i, \theta^i) = H_o(J_i) + \epsilon H_1(J_i, \theta^i). \tag{1.21}$$

For tori to exist in this new system there must be a new set of coordinates $(\bar{J}_i, \bar{\theta}^i)$ satisfying

$$H(J_i, \theta) = \bar{H}(\bar{J}_i), \tag{1.22}$$

and the new coordinates are generated from the old by the canonical generating function $S(\bar{J}_i, \bar{\theta}^i))$ such that

$$J_i = \frac{\partial S}{\partial \theta^i}, \qquad \bar{\theta}^i = \frac{\partial S}{\partial \bar{J}^i}. \tag{1.23}$$

From the previous two equations, we obtain the Hamilton-Jacobi equation for S:

$$H(\frac{\partial S}{\partial \theta^i}, \theta^i) = \bar{H}(\bar{J}_i). \tag{1.24}$$

To establish the existence of tori, we seek solutions to (1.20) in the form of a power series,

$$S = S_o + \epsilon S_1 + \epsilon^2 S_2 + \dots \tag{1.25}$$

where $S_o = \theta^i \bar{J}_i$ so that $\theta^i = \bar{\theta}^i$, $J_i = \bar{J}_i$ when $\epsilon = 0$. We substitute this into (1.20), using H as given by (1.18). Then we have

$$H_o(\bar{J}_i + \epsilon \frac{\partial S_1}{\partial \theta^i} + \dots) + \epsilon H_1(\bar{J}_i + \dots, \theta^i) = \bar{H}(\bar{J}_i). \tag{1.26}$$

We can expand this in powers of ϵ. Retaining only the first-order terms, we are left with

$$H_o(\bar{J}_i) + \epsilon \frac{\partial H_o}{\partial \bar{J}_i} \epsilon \frac{\partial S_1}{\partial \theta^i} + \dots) + \epsilon H_1(\bar{J}_i, \theta^i) = \bar{H}(\bar{J}_i). \tag{1.27}$$

We note that H_1 and S_1 are periodic in $\bar{\theta}^i$ and we can write

$$S_1(\bar{J}_i, \bar{\theta}^i) = \sum_m S_{1,m}(\bar{J}_i) e^{\mathrm{i} m_i \theta^i} \tag{1.28}$$

$$H_1(\bar{J}_i, \bar{\theta}^i) = \sum_m H_{1,m}(\bar{J}_i) e^{\mathrm{i} m_i \theta^i} \tag{1.29}$$

If we substitute these expressions into (1.23) we obtain the generator of the new tori,

$$S(\bar{J}_i, \bar{\theta^i})) = S_o + \epsilon \, \mathrm{i} \sum_m \frac{H_{1,m}(\bar{J}_i)}{m_i \omega_o^i(\bar{J}_i)} e^{\mathrm{i} m_i \theta^i}, \tag{1.30}$$

where $\omega_o^i(\bar{J}_i)$ is the N-dimensional frequency vector defined in (1.15). Unfortunately, this results in the pathological divergence of (1.26); for unperturbed tori with commensurate frequencies there are always terms that satisfy $m_i \omega_o^i = 0$. For these tori, the series diverges and our attempted solution fails. However, there are tori for which the series converges; these are the so-called KAM tori (below).

1.3.6 The Destruction of Tori

The central result of the KAM theorem is that for sufficiently small perturbations, most tori survive. How do these tori survive and what happens when tori do not survive? The answer lies in the so-called "Arithmetic of Torus Destruction" [11]. Here we refer the reader to references [116, 82, 124] for a general discussion, and merely restate the central result (recall Sec. 1.3.4): for sufficiently small perturbations, sufficiently irrational tori survive and are not destroyed. The meaning of "sufficiently irrational" is illustrated by considering the continued fraction expansion of an irrational number x:

$$x = [a_0, a_1, a_2, \cdots] = a_0 + \cfrac{1}{a_1 + \cfrac{1}{a_2 + \cdots}}. \tag{1.31}$$

If we terminate the sequence at a finite number n, we have

$$x = [a_0, a_1, \cdots, a_n] = a_0 + \cfrac{1}{a_1 + \cfrac{1}{\ddots + \cfrac{1}{a_n}}}. \tag{1.32}$$

Recall that tori in phase space are identified by their frequency ratio ω_1/ω_2. Then we can approximate any irrational tori to any arbitrary degree of closeness with its finite continued fraction expansion. Clearly, this approximation converges faster if the sequence $[a_0, a_1, \cdots, a_n]$ diverges faster. In that sense, the "most irrational" number, the number that converges the slowest, and which was conjectured to be the last remaining torus by Greene [42], is the Golden Mean:

$$[1, 1, \cdots 1] = 1 + \cfrac{1}{1 + \cfrac{1}{\ddots + \cfrac{1}{1}}} = \frac{\sqrt{5}-1}{2} \approx .618033989... \tag{1.33}$$

1.4 The Arnol'd Diffusion

The Arnol'd Diffusion is a phenomena of higher degree of freedom ($N > 2$) systems. For systems with low degrees of freedom, invariant tori of dimension N divide the $2N - 1$ energy surface (the region of phase space that is energetically available), and irregular orbits are constrained by tori. An analogy is that while a line divides a plane, a line does not divide a three dimensional space. In much the same way, chaotic orbits that were proven by

KAM to exist arbitrarily close to tori, are now free to wander around tori in higher dimensions.

The classical meaning of the Arnol'd Diffusion is that ascribed by Arnol'd in his seminal paper [5]; a perturbed Hamiltonian system forms a dense network of interconnecting resonances (the Arnol'd Web) that permeates the entirety of phase space, and the chaotic regions surrounding the resonances intersect. Therefore, an initial condition lying in the chaotic region may diffuse arbitrarily far from its starting point; this is the Arnol'd Diffusion [134, 135, 18, 126, 116, 82], a fundamental property of Hamiltonian systems subjected to perturbation.

Technically, Arnol'd Diffusion refers only to motion along the resonance network or web, specifically the diffusion along the dominant (guiding) resonance onto intersecting resonance (see [126] for a discussion of the guiding resonance of Arnol'd's Hamiltonian presented in [5]). However, it is not uncommon to refer to any motion of a trajectory around existing tori in higher dimensional phase spaces as such, and different types of diffusion [134, 135, 82] can occur.

1.5 Symplectic Mappings

1.5.1 Symplectic Maps and the Poincaré Surface of Section

As we have seen, the return map $T : \Sigma_P \to \Sigma_P$ of the flow (the Poincaré surface of section) is a valuable technique for analyzing the dynamics of a flow. For integrable systems, we can derive an exact map (known as a *twist* mapping; see [11, 116]) that relates the return of the flow to the previous intersection:

$$r' = r_o, \qquad \Theta' = \Theta_o + 2\pi\alpha r_o, \tag{1.34}$$

where α is known as the rotation number of the map.

However, since integrable systems are the rare exceptions, it is natural to ask if there are other maps which correspond to nearly integrable Hamiltonian flows. It turns out there are, by a theorem due to Moser [113]. Return maps inherit symplecticity from the Hamiltonian flow, and we may easily construct symplectic mappings by means of a generating function. In Chap. 3 we shall do just this.

1.5.2 The Standard Map

The standard map, also known as the Chirikov-Taylor map, is one of the most important models in modern dynamics. It is an essential tool for understanding KAM, the breakup of tori, and the transition to chaos. Boris Chirikov derived the map as a universal description for resonances in Hamiltonian systems [18], and Bryan Taylor derived it as a model of charged particles in a magnetic field [98, 99, 42]. The standard map is also useful as a model of magnetic field lines [104], but it is the universal description of the behavior of Hamiltonian systems that chiefly interests us here.

Perhaps the most natural expression of the standard map is

$$\begin{aligned} \theta' &= \theta + J' \\ J' &= J + \frac{k}{2\pi}\sin(2\pi\theta), \end{aligned} \tag{1.35}$$

where $k > 0$. In this setting, the initial value of J determines the torus, θ is the angle of the cross section, and the map corresponds to a Poincaré section of the flow on the torus $\mathbb{T}^2$. There are two angles θ_1 and θ_2 with two respective frequencies ν_1 and ν_2 on this torus. If the ratio of the frequencies ν_1/ν_2 is rational, then the trajectory goes around the θ_1 cross section of the torus a times for every b revolutions around the θ_2 cross section. The result of this is a set of points in the Poincaré section. If the frequency ratio is irrational, the trajectory is quasiperiodic, resulting in a continuous curve in the phase space of the map. To visualize the map, one iterates a variety of initial conditions for some number and plots the results in phase space (Figures 1.1 and 1.2).

Example 1.5.1. If $a = 1$ and $b = 3$, then the frequency ration is $\frac{1}{3}$. The Poincaré section of this trajectory is simply three evenly spaced points that lie on a circle. This is referred to as the $\frac{1}{3}$ *resonance.*

1.5.2.1 Rotation Numbers, Winding Numbers, and the Breakup of Tori

In Sec. 1.3, the ratio of the frequencies on the torus was defined to be the rotation number of a twist map. However, one can calculate this ratio *a posteriori* from the Poincaré section without knowledge of the flow.

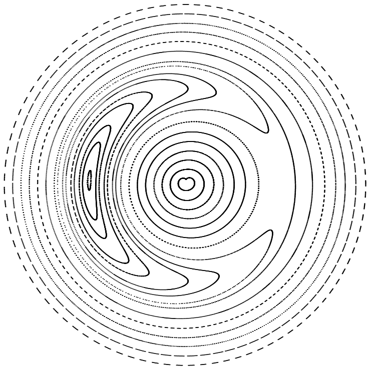

Figure 1.3: The standard map in polar coordinates ($k = 0.3$).

Definition 1.5.1. The rotation number ρ of an orbit defined by the area-preserving map $T : \mathbb{R} \to \mathbb{R}$ is

$$\rho = \lim_{n\to\infty} \frac{1}{2\pi} \sum_{i=1}^{n} \frac{\theta_i - \theta_{i-1}}{i} \approx \frac{\Delta\theta}{2\pi n}, \tag{1.36}$$

where $\Delta\theta$ is the total angle between the first and nth iterations, as measured relative to the island of interest.

Example 1.5.2. The angle between subsequent iterations of the $\frac{1}{3}$ resonance is 120 degrees. Clearly then, from (1.36), the rotation number of the $\frac{1}{3}$ *resonance* is $\frac{1}{3}$.

Note that it is possible to obtain rotation numbers for any region of the map containing closed curves (see Figure 1.2). These regions, surrounding the elliptical fixed points that appear when the resonant tori break up, are known as islands, and a set of rotation numbers for each island may be calculated using (1.36), where θ is measured relative to the center of the island of interest. This is not the usual procedure, but it may help to clear up confusion that can arise when using the terms frequencies, winding numbers, and rotation numbers interchangeably. As we have seen in Sec. 1.3 and by direct example above, the rotation number of a twist map is equal to the ratio of the frequencies on the torus. In fact, the terms winding number and rotation number are often used interchangeably, but here we reserve the term winding number for that frequency associated with the lift (see below) of an area-preserving map.

It is also common (and instructive) to write the standard map as

$$\begin{aligned} x' &= x + p' \bmod 1 \\ p' &= p + \frac{k}{2\pi}\sin(2\pi x), \end{aligned} \tag{1.37}$$

where $k > 0$. One may also take $k < 0$, which is equivalent to shifting the value of θ by π. In this work, we take $k > 0$ and shift the center island to the middle of the domain of interest. Figure 1.2 shows the phase portrait of the standard map in these coordinates for increasing values of k. For $k = 0$, the map is integrable and the frequencies are simply the initial values of p. If p_o is rational, a periodic orbit results; if irrational, we obtain a quasiperiodic orbit (Figure 1.2a). As k increases, the resonant tori break up and are replaced by alternating elliptical and hyperbolic fixed points orbits, leading to stochasticity in the phase space (Sec. 1.3). This can be seen in Figure 1.2b, where new islands surrounding the elliptical fixed points have appeared in the phase space. Increasing k further results in the breakup of more tori and a more complicated picture in phase space. Below the critical value of $k_c = 0.9716...$, the last remaining torus is intact (Figure 1.2d).

What happens to the frequencies as the tori break? First, let us compare the standard map in polar coordinates and as given by (1.37). Directly, compare Figure 1.3 and Figure 1.4b. In polar coordinates, the tori are circles, as one would expect from a Poincaré section of the flow on a torus. In Figure 1.4b, the tori are the roughly horizontal lines, and the center island corresponds to the "banana" region of the polar phase portrait. How then, do we compare frequencies between these two representations? What are the frequencies on the torus? From Figure 1.3, there are two rotation numbers, or frequencies, to calculate using (1.36). One, the rotation number around the center of the phase portrait, and two, the rotation number of the "banana" island region. Clearly, one could measure the rotation number of this island that lies at the center of Figure 1.4b, but how can one measure the other frequencies? The answer to this question lies in the *winding number* of the map.

Definition 1.5.2. The winding number of an orbit of the area-preserving map $T : \mathbb{R} \to \mathbb{R}$ is

$$w = \lim_{n\to\infty} \frac{q_n}{n}, \tag{1.38}$$

where

$$\begin{pmatrix} q_{n+1} \\ p_{n+1} \end{pmatrix} = T \begin{pmatrix} q_n \\ p_n \end{pmatrix}, \tag{1.39}$$

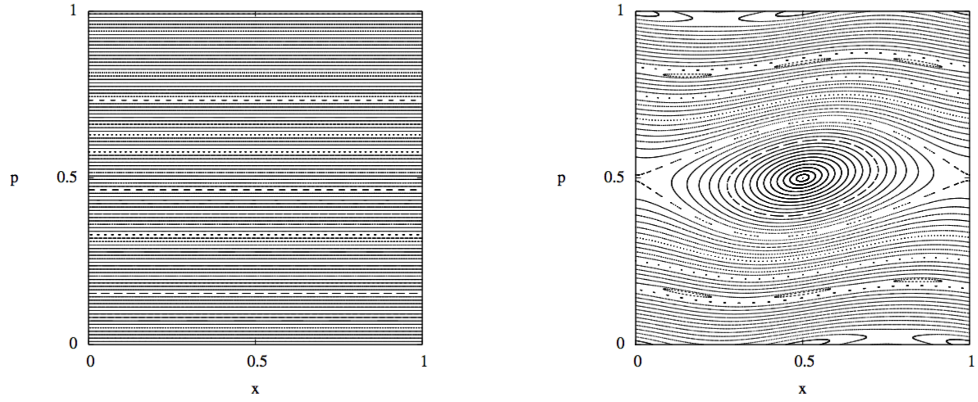

(a) k = 0 (b) k = 0.3

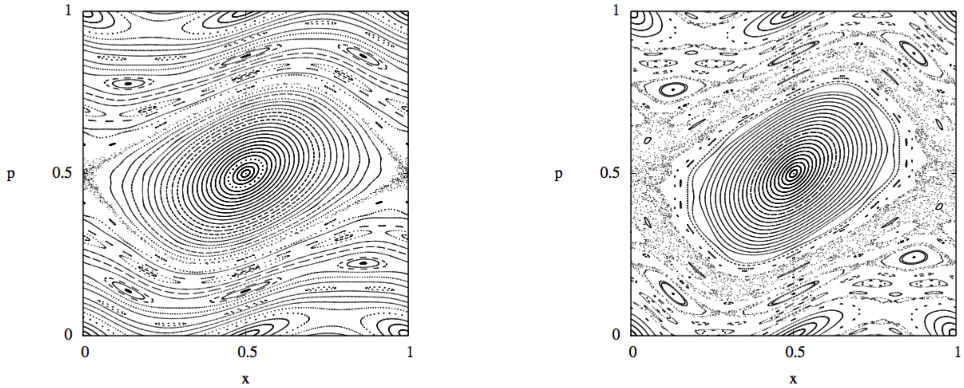

(c) k = 0.7 (d) k = 0.97

Figure 1.4: Phase portraits of the standard map. Portraits are shown for increasing values of the parameter k. (a) When $k = 0$, the system is integrable and the tori are straight lines in the phase space. $(b) - (d)$ As k increases, resonance overlap and the breakup of the tori occurs, leading to stochastic regions. At $k = 0.97$, the last remaining tori is still intact, but barely.

Note that the winding number is obtained from the lift $\mathbb{T} \times \mathbb{R}$, where q_n is lifted to $\mathbb{R}$ instead of $\mathbb{T}$. Figure 1.5 demonstrates the lift of the standard map.

In the "natural" coordinates (J, θ) of the standard map (1.35), the winding number corresponds to the ratio of the two frequencies on the 2-dimensional torus (recall Sec. 1.3.2). In part, this is due to the fact that it is common for mathematicians to refer to the "winding number" of a knot or a curve on a torus. In this setting, the winding number is simply the number of times the curve winds around in one direction versus the other. Since the Poincaré section sets one of the frequencies to 2π or 1, it is common to refer to the winding number as "the frequency" of the standard map. See [11, 88, 82, 126] for further discussion.

Example 1.5.3. The lift of the standard map as written in (1.37) is simply

$$\begin{aligned} x' &= x + p' \\ p' &= p + \frac{k}{2\pi}\sin(2\pi x). \end{aligned} \tag{1.40}$$

Now the map is identical to (1.35), given the transformation $(p, x) \to (J, \theta)$. Therefore, the winding number is merely

$$w = \lim_{n\to\infty} \frac{\theta_n}{n}, \tag{1.41}$$

which is equivalent to (1.36) for the rotation number. There is no factor of 2π because we have written the standard map for the domain [0,1]. Conversely, one could iterate the map of (1.35), calculate the change in angle over each iteration, and take the average as defined by (1.36) and in this manner obtain the rotation number.

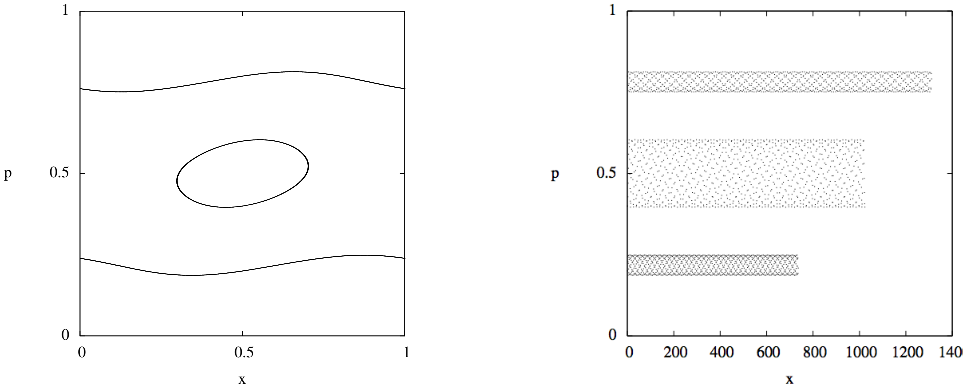

(a) k = 0.3 (b) lift, k = 0.3

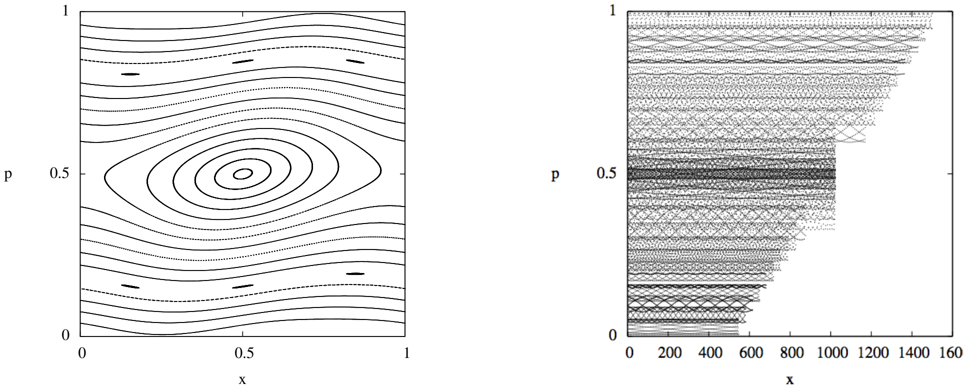

(c) k = 0.3 (d) lift, k= 0.3

Figure 1.5: Lift of the standard map. The standard map is shown in $\mathbb{T}^2$ (left) and the lift $\mathbb{T} \times \mathbb{R}$ (right). The winding number is defined only for the lift. Note the similarity to the "Devil's Staircase" in (d).

Example 1.5.4. For the $\frac{1}{3}$ resonance, the lift of the standard map with $k = 0$ gives $\theta_n = \frac{1}{3}, \frac{2}{3}, \frac{3}{3}, \frac{4}{3}, \ldots = \frac{1}{3}n$. A good approximation of the winding number is obtained by letting $n \to \infty$. If we take $n = 10^5$, the winding number is $w = \frac{1/3 \cdot n}{n} = \frac{1}{3}$. This is the same result that we obtained in example 1.5.2 demonstrating the calculation of the rotation number.

Thus far we have been concerned with the frequencies of the map relative to the center of the map in polar coordinates. These are the winding numbers shown in Figure 1.5. Here, the winding numbers have been calculated for 1000 trajectories evenly spaced in p_o. For $k = 0$, the map is integrable and the frequencies are simply the initial values of p. Thus, a plot of the winding numbers is a straight line. A nonzero values of k adds a nonintegrable perturbation to the map, and as demonstrated in the phase portraits of Figure 1.4, the tori breakup and islands appear. This corresponds to the appearance of the (vertically) flat region in Figure 1.5d. Recall that the center island of the standard map in the $p - x$ plane is the "banana" region of the map as plotted in polar coordinates. Attempting to measure the rotation of these trajectories around the center of the plot yields an average of zero, but here we have shifted the island by $\frac{1}{2}$ so that it appears in the center. Therefore, the frequency obtained is $\frac{1}{2}$. In the literature it is common to see this plot shifted up or down, with the island region at the bottom of the plot. As k increases (cf. Figures 1.4 and 1.6), further islands appear in the phase portrait and we see corresponding flat regions in the frequency plot. This is the so-called "Devil's Staircase". At any scale of the map, islands exist, and so zooming in on the frequency plot yields further and further appearances of “steps” in the staircase. However, as k increases, even as steps on the staircase appear, entire regions of stairs disappear and “blow up”. Further, the flat regions of the staircase shift as a result of the perturbation. Hence, the description is apt.

1.5.3 Higher Dimensional Symplectic Mappings

Examples of higher dimensional symplectic mappings exist in the literature [29, 33, 30, 63, 139]. Here we introduce some phenomena of a higher dimensional mapping through a four dimensional systen which has been extensively studied [29, 33, 76, 63]. This map is a composition of two coupled standard mappings and is used to model the evolution of galaxies in the solar system as well as for the study of higher dimensional systems. In Chap. 4 we use this mapping to demonstrate agreement of our frequency method with results in the literature. Here we use the map to illustrate the complexity of trajectories in the phase space that can result from four dimensions instead of two.

1.5.3.1 The Froeschlé Map and the Generalized Coupled Standard Mapping

The Froeschlé map is a generalized coupled standard mapping that was suggested by Arnol’d to M. Hénon[2]. It is directly related to the inverse of the

---

[2] The original reference is [33]. For an interesting account and a partial reproduction of Arnold’s original letter to Hénon, see [79].

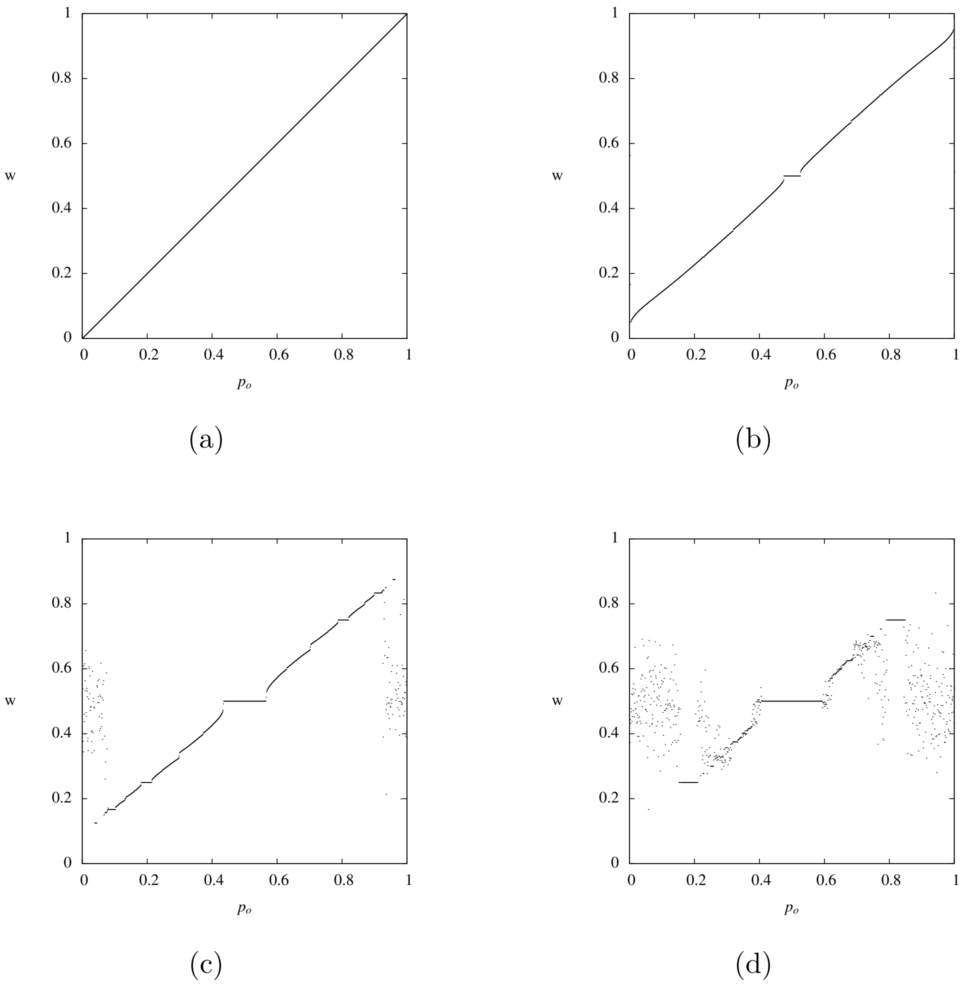

(a) (b)

(c) (d)

Figure 1.6: Winding numbers and the devil's staircase in the standard map. As k increases, islands appear on every scale. This is reflected in the frequency (winding number) plot as the appearance of "steps" in the Devil's Staircase. No matter how far one zooms in, further "steps on steps" with be revealed. As k increases from 0 (a), the frequency plot breaks up, corresponding to stochastic regions in the map.

Chirikov-Taylor map, as we will now demonstrate. The standard Chirikov-Taylor mapping can be written as

$$\begin{aligned} x' &= x + y' \bmod 2\pi \\ y' &= y + k\sin(x). \end{aligned} \tag{1.42}$$

The inverse of this is

$$\begin{aligned} x' &= x - y \bmod 2\pi \\ y' &= y - k\sin(x'). \end{aligned} \tag{1.43}$$

Making the substitution $(x, y) \rightarrow (-\tilde{y}, \tilde{x})$, and setting $k = a$ yields

$$\begin{aligned} y' &= y + x \bmod 2\pi \\ x' &= x + a\sin(y'), \end{aligned} \tag{1.44}$$

where the tildes have been dropped for convenience. Coupling two of these maps with the coupling parameter b gives the Froeschlé map,

$$\begin{aligned} x_1' &= x_1 + a_1\sin(y_1') + b\ sin(y_1' + y_2') \\ y_1' &= y_1 + x_1 \bmod 2\pi \\ x_2' &= x_2 + a_2\sin(y_2') + b\ sin(y_1' + y_2') \\ y_2' &= y_2 + x_2 \bmod 2\pi, \end{aligned} \tag{1.45}$$

or equivalently,

$$\begin{aligned}
x_1' &= x_1 + a_1 \sin(y_1 + x_1) + b\ sin(y_1 + x_1 + y_2 + x_2) \\
y_1' &= y_1 + x_1 \bmod 2\pi \\
x_2' &= x_2 + a_2 \sin(y_2 + x_2) + b\ sin(y_1 + x_1 + y_2 + x_2) \\
y_2' &= y_2 + x_2 \bmod 2\pi. \qquad (1.46)
\end{aligned}$$

Alternatively, one may examine the generalized coupled standard mapping [63]:

$$\begin{aligned}
\theta_1' &= \theta_1 + I_1' \bmod 1 \\
I_1' &= I_1 + \frac{k_1}{2\pi}\sin(\theta_1) + \frac{b}{2\pi}\ sin(\theta_1 + \theta_2) \\
\theta_2' &= \theta_2 + I_2' \bmod 1 \\
I_2' &= I_2 + \frac{k_2}{2\pi}\sin(\theta_2) + \frac{b}{2\pi}\ sin(\theta_1 + \theta_2).
\end{aligned} \qquad (1.47)$$

Examples of the trajectories obtained from this mapping are shown in Figure 1.8. Note the complexity and different types of orbits. For small b, the phase portrait in each of the $I_i - \theta_i$ planes is close to what we see for a 2-dimensional standard map (Figure 1.4). Just as increasing k in the standard map leads to the destruction of tori in the phase space, increasing k_1 or k_2 has the same effect here. However, the coupling parameter also plays a large role. Immediately upon $b > 0$, the curves of the 2-dimensional standard map are perturbed into more complicated orbits. Instead of a 2-dimensional map, each of the of $I_i - \theta_i$ planes is now a projection of the 4-dimensional mapping. In addition, the coupling of the maps introduces an additional frequency in each, i.e., each map now has a contribution from θ_1 and θ_2 with frequencies ω_1 and ω_2. This leads to the complex figures of Figure 1.8, which are orbits of the 4-dimensional mapping plotted in the $I_1 - \theta_1$ plane.

The complexity of the orbits from a higher dimensional mapping poses problems for analyzing the dynamics with the tools developed for lower dimensional systems. Ordinarily, one could examine the frequencies of the map by analyzing the winding or rotation numbers discussed earlier. This would allow us to find the tori in phase space, essential for demonstrating Arnol'd Diffusion. However, as seen in Figure 1.7 (also, Figure 3.7), the addition of a second frequency makes this difficult with sufficient coupling. To define a rotation number, one must have a set of points with an appropriate choice of origin. Clearly this is not the case for most of the trajectories in Figure 1.7. But since the map is symplectic, regular trajectories must lie on tori, and with an appropriate coordinate choice we can recover a projection that yields simple closed curves in phase space. We can then take the rotation numbers as needed (Chap. 5). However, the method of frequency analysis allows us to obtain the frequencies on the torus, which are identical to the rotation numbers for our map, without this procedure (Chap. 4).

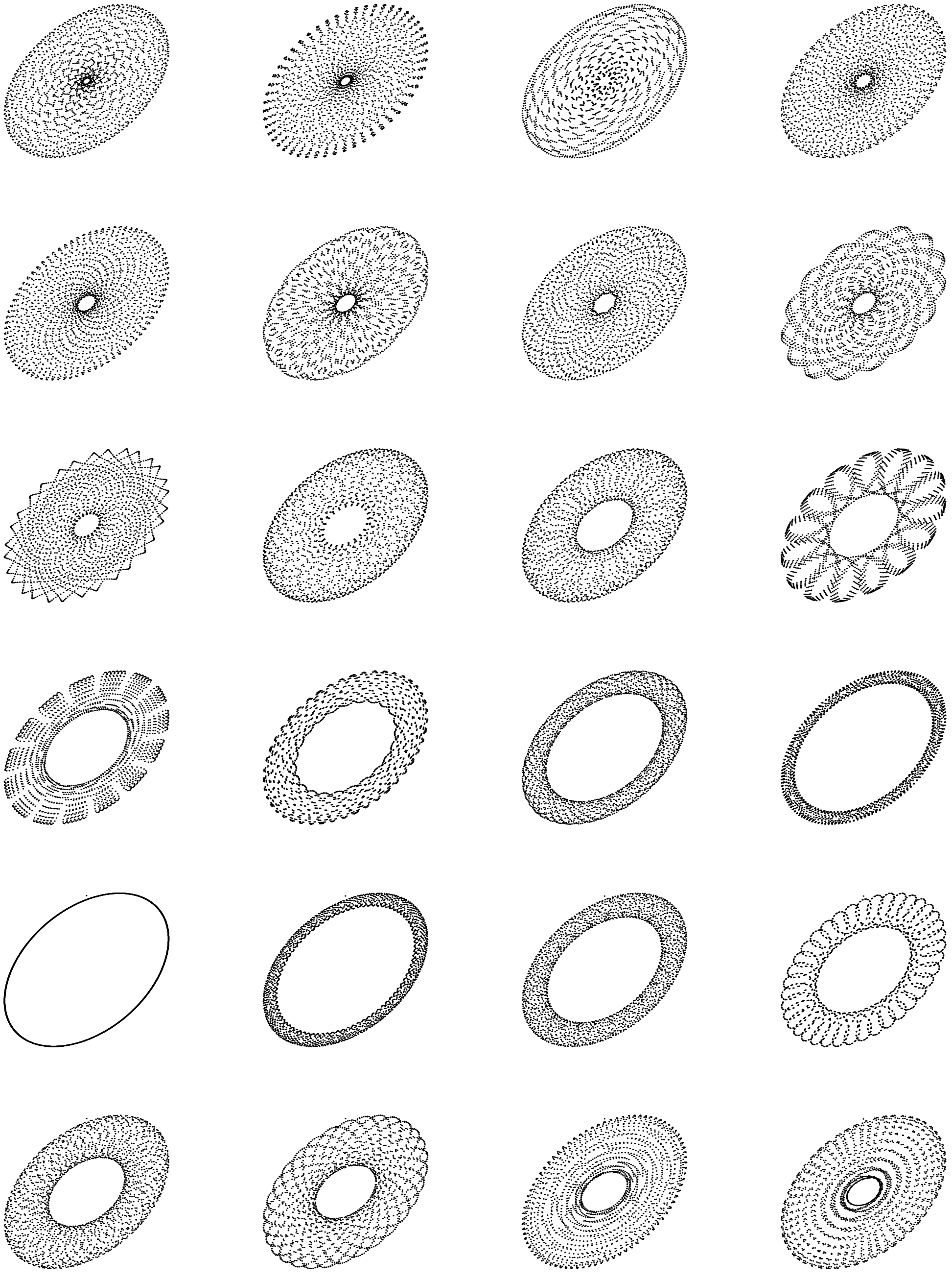

Figure 1.7: Phase portraits of the coupled standard map for $k_1 = k_2 = 0.7, b = 0.01$. The map was iterated 2^{11} times for each initial condition and the results plotted in the $I_1 - \theta_1$ plane (see the explanation of Table 1.1).

Table 1.1: Initial conditions for Figure 1.8. As we move down the table, the initial conditions increase in x_1 and x_2, corresponding to the orbits in Figure 1.8 from left to right, top to bottom.

x_1	y_1	x_2	y_2
0.5020000000000000	0.5000000000000000	0.5500000000000000	0.5000000000000000
0.5030000000000000	0.5000000000000000	0.5520000000000000	0.5000000000000000
0.5040000000000000	0.5000000000000000	0.5540000000000000	0.5000000000000000
0.5050000000000000	0.5000000000000000	0.5560000000000000	0.5000000000000000
0.5060000000000000	0.5000000000000000	0.5580000000000000	0.5000000000000000
0.5070000000000000	0.5000000000000000	0.5600000000000000	0.5000000000000000
0.5080000000000000	0.5000000000000000	0.5620000000000000	0.5000000000000000
0.5090000000000000	0.5000000000000000	0.5640000000000000	0.5000000000000000
0.5100000000000000	0.5000000000000000	0.5660000000000000	0.5000000000000000
0.5110000000000000	0.5000000000000000	0.5680000000000000	0.5000000000000000
0.5120000000000000	0.5000000000000000	0.5700000000000000	0.5000000000000000
0.5130000000000000	0.5000000000000000	0.5720000000000000	0.5000000000000000
0.5140000000000000	0.5000000000000000	0.5740000000000000	0.5000000000000000
0.5150000000000000	0.5000000000000000	0.5760000000000000	0.5000000000000000
0.5160000000000000	0.5000000000000000	0.5780000000000000	0.5000000000000000
0.5170000000000000	0.5000000000000000	0.5800000000000000	0.5000000000000000
0.5180000000000000	0.5000000000000000	0.5820000000000000	0.5000000000000000
0.5190000000000000	0.5000000000000000	0.5840000000000000	0.5000000000000000
0.5200000000000000	0.5000000000000000	0.5860000000000000	0.5000000000000000
0.5210000000000000	0.5000000000000000	0.5880000000000000	0.5000000000000000
0.5220000000000000	0.5000000000000000	0.5900000000000000	0.5000000000000000
0.5230000000000000	0.5000000000000000	0.5920000000000000	0.5000000000000000
0.5240000000000000	0.5000000000000000	0.5940000000000000	0.5000000000000000
0.5250000000000000	0.5000000000000000	0.5960000000000000	0.5000000000000000
0.5260000000000000	0.5000000000000000	0.5980000000000000	0.5000000000000000

1.5.3.2 A Note on Higher Dimensional Poincaré Sections

As we have seen, the dynamics of an N-dimensional integrable Hamiltonian system takes place on an N-dimensional torus in phase space. A $2N-2$-dimensional symplectic map is generated by taking a Poincaré section of this flow. For a 2-degree-of-freedom system, the map is 2-dimensional, but for three degrees of freedom, the map is 4-dimensional. Clearly, we cannot easily visualize a four-dimensional object, but if we are in action-angle variables it is simpler to visualize projections of a four-dimensional Poincaré section. We have $J_1, J_2, \theta_1, \theta_2$ and we can use closed curves in the $J_i - \theta_i$ planes to define a torus. In Chap. 5, we decompose a higher dimensional mapping into $N-1$ projections that yield simple, closed curves. In Chap. 3, we will introduce a simpler, computationally less expensive 4-dimensional map that will allow us to explore the phenomena of Arnol'd Diffusion: the coupled cubic-quadratic map. This mapping arises naturally from considerations of stability and the phenomena of Negative Energy Modes (Chap. 2), and provides a natural means to explore Arnol'd Diffusion in a lower dimensional Hamiltonian system.

Chapter 2

Stability of Equilibria and Negative Energy Modes

Stability is of paramount importance in classical physics, and has a rich history. Of relevant interest to this work is the existence of negative energy waves or modes of oscillation that turn unstable when dissipation is added to the system (Sec. 2.2). Numerous examples and discussions can be found in the literature. Treatments of stability be found in [103, 105], as well as the classical texts of [7] and [2]. For negative energy modes, see [102, 106, 71]. For a comprehensive analysis of linear stabily in two-dimensional and four-dimensional maps, see [88]. Here we offer definitions of the various types of stability that are of primary interest to Hamiltonian Dynamics, describe the Negative Energy Modes that can exist in Hamiltonian Systems, and offer examples of such behavior to motivate our introduction of the coupled cubic-quadratic mapping in Chap. 3.

Generally speaking, *stability* refers to the behavior of solutions of a flow $\dot{z}^i = V^i(z)$ around *fixed points*, or *equilibria*, z_e that satisfy $V(z_e) = 0$ for all time. Equilibria are said to be stable if solutions that begin within a sufficiently small distance of z_e remain close to z_e for all time. Systems may be *linearly stable*, under the linearized dynamics of the flow, or *nonlinearly stable* (see below). A system may also be *Lyupanov stable* or *spectrally stable*.

2.1 Types of Stability

Definition 2.1.1. An *equilibrium point* of the flow $\dot{z}^i = V^i(z), i = 1, \ldots, N$, satisfies the condition $V(z_e) \equiv 0$.

Definition 2.1.2. The equilibrium point z_e is said to be *stable* if, for any neighborhood N of z_e, there exists a sub-neighborhood $S \subset N$ of z_e such that if $z(t = 0) \in S$, then $z(t) \in N$ for all time $t > 0$.

Definition 2.1.3. z_e is said to be *asymptotically stable* if $\lim_{t \to \infty} z(t) = z_e$.

Definition 2.1.4. If $z(t)$ is stable according to the above definition under the linearized dynamics

$$\delta \dot{z}^i = \frac{\partial V^i}{\partial z^j}(z_e) \delta z^j, \tag{2.1}$$

then z_e is *linearly stable*. Equivalently, the linearized flow $z(t) \approx z_e + \delta z$, or Eq. (2.1) itself, is said to be linearly stable.

Linear stability is sometimes referred to as *local stability*. If an equilibria is stable under the full dynamics, it is said to be *nonlinearly* or *globally* stable. This type of stability is also referred to as *Lyapunov stability* [86]. If an equilibria is linearly stable, but unstable under the full nonlinear dynamics, it is said to be *nonlinearly unstable*. A *finite amplitude* *instability* refers to an equilibrium point that is perturbed far enough to be unable to remain stable. For example, many physical systems will not remain stable under an earthquake or other large amplitude perturbation.

One last type of stability is related to the linear flow (3.1). If a system is linearly stable, then under the substitution $\delta z = \delta \hat{z} e^{\lambda t}$, we obtain an eigenvalue problem for λ.

Definition 2.1.5. A linear system of the form $\dot{z}^i = A^i_j\, z^j$ is *spectrally stable* if all the eigenvalues of the matrix A^i_j are pure imaginary.

2.2 Negative Energy Modes: Definition and Examples

Negative energy modes [101, 137, 103, 71, 73, 90, 102, 106, 22, 43] are found in fluids and plasma systems, general mechanical systems with gyroscopic forces (such as the Coriolis force), in the dynamics of particles in magnetic fields, and the well known “three wave” problem. Here we outline the motivation behind the terminology.

If a Hamiltonian system is not separable, but can be written as a general function of q and p, Dirichlet’s theorem [23] gives a sufficient condition for stability. If families of constant H surfaces define a good neighborhood near an equilibrium point, then the equilibrium is nonlinearly stable. If the Hamiltonian is well behaved, a definite [1] matrix $\partial^2 H(z_e)/\partial z^i \partial z^j$, where $z = (q, p)$, indicates stability. Note that H can be a maximum of the energy,

---

[1] A matrix is definite if all eigenvalues have the same sign and are greater than zero.

as is typical for localized vortices in fluid mechanics and can also occur for rigid bodies [103].

However, if the matrix is indefinite it can be globally (spectrally) unstable, but linearly stable. In this case, the system possesses both positive and negative energy modes. We examine such a case next.

2.2.1 Cherry's Example: Wave-Wave Resonance

Cherry's Hamiltonian [17] is

$$H = \frac{1}{2}\omega_2(p_2^2 + q_2^2) - \frac{1}{2}\omega_1(p_1^2 + q_1^2) + \frac{1}{2}\alpha[2q_1p_1p_2 - q_2(q_1^2 - p_1^2)] \tag{2.2}$$

where the frequencies ω_1 and $\omega_1 > 0$, and α is a nonlinear parameter. Oscillator one (ω_1) is what is commonly referred to as a Negative Energy Mode, and due to the minus sign the matrix $\partial^2 H(z_e)/\partial z^i \partial z^j$ is not definite. Hence, the system is linearly stable but nonlinearly unstable.

With the transformation $q_i = \sqrt{2J_i}\sin\theta_i$, $p_i = \sqrt{2J_i}\cos\theta_i$, Cherry's Hamiltonian takes the following form:

$$H = \omega_1 J_1 - \omega_2 J_2 + \alpha J_1 \sqrt{J_2}\sin(2\theta_1 + \theta_2). \tag{2.3}$$

Kueny [70, 71] extensively analyzed Cherry's system in the context of wave-wave resonance and explosive growth. Solutions exist for the resonance condition $2\omega_1 = \omega_2$. They are:

$$\begin{aligned} q_1 &= \frac{\sqrt{2}}{\epsilon - \alpha t} \sin{(\omega_1 t + \gamma)} \\ p_1 &= \frac{\sqrt{2}}{\epsilon - \alpha t} \cos{(\omega_1 t + \gamma)} \\ q_2 &= \frac{1}{\epsilon - \alpha t} \sin{(2\omega_1 t + 2\gamma)} \\ p_2 &= \frac{1}{\epsilon - \alpha t} \cos{(2\omega_1 t + 2\gamma)}. \end{aligned} \tag{2.4}$$

Note that these solutions diverge in finite time. This behavior is known as explosive growth and is found in systems with positive and negative energy modes in resonance. When the resonance condition does not exist, solutions diverge only above critical amplitudes. Figure 2.1, adapted from [70], demonstrates this phenomena. Note the similarity between the surface of section for Cherry's Hamiltonian in this figure, and the phase portraits of the cubic and quadratic mappings introduced in Chap. 3 (Figures 3.1 and 3.4). Indeed, the coupled cubic-quadratic mapping was devised to mimic the explosive growth found in systems with Negative Energy Modes, exemplified by Cherry's example and the wave-wave resonance interactions commonly found in plasma systems.

2.2.2 Wave-Wave Problems in Plasma Physics

The general Hamiltonian for a three-wave resonance is

$$H = \omega_1 J_1 - \omega_2 J2 + \sigma\omega_3 J_3 + \alpha\sqrt{J_1 J_2 J_3}\sin{(\theta_1 + \theta_2 - \sigma\theta_3)}. \tag{2.5}$$

See [137, 70, 70, 71] for further discussion, among others. Nopte that $\sigma = 1$

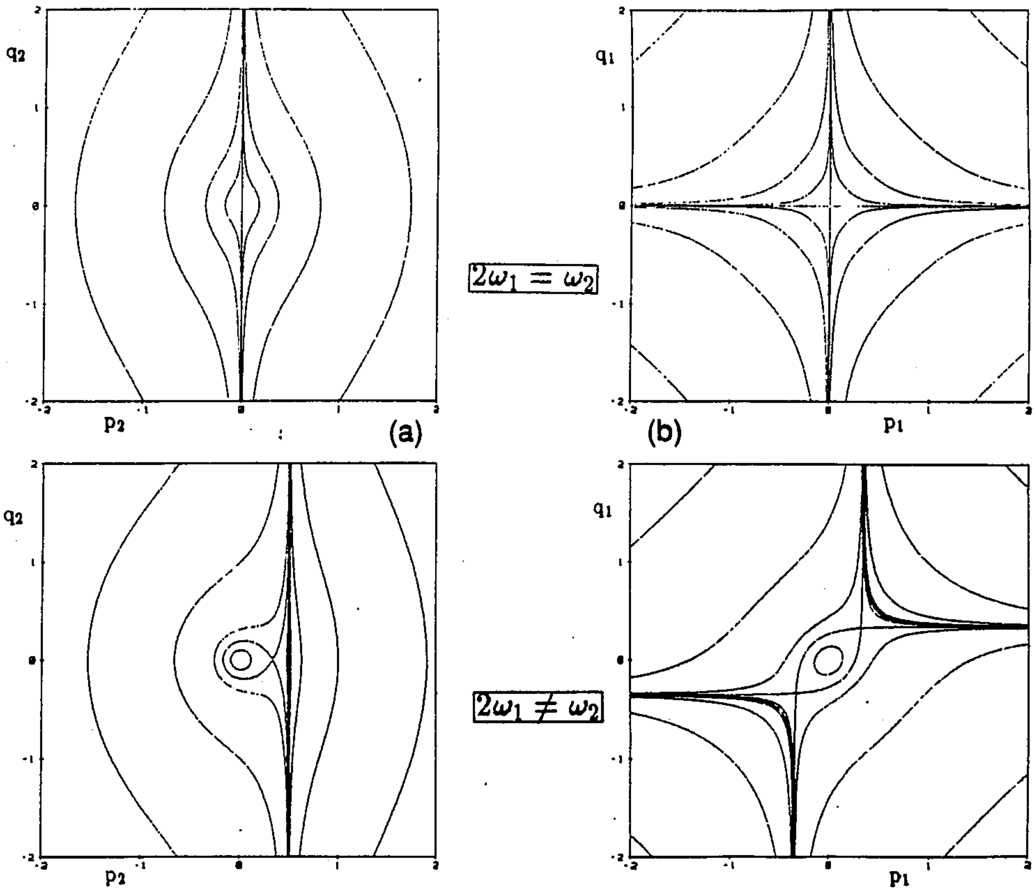

Figure 2.1: Poincaré sections for Cherry's Hamiltonian. Instersections of the orbits with the q_1 plane (a) and $q_2 = 0$ (b) for the resonant ($2\omega_1 = \omega_2$) and non-resonant cases. Figure adapted from [70]. The resonance condition results in explosive growth, while non-resonance means that solutions diverge only above some critical amplitude. We will mimic this behavior with a symplectic mapping introduced in the following chapter.

signifies a positive energy resonance, and $\sigma = -1$ a negative energy resonance. With an appropriate canonical transformation and judicious choice of constants [70], the above can be written as

$$H = \frac{1}{2}(\omega_1 - \omega_2)I_1 + \sigma\omega_3 I_3 + \frac{\alpha}{2} I_1 \sqrt{I_3} \sin{(2\psi_1 - \sigma\psi_3)}, \tag{2.6}$$

which becomes a two-wave resonance for $\sigma = 1$. For $\sigma = -1$, we recover the form of Cherry's Hamiltonian from the previous section.

2.2.3 FLR Stabilization

As a model of finite Larmor radius (FLR) stabilization [102, 106, 107], consider a particle subjected to a uniform, inverted harmonic potential (as may arise from MHD equilibrium) and a uniform magnetic field in the z-direction. The Hamiltonian may be written as

$$H = -\frac{1}{2}(p_1^2 + p_2^2) + \omega_L(q_2 p_1 - q_1 p_1) + \frac{1}{2}(\omega_L^2 - \omega_0^2)(q_1^2 + q_2^2) + V_3, \tag{2.7}$$

where V_3 is an anharmonic contribution to the potential with terms of order three, ω_L is the Larmor frequency $eB/2mc$, and ω_0 is the natural frequency $\sqrt{k/m}$. Upon a canonical transformation, this Hamiltonian has a standard negative energy mode,

$$H = -\frac{1}{2}\omega_1(P_1^2 + Q_1^2) + \frac{1}{2}\omega_2(P_2^2 + Q_2^2) + V_3, \tag{2.8}$$

and V_3 is now a function of the new coordinates. When energy is dissipated from this system, the negative energy modes are destabilized. Further, upon the standard Hamiltonian perturbation method of averaging, and under the resonance condition $2\omega_1 = \omega_2$, we recover Cherry's Hamiltonian (Eq. 2.2). As we have seen above, Cherry's system is spectrally stable, but globally unstable as the nonlinearity of the system diverts energy from the negative energy mode to the positive.

Chapter 3

The Coupled Cubic-Quadratic Mapping

3.1 Introduction

As alluded to in the previous chapter, to mimic the the explosive growth found in Hamiltonian systems with Negative Energy Modes such as Cherry's example and wave-wave interactions in plasma physics, we couple the symplectic (area-preserving) cubic and quadratic mappings introduced in Chap. 1 via a type 1 generating function $F(q_{old}, q_{new})$ [2, 62]. Note that, although it is common in the literature for q and p to represent the old coordinates, and Q and P the new, here we reserve (q, Q, p, P) for the coordinates of the coupled map. In the case of a type 1 generating function, the new equations are

$$p_{old} = \frac{\partial F}{\partial q_{old}}, \qquad p_{new} = -\frac{\partial F}{\partial q_{new}}, \tag{3.1}$$

and it is customary to invert the first equation for the p_{old} to obtain equations for the new canonical coordinates. We now illustrate this procedure for the uncoupled cubic and quadratic maps and demonstrate how the coupled cubic-quadratic map is derived from a generating function with the simplest type of coupling.

3.2 Generating the Cubic Map

We write the generating function for a cubic map as

$$F_{cubic} = \quad qq' + tq^2/2 + q^4/4. \tag{3.2}$$

For a type 1 generating function, with q' taking the place of q_{n+1}, the equations are

$$\begin{aligned} p &= \frac{\partial F}{\partial q} = q' + tq + q^3 \\ p' &= -\frac{\partial F}{\partial q'} = -q. \end{aligned} \tag{3.3}$$

This yields the equations for the symplectic (area-preserving) cubic mapping

$$\begin{aligned} p' &= -q \\ q' &= p - tq - q^3. \end{aligned} \tag{3.4}$$

3.3 Generating the Quadratic Map

We write the generating function for a quadratic map as

$$F_{quadratic} = \quad QQ' + \tau Q^2/2 + Q^3/3. \tag{3.5}$$

For a type 1 generating function, with Q' taking the place of Q_{n+1}, the equations are

$$\begin{aligned} P &= \frac{\partial F}{\partial Q} = Q' + \tau Q + Q^2 \\ P' &= -\frac{\partial F}{\partial Q'} = -Q. \end{aligned} \tag{3.6}$$

This yields the equations for the symplectic quadratic mapping

$$\begin{aligned} P' &= -Q \\ Q' &= P - \tau Q - Q^2. \end{aligned} \tag{3.7}$$

3.4 Generating the Coupled Mapping

To generate the coupled cubic-quadratic mapping from the cubic and quadratic maps previously given, we choose the simplest type of coupling aqQ, where a controls the strength of the coupling. Then one such generating function for the coupled cubic-quadratic mapping is

$$F_{coupled} = \quad qq' + QQ' + tq^2/2 + \tau Q^2/2 + Q^3/3 + q^4/4 + aqQ. \tag{3.8}$$

We have

$$\begin{aligned} p &= \frac{\partial F}{\partial q} = q' + tq + q^3 + aQ \\ p' &= -\frac{\partial F}{\partial q'} = -q \\ P &= \frac{\partial F}{\partial Q} = Q' + \tau Q + Q^2 + aq \\ P' &= -\frac{\partial F}{\partial Q'} = -Q. \end{aligned} \tag{3.9}$$

and the equations for the coupled map are

$$\begin{aligned} p' &= -q \\ q' &= p - tq - q^3 - aQ \\ P' &= -Q \\ Q' &= P - \tau Q - Q^2 - aq. \end{aligned} \tag{3.10}$$

We shall refer to Eq. (3.10) as the first form or Form$_1$ of the mapping. Let us take

$$t = 1.1, \qquad \tau = .9864, \qquad a = 0.01. \tag{3.11}$$

Then we have

$$\begin{aligned} p' &= -q \\ q' &= p - 1.1q - q^3 - .01Q \\ P' &= -Q \\ Q' &= P - .9864Q - Q^2 - .01Q. \end{aligned} \tag{3.12}$$

Now let $(P', Q') \rightarrow (-Q', -P')$ and $a \rightarrow -a$. The new generating function and governing equations are

$$F_{coupled_2} = \quad qq' - QQ' + tq^2/2 + \tau Q^2/2 + Q^3/3 + q^4/4 - aqQ \tag{3.13}$$

$$\begin{aligned} p &= \frac{\partial F}{\partial q} = q' + tq + q^3 - aQ \\ p' &= -\frac{\partial F}{\partial q'} = -q \\ P &= \frac{\partial F}{\partial Q} = -Q' + \tau Q + Q^2 - aq \\ P' &= -\frac{\partial F}{\partial Q'} = Q. \end{aligned} \tag{3.14}$$

The new equations for the coupled map are

$$\begin{aligned} p' &= -q \\ q' &= p - tq - q^3 + aQ \\ P' &= Q \\ Q' &= -P + \tau Q + Q^2 - aq. \end{aligned} \tag{3.15}$$

This is an alternative form of the mapping that we shall refer to as the second form or Form$_2$. Interesting orbits were obtained with this mapping for $t = 1.1$, $\tau = 1.1$, $a = 0.1$ that are similar to those found in [102].

Notice that if we let let $(P', Q') \to (-Q', -P')$ in the second form, and choose

$$t = 1.1, \qquad \tau = .9864, \qquad a = -0.01 \tag{3.16}$$

then we recover Eq. (3.12).

3.5 The Cubic Map

The cubic map is

$$\begin{aligned} p' &= -q \\ q' &= p - qt - q^3. \end{aligned} \tag{3.17}$$

Here we take $t = 1.1$, for reasons that will be discussed further in Chap. 2. Figures 3.1 and 3.2 show the phase portrait and frequencies of the cubic map, respectively, and Figure 3.3 shows a series of phase portraits for increasing t. Note that the $\frac{3}{8}$ resonance corresponds to the flat region of Figure 3.2. This corresponds to the island region in the phase portrait around $(p, q) \approx (.6, .6)$. The map is centered around an elliptical fixed point at $(0, 0)$, which is stable, and there are two hyperbolic fixed points at $(-1, -1)$ and (1,1). Trajectories with initial conditions greater than the critical values (p_{cr}, q_{cr}) escape to infinity (Figure 3.1).

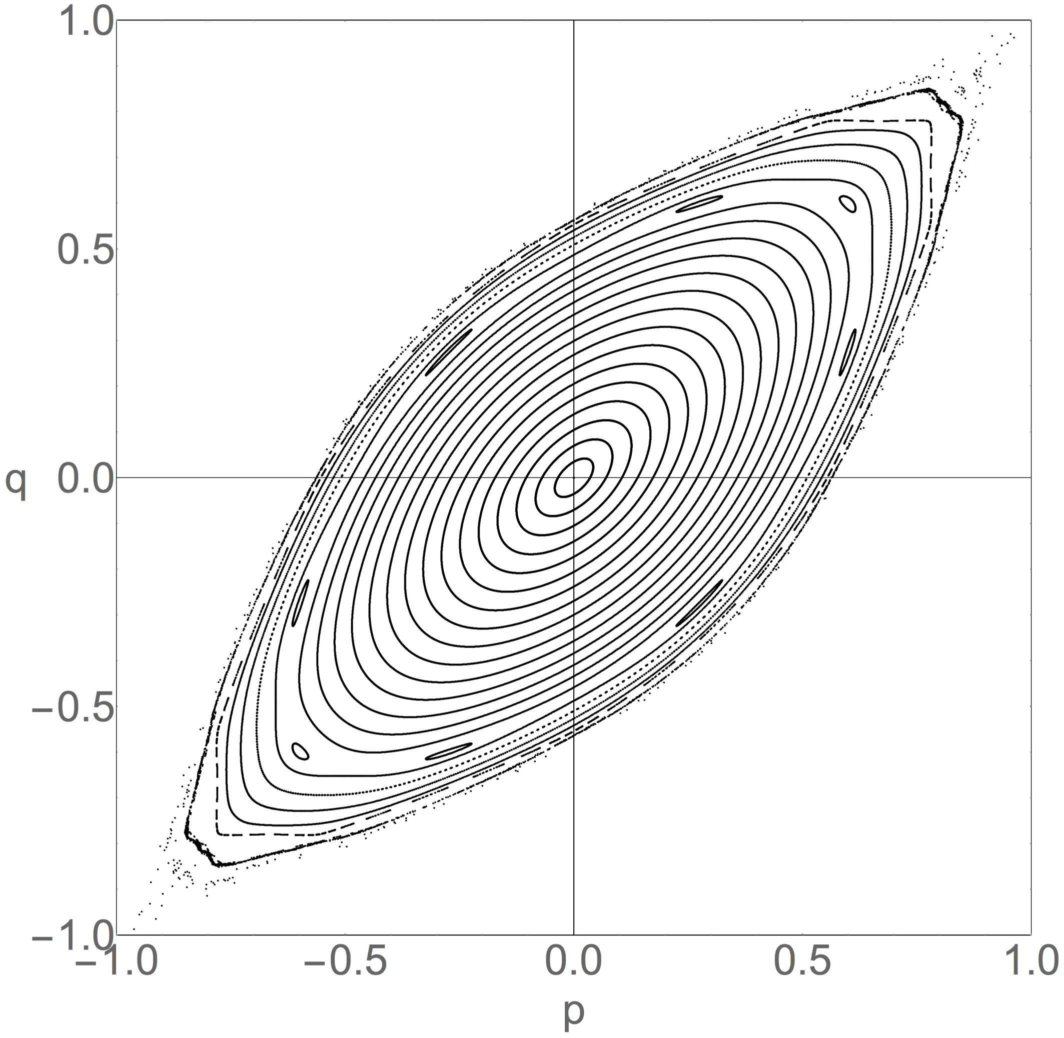

Figure 3.1: Phase portrait of the uncoupled cubic map. We utilize a symplectic mapping to mimic the explosive behavior found in systems with Negative Energy Modes, such as Cherry's Hamiltonian and wave-wave problems in plasma physics. Note the resemblance to the surface of section in Figure 2.1. For an appropriate parameter value t, solutions diverge above a critical amplitude.

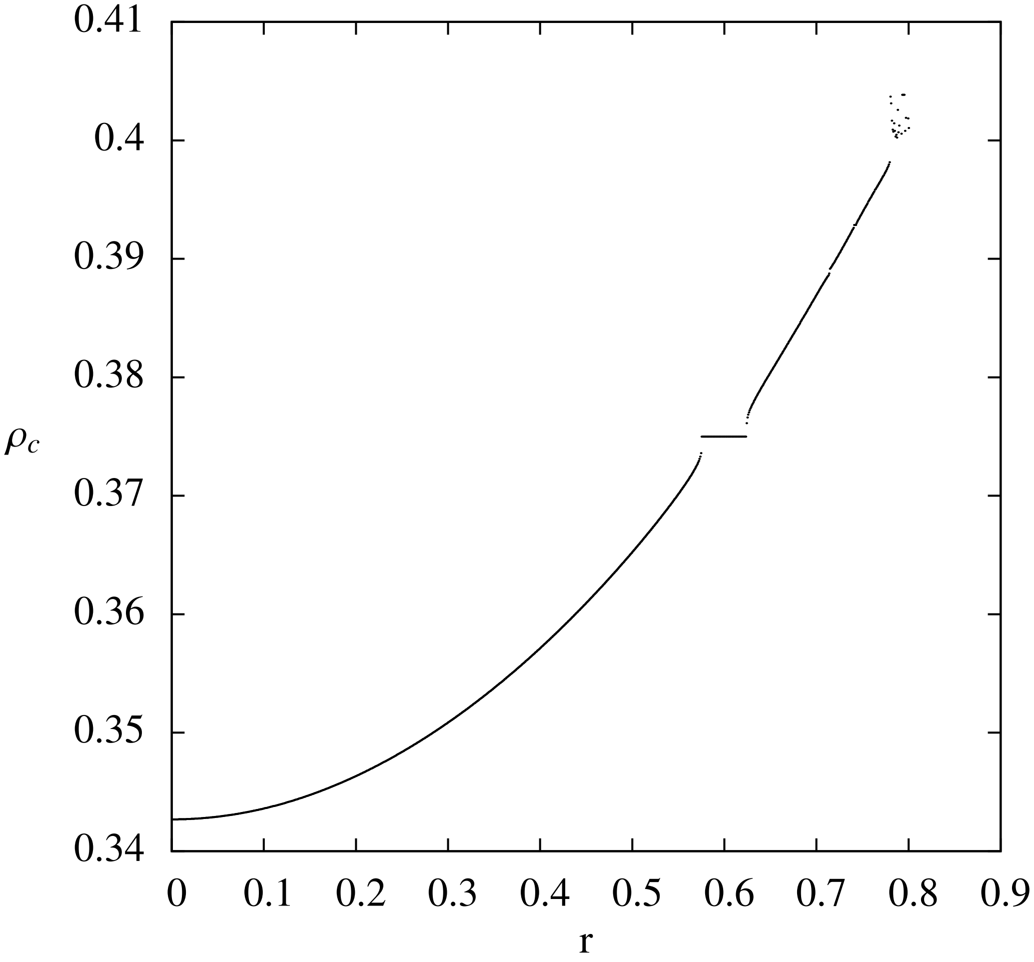

Figure 3.2: Rotation numbers (frequencies) of the uncoupled cubic map.

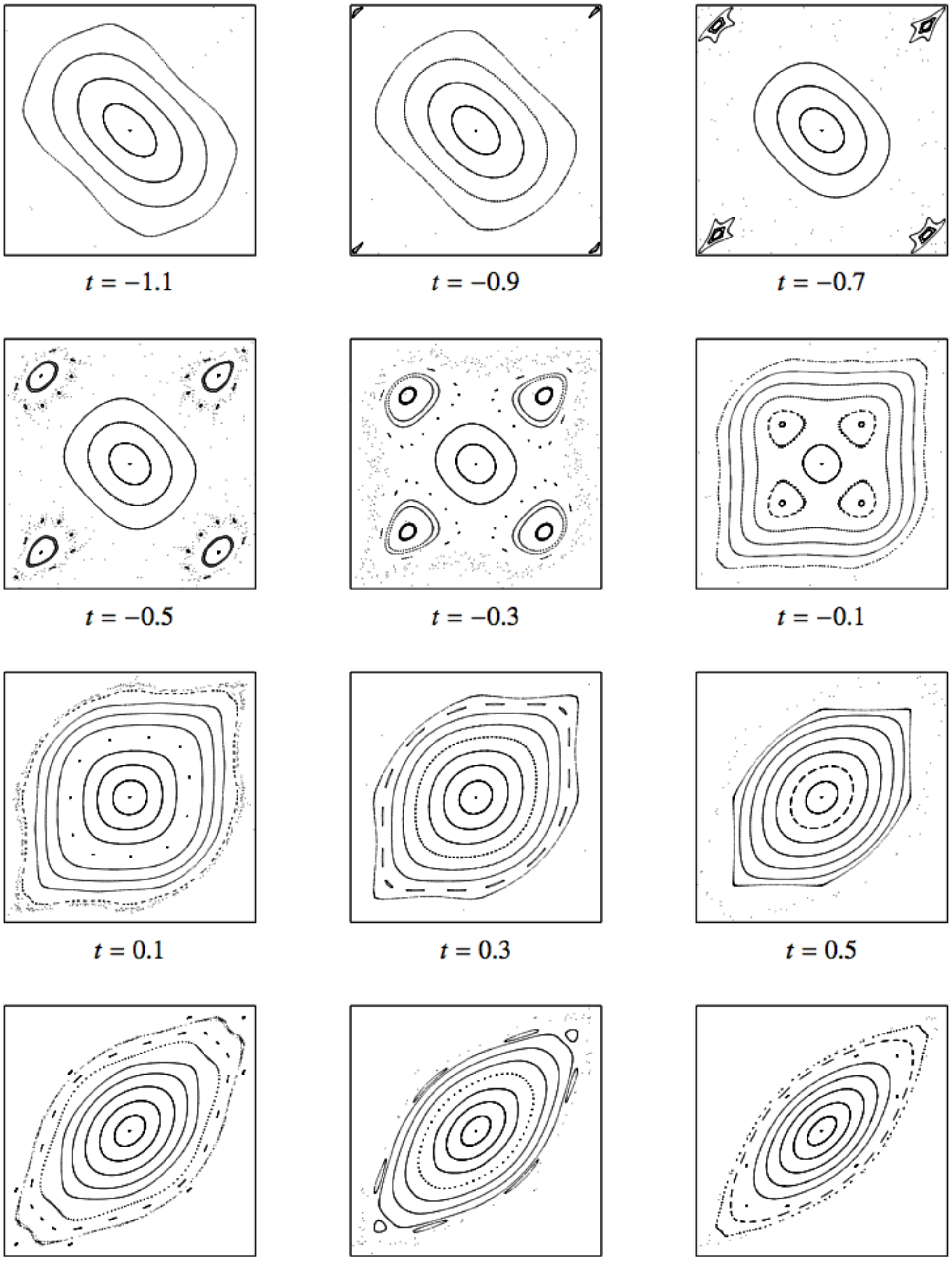

$t = -1.1$ $t = -0.9$ $t = -0.7$

$t = -0.5$ $t = -0.3$ $t = -0.1$

$t = 0.1$ $t = 0.3$ $t = 0.5$

$t = 0.7$ $t = 0.9$ $t = 1.1$

Figure 3.3: Phase portraits of the cubic map for increasing t.

3.6 The Quadratic Map

The quadratic map is

$$
\begin{aligned}
P' &= -Q \\
Q' &= P - Q\tau - Q^2. \qquad (3.18)
\end{aligned}
$$

Figure 3.6 shows a series of phase portraits for increasing τ. The phase portrait and frequencies of the quadratic map for $\tau = .9864$ are shown in Figures 3.4 and 3.5, respectively. Essentially an island region centered around a fixed point, the quadratic map also contains trajectories that can escape to infinity (Figure 3.4).

3.7 Generalized Polynomial Mappings

An alternative derivation of the area-preserving cubic, area-preserving quadratic, and symplectic 4D coupled map is to rely upon the normal form for a generalized polynomial mapping, as given by Engels [24, 25]. One may then choose appropriate constants to arrive at two respective (cubic and quadratic) families of one parameter maps, and couple these maps by preserving symplecticity. To introduce Engel's form for the general polynomial mapping, we review Hénon's derivation of the generalized quadratic mapping. Note that our quadratic mapping is simpler than Hénon's fully generalized polynomial mapping, as we choose to let some terms vanish (below).

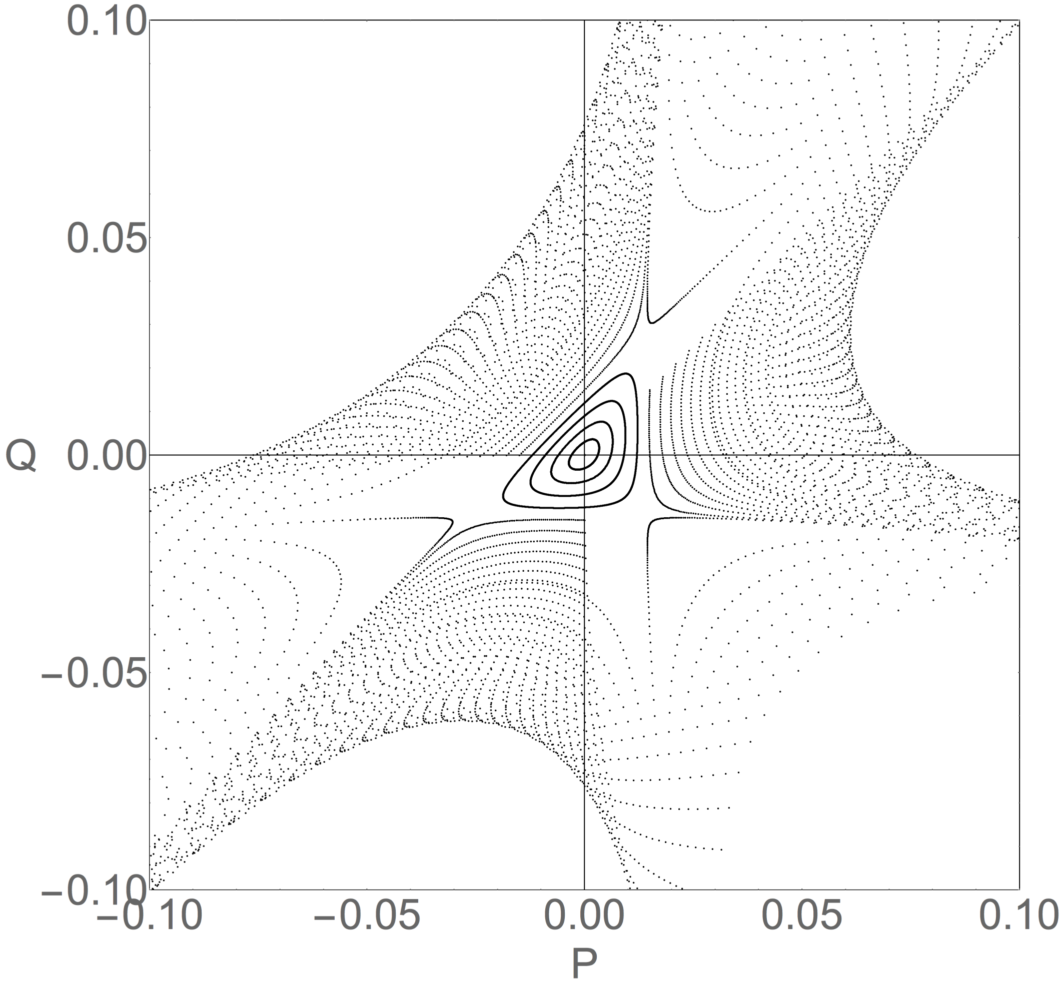

Figure 3.4: Phase portrait of the uncoupled quadratic map. We utilize a symplectic mapping to mimic the explosive behavior found in systems with Negative Energy Modes, such as Cherry's Hamiltonian and wave-wave problems in plasma physics. Note the resemblance to the surface of section in Figure 2.1.

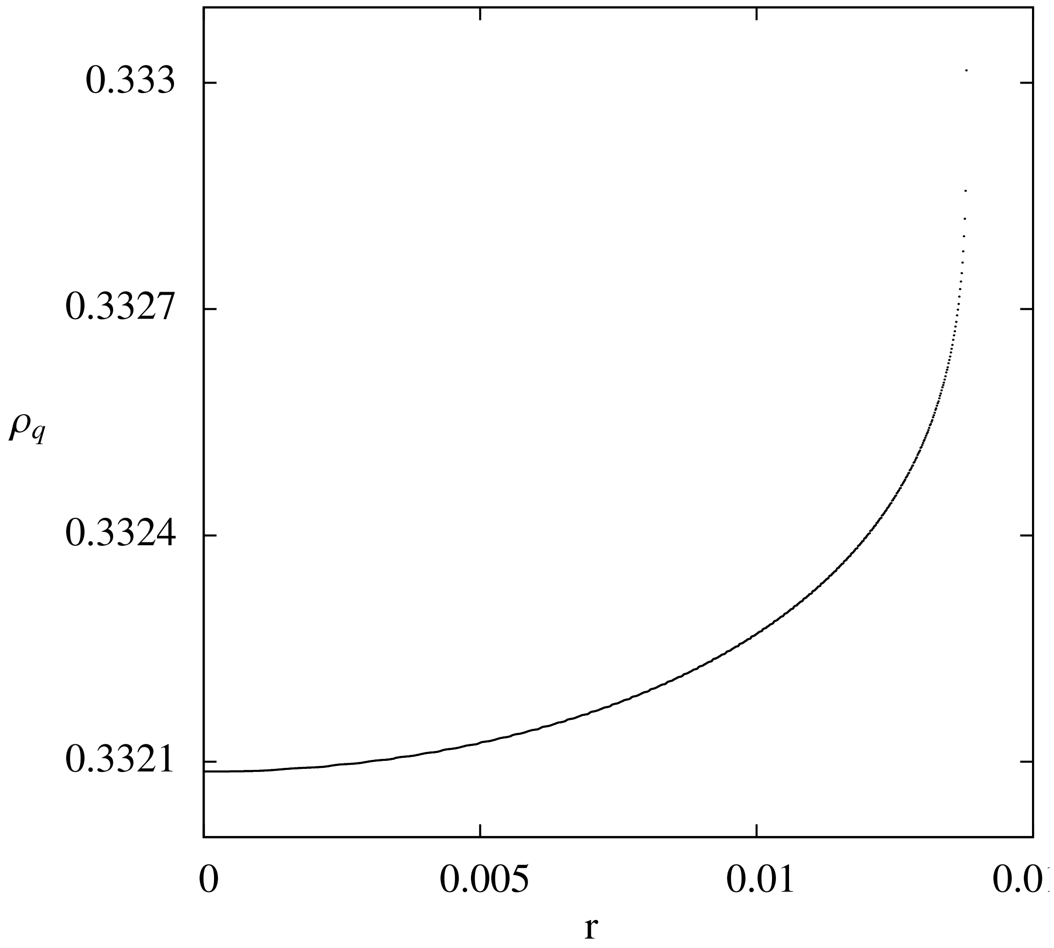

Figure 3.5: Rotation numbers (frequencies) of the uncoupled quadratic map.

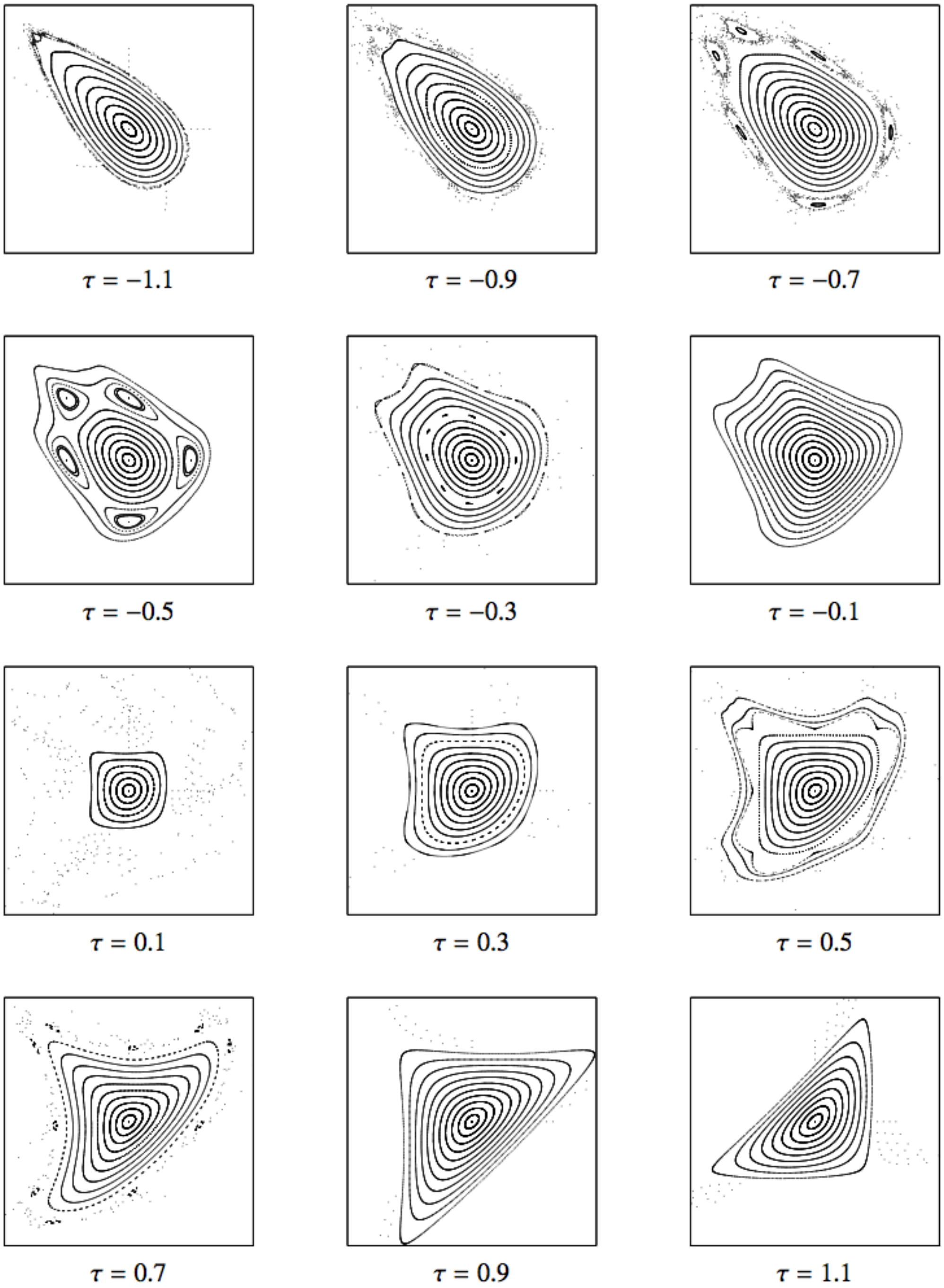
$\tau = -1.1$
$\tau = -0.9$
$\tau = -0.7$
$\tau = -0.5$
$\tau = -0.3$
$\tau = -0.1$
$\tau = 0.1$
$\tau = 0.3$
$\tau = 0.5$
$\tau = 0.7$
$\tau = 0.9$
$\tau = 1.1$

Figure 3.6: Phase portraits of the quadratic map for increasing τ.

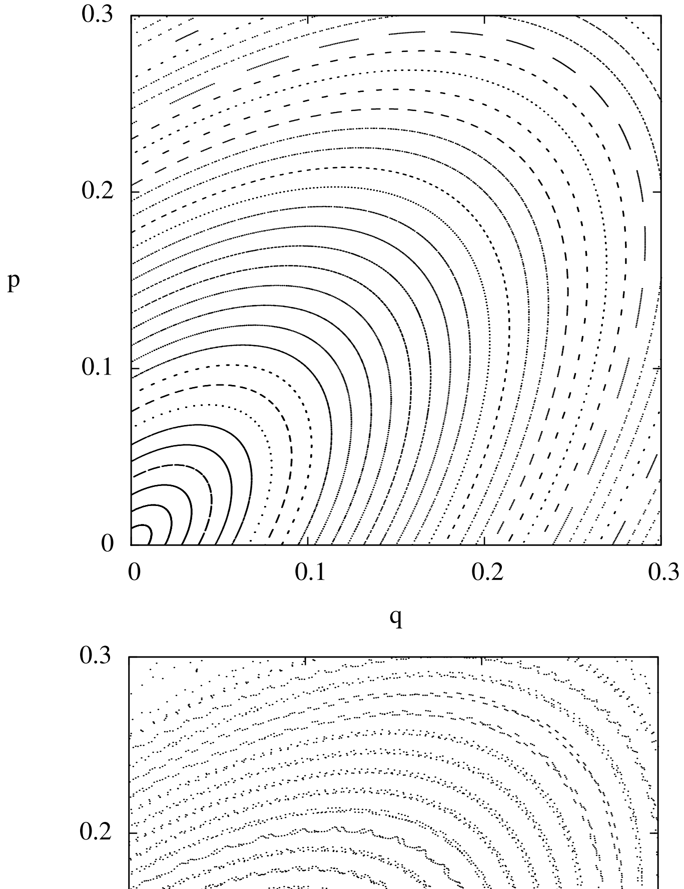

Figure 3.7: The effect of coupling on the phase portrait. Uncoupled (a) and coupled (b) orbits in the $p - q$ plane. Trajectories were plotted at regularly space intervals in the $p - q$ plane (a) and (P, Q) was held constant at $(0, 0)$ to illustrate the effects of coupling (b).

The popular and well known “Hénon Map” [52],

$$x' = y + 1 - ax^2, \qquad y = bx, \tag{3.19}$$

designed to mimic the Lorenz [85] attractor, is the most general quadratic mapping with a constant Jacobian and for $b = -1$ is area-preserving (but no longer contains a strange attractor). However, in an earlier (1969) paper [51] M. Hénon derived the general quadratic mapping that is “in a sense the simplest nontrivial mapping”. In his derivation, Hénon referenced work by Engel [24, 25] showing that any polynomial area-preserving mapping T can be written as the product of two simpler mappings: $T = RS$, where R represents a rotation, and S is a shearing. Here we briefly reproduce part of his derivation and compare it to Engel’s form for the general polynomial area-preserving map and our quadratic mapping. Our intent is mainly to demonstrate the simplicity of our chosen cubic and quadratic maps.

Hénon begins with the mapping

$$x' = f(x, y), \qquad y_1 = g(x, y) \tag{3.20}$$

and reminds us that, for the simplest case of $f(x, y)$ and $g(x, y)$ being linear polynomials (which also speeds up computation times), a coordinate transformation reduces the mapping to a simple rotation about the origin:

$$x' = x\cos(\theta) - y\sin(\theta), \qquad y' = x\sin(\theta) + y\cos(\theta), \tag{3.21}$$

where θ is a constant. Moving to the next degree in f and g, we have the general quadratic mapping

$$\begin{aligned} x' &= ax + by + cx^2 + dxy + ey^2 \\ y' &= a'x + b'y + c'x^2 + d'xy + e'y^2. \end{aligned} \tag{3.22}$$

Hénon then uses the area-preserving condition and a linear change of coordinates to transform this mapping to a one parameter mapping (instead of the ten coefficients above)

$$\begin{aligned} x' &= x\cos(\theta) - (y - x^2)\sin(\theta) \\ y' &= x\sin(\theta) + (y - x^2)\cos(\theta), \end{aligned} \tag{3.23}$$

which is a product of the shearing

$$x_S = x, \qquad y_S = y - x^2, \tag{3.24}$$

and the rotation

$$\begin{aligned} x' &= x_S\cos(\theta) - y_S\sin(\theta) \\ y' &= x_S\sin(\theta) + y_S\cos(\theta). \end{aligned} \tag{3.25}$$

Engel's form for the general polynomial area-preserving map is

$$\begin{aligned} x' &= g_0 + g_{10}x + g_{01}y + \beta\sum_{\kappa=2}^{p} a_\kappa[(\alpha g_{10} - \beta h_{10})x + (\alpha g_{01} - \beta h_{01})y]^\kappa \\ x' &= g_0 + g_{10}x + g_{01}y + \beta\sum_{\kappa=2}^{p} a_\kappa[(\alpha g_{10} - \beta h_{10})x + (\alpha g_{01} - \beta h_{01})y]^\kappa \end{aligned} \tag{3.26}$$

with $g_{10}h_{01} - g_{01}h_{10} \neq 0$. From this equation, we can see that the general area preserving map with a given linear and cubic term has two free parameters. In our case we have set one of those parameters (α) to be zero. This leaves us with a one parameter cubic mapping. Similarly, by making the appropriate choices in the normal form we end up with a one parameter (τ) family of quadratic maps. To couple the maps, we choose a coupling term that preserves the symplecticity of the map.

Table 3.1: Initial conditions for Figure 3.8. As we move down the table, the initial conditions increase in p and q, corresponding to the orbits in Figure 3.8 from left to right, top to bottom. Here $a = .01, t = 1.1, \tau = .9864$

p	q	P	Q
0.6400000000000000	0.6400000000000000	0.0000000000000000	0.0000000000000000
0.6420000000000000	0.6420000000000000	0.0000000000000000	0.0000000000000000
0.6440000000000000	0.6440000000000000	0.0000000000000000	0.0000000000000000
0.6460000000000000	0.6460000000000000	0.0000000000000000	0.0000000000000000
0.6480000000000000	0.6480000000000000	0.0000000000000000	0.0000000000000000
0.6500000000000000	0.6500000000000000	0.0000000000000000	0.0000000000000000
0.6520000000000000	0.6520000000000000	0.0000000000000000	0.0000000000000000
0.6540000000000000	0.6540000000000000	0.0000000000000000	0.0000000000000000
0.6560000000000000	0.6560000000000000	0.0000000000000000	0.0000000000000000
0.6580000000000000	0.6580000000000000	0.0000000000000000	0.0000000000000000
0.6600000000000000	0.6600000000000000	0.0000000000000000	0.0000000000000000
0.6620000000000000	0.6620000000000000	0.0000000000000000	0.0000000000000000
0.6640000000000000	0.6640000000000000	0.0000000000000000	0.0000000000000000
0.6660000000000000	0.6660000000000000	0.0000000000000000	0.0000000000000000
0.6680000000000000	0.6680000000000000	0.0000000000000000	0.0000000000000000
0.6700000000000000	0.6700000000000000	0.0000000000000000	0.0000000000000000
0.6720000000000000	0.6720000000000000	0.0000000000000000	0.0000000000000000
0.6740000000000000	0.6740000000000000	0.0000000000000000	0.0000000000000000
0.6760000000000000	0.6760000000000000	0.0000000000000000	0.0000000000000000
0.6780000000000000	0.6780000000000000	0.0000000000000000	0.0000000000000000
0.6800000000000000	0.6800000000000000	0.0000000000000000	0.0000000000000000
0.6820000000000001	0.6820000000000001	0.0000000000000000	0.0000000000000000
0.6840000000000001	0.6840000000000001	0.0000000000000000	0.0000000000000000
0.6860000000000001	0.6860000000000001	0.0000000000000000	0.0000000000000000

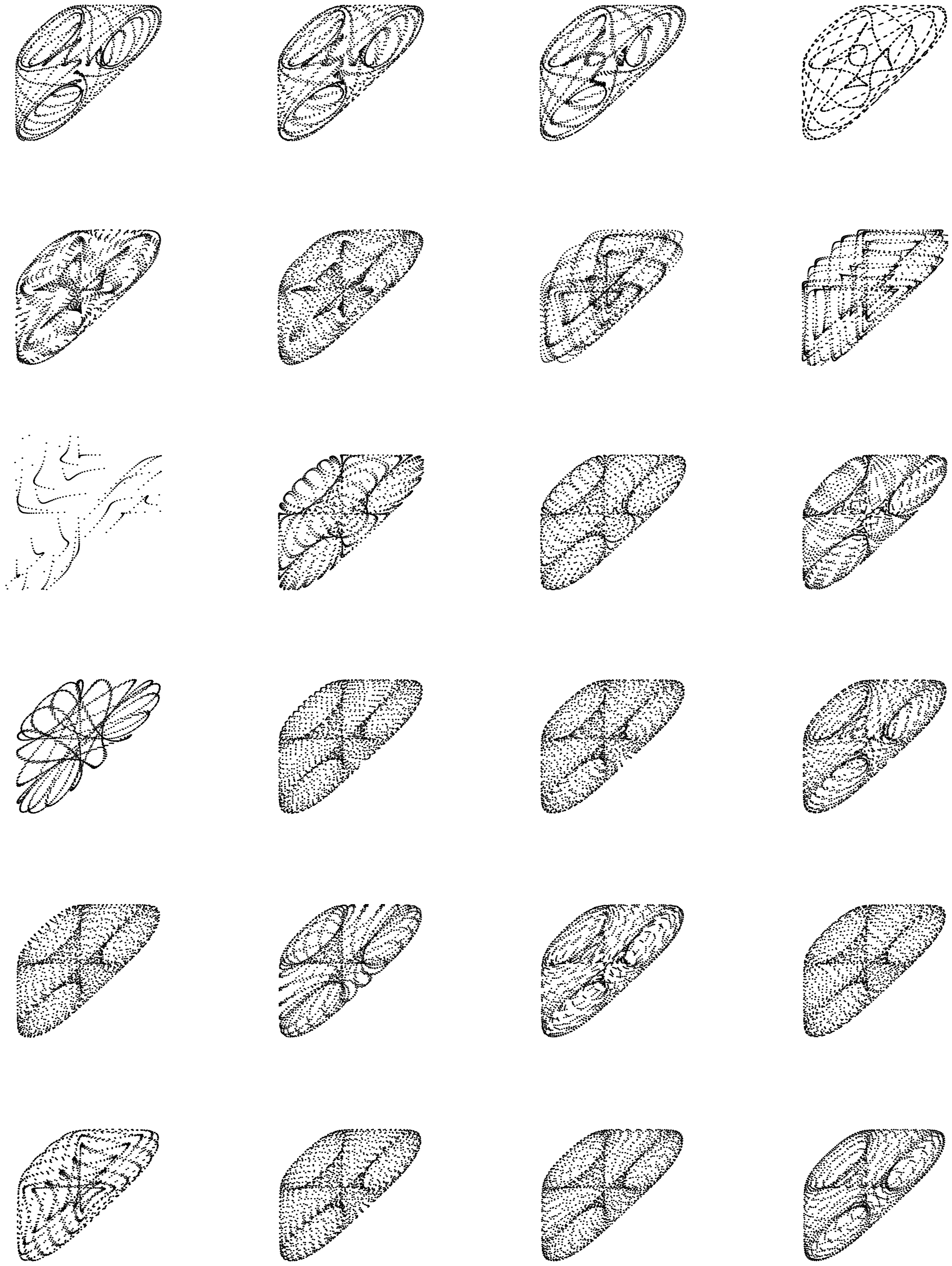

Figure 3.8: Phase portraits of the coupled cubic-quadratic map (I). The map was iterated 2^{11} times for each initial condition and the results plotted in the $P-Q$ plane (see the explanation of Table 3.1).

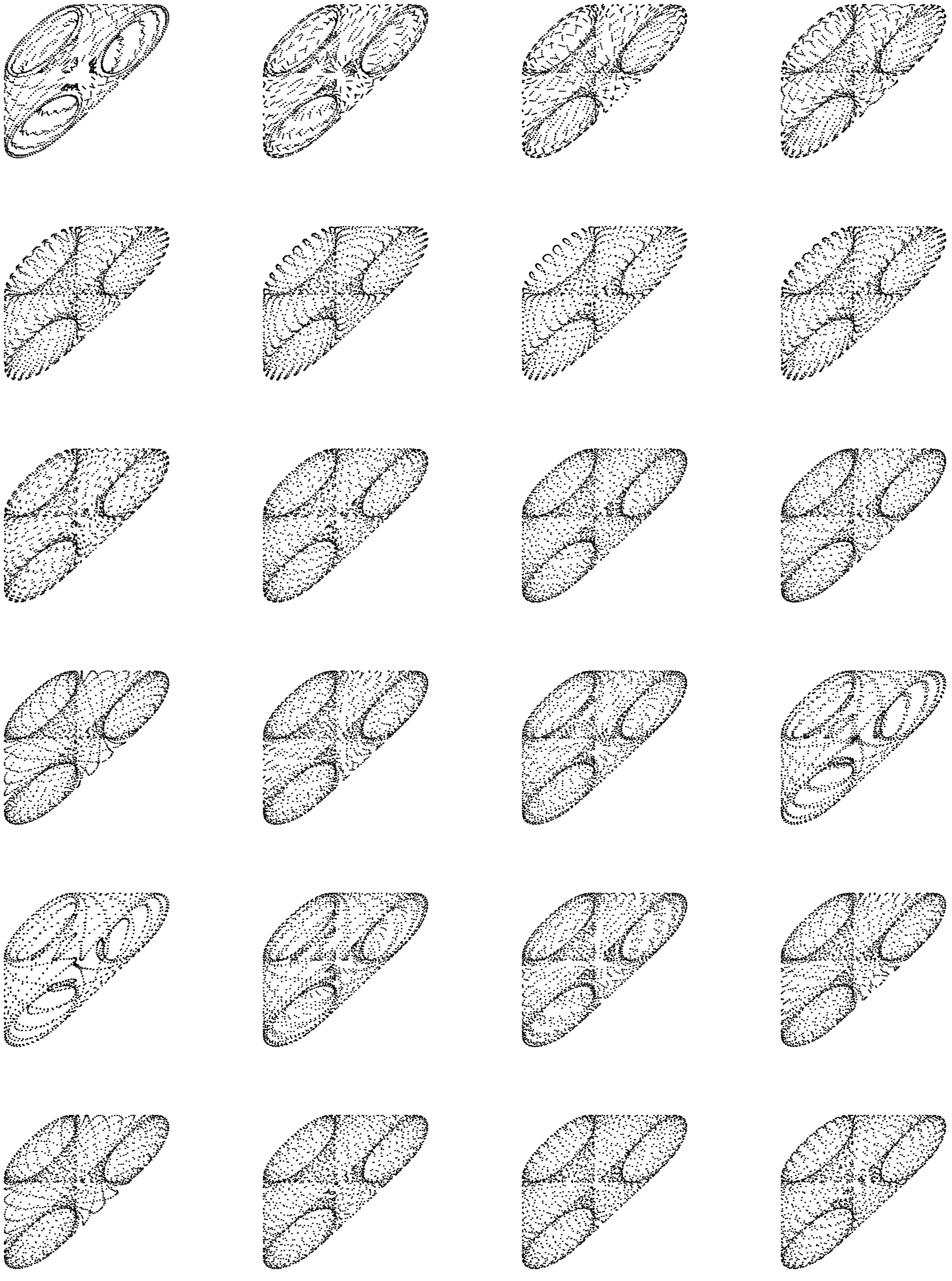

Figure 3.9: Phase portraits of the coupled cubic-quadratic map (II). The process is identical to that of Figure 3.8, except the initial conditions scan in P. See the explanation of Table 3.2 and the following discussion.

Table 3.2: Initial conditions for Figure 3.9. As we move down the table, the initial conditions increase in P, corresponding to the orbits in Figure 3.9 from left to right, top to bottom. Here $a = .01, t = 1.1, \tau = .9864$

p	q	P	Q
0.6400000000000000	0.6400000000000000	0.0010000000000000	0.0000000000000000
0.6400000000000000	0.6400000000000000	0.0015000000000000	0.0000000000000000
0.6400000000000000	0.6400000000000000	0.0020000000000000	0.0000000000000000
0.6400000000000000	0.6400000000000000	0.0025000000000000	0.0000000000000000
0.6400000000000000	0.6400000000000000	0.0030000000000000	0.0000000000000000
0.6400000000000000	0.6400000000000000	0.0035000000000000	0.0000000000000000
0.6400000000000000	0.6400000000000000	0.0040000000000000	0.0000000000000000
0.6400000000000000	0.6400000000000000	0.0045000000000000	0.0000000000000000
0.6400000000000000	0.6400000000000000	0.0050000000000000	0.0000000000000000
0.6400000000000000	0.6400000000000000	0.0055000000000000	0.0000000000000000
0.6400000000000000	0.6400000000000000	0.0060000000000000	0.0000000000000000
0.6400000000000000	0.6400000000000000	0.0065000000000000	0.0000000000000000
0.6400000000000000	0.6400000000000000	0.0070000000000000	0.0000000000000000
0.6400000000000000	0.6400000000000000	0.0075000000000000	0.0000000000000000
0.6400000000000000	0.6400000000000000	0.0080000000000000	0.0000000000000000
0.6400000000000000	0.6400000000000000	0.0085000000000000	0.0000000000000000
0.6400000000000000	0.6400000000000000	0.0090000000000000	0.0000000000000000
0.6400000000000000	0.6400000000000000	0.0095000000000000	0.0000000000000000
0.6400000000000000	0.6400000000000000	0.0100000000000000	0.0000000000000000
0.6400000000000000	0.6400000000000000	0.0105000000000000	0.0000000000000000
0.6400000000000000	0.6400000000000000	0.0110000000000000	0.0000000000000000
0.6400000000000000	0.6400000000000000	0.0115000000000000	0.0000000000000000
0.6400000000000000	0.6400000000000000	0.0120000000000000	0.0000000000000000
0.6400000000000000	0.6400000000000000	0.0125000000000000	0.0000000000000000

3.8 The Geometry of Phase Space

As previously demonstrated, there are two sub-planes of the four-dimensional space that are convenient to plot the dynamics of the map: $p - q$ and $P - Q$. Figures 3.7-3.9 show some examples of the types of orbits obtained for Form$_1$ of the mapping (Eq 3.10; $t = 1.1, \tau = .9864, a = .01$). For these parameters, the contribution from the quadratic mapping to the cubic via the coupling term is relatively small, and the contribution from the quadratic to the cubic is relatively large (cf. Figure 3.1 and 3.4). Notice that we obtain similar results in the $P - Q$ plane (Figure 3.8, Table 3.1) if we choose a number of orbits by scanning along the $p - q$ diagonal with $P - Q$ constant at $(0, 0)$, or if we hold (p, q) constant and scan the $P - Q$ orbits (Figure 3.9, Table 3.2). For these parameters, the orbits in the $P - Q$ sub-plane no longer appear regular, but highly convoluted[1]. In the $p - q$ sub-plane, the orbit may appear to have little or no change, but a closer look reveals the finer features due to the influence of the quadratic upon coupling (Figure 3.7).

In the following chapter, we will more closely examine the second form of the mapping (3.15). Figure 4.3 shows the phase portraits for Form$_2$ of the mapping with $t = 1.1$, $\tau = 1.1$, and $a = .1$. Note the qualitative difference resulting from the choice of parameters; for $t \sim \tau$, the respective uncoupled orbits have approximately the same amplitude, and there is no drastic effect

---

[1] Also see Figure 5.3 and others throughout this work.

of one upon the other (cf. Figures 3.7-3.9). In the phase portraits and the frequency analysis (Chap. 4), one observes orbits of a more diffusive nature in Form$_2$ of the mapping (when $t \sim \tau$) than Form$_1$.

In Chap. 5, we discuss a method for "unwinding" the convoluted projections in the lower dimensional sub-spaces. To reiterate, even if an orbit lies on a torus, in higher dimensions we cannot accurately obtain the rotation number (frequency) via the straightforward method of Eq. (1.36) if we cannot easily obtain the angles of successive iterations about some center. In addition, the complicated projections obtained in the sub-planes make it difficult to tell whether an orbit is in fact, a simple, closed curve. The dynamics occurs in higher dimensions upon coupling, and the orbit is projected into lower dimensions sub-planes, just as a three-dimensional object's shadow is projected onto a two-dimensional surface. The $p - q$ and $P - Q$ sub-planes are just one set of projections we may make, and in Chap. 5 we examine a process that allows us to untangle the projection to reveal orbits that are in fact, simple, closed curves in phase space (as expected for invariant tori). First, however, in Chap. 4 we introduce and apply the method of frequency analysis, which allows us to obtain the frequencies (rotation numbers) of orbits with or without transforming to a simple projection space.

Chapter 4

Frequency Analysis and Dynamical Systems

4.1 Introduction

In this chapter we introduce the method of frequency analysis as treated extensively by Laskar [80, 77, 78, 76, 75, 74, 127], and demonstrate the use of an improved method by Gomez [39, 40]. In Sec. 4.3.1, we use the frequency analysis method to obtain the well known Devils Staircase in the Chirikov-Taylor (Standard) Mapping. In the same section, we use sample data from known sinusoids and the integrable case of the Standard Map to demonstrate that the frequencies obtained are accurate to 19 decimal places. We discuss the use of high precision computations used to obtain this result in Sec. 4.5. The standard in modern scientific computing is double precision, or 53 bits, corresponding to 15-17 decimal places. See [38] for an interesting discussion of precision and computing. We obtain the two-dimensional frequency map for the Froeschle Mapping, which agrees well with previous work [76], in Sec. 4.3.2. In Sec. 4.4, we apply the method of frequency analysis to the four-dimensional coupled cubic-quadratic mapping, obtaining the frequency map for two qualitatively different sets of parameters, and following the frequency of specific orbits for long time scales ($\sim 10^6$). In this manner, we provide evidence of higher dimensional transport phenomena that appears to demonstrate both diffusion along resonances and motion around tori. These phenomena are often referred to as Arnol'd Diffusion.

4.2 The Method of Frequency Analysis

The method of frequency analysis is a useful tool for the analysis of dynamical systems [80, 77, 78, 76, 75, 74, 127]. For a perturbed Hamiltonian system (Eq. (1.21)) with n degrees of freedom, the flow (recall Eqs. (1.1) and (1.14)) can take the form of a Fourier series on KAM tori [78],

$$z^i(t) = z^i_o e^{\mathrm{i}\omega^i t} + \sum_m a^i_j e^{\mathrm{i}m_k\omega^k t}, \tag{4.1}$$

where the a^i_j depend on the frequencies, and $m_k\omega^k = m_1\omega^1 + m_2\omega^2 + \ldots + m_n\omega^n$. To high accuracy, this can be represented by the *quasiperiodic approximation*,

$$z^i(t) = z^i_o e^{\mathrm{i}\omega^i t} + \sum_{j=1}^{N} a^i_{m_j} e^{\mathrm{i}m_j\omega^j t}, \tag{4.2}$$

to a desired accuracy by retaining N terms. Therefore, for some quasiperiodic function $f(t)$ obtained numerically, it is possible to obtain a quasiperidoc approximation of $f(t)$ to a high degree of accuracy by computing the Discrete Fourier Transform of $f(t)$ and obtaining the frequencies and amplitudes of (4.2). Improvements in accuracy were made by Laskar [80, 78] by seeking the maximum of a special function in frequency space,

$$\phi(\omega) = \int_0^T f(t)e^{-\mathrm{i}\omega t}. \tag{4.3}$$

Once the location of the first frequency is obtained, the contribution of the first frequency term is subtracted out from the quasiperiodic approximation and the process is repeated. In this manner, one can iteratively arrive at the quasiperiodic approximation. Data windowing by use of the Hanning Filter [12] reduces the displacement of each peak by perturbations from each of the other, ensuring that the frequencies are more accurately determined. It is believed [127, 78] that the accuracy of the frequencies determined by this method for a KAM orbit is on the order of $1/T^4$, instead of $1/T^2$ without a Hanning window and $1/T$ for an ordinary FFT.

Recently, further improvements [39, 40] in the method of frequency analysis have been made by Gomez, et al. Their method for the determination of the quasiperiodic approximation is based on a collocation method in frequency space, and is exact for finite trigonometric polynomials. Further, even when $f(t)$ contains infinitely many linear combinations of a basic frequency subset, the collocation method is able to determine a small number of frequencies with high precision. One of the goals of this work is to demonstrate the practical applicability of this method and test its accuracy and precision.

4.3 Frequency Analysis of Symplectic Mappings

4.3.1 Area-Preserving Mappings: The Standard Map

Recall that the standard map is

$$x_{n+1} = x_n + p_{n+1}\,, \qquad p_{n+1} = p_n + \frac{k}{2\pi}\sin(2\pi x_n) \tag{4.4}$$

and one can calculate (what we refer to as) both a rotation number and winding number (Sec. 1.5.1) of this system. Here we compare the calculations of these numbers using Eq. (1.36) and Eq. (1.38) to the values obtained from the method of frequency analysis.

As a test of the frequency method we use the case of $k = 0$, for which the map is integrable, to determine known frequencies to a high degree of accuracy. In this case, p is a constant of motion and the frequencies are equal to the initial p values. We can use this fact to test our numerics to a high degree of accuracy. If our initial p_o is known to many decimals, then a comparison of the frequency yields a measure of the accuracy of the method. Given a sufficient number of data points, we find that the frequencies are accurate to at least 19 decimals (Tables 4.1-4.2, Figure 4.1).

4.3.2 Higher Dimensional Mappings

4.3.2.1 The Froeschlé Map

As a test of the method, we generate the frequency map [76] of the Froeschlé Mapping of Eq. (1.46) for various values of the coupling parameter b. The results are shown in Figure 4.2. For $b = 0$, the maps are integrable and we observe a regular frequency space. Upon coupling, the 1:1 resonance appears and irregularities are observed, denoting regions of instability. As b increases, more and more tori are destroyed, which is reflected in the frequency mapping. In the following section, we will use the frequency map for the coupled cubic-quadratic mapping.

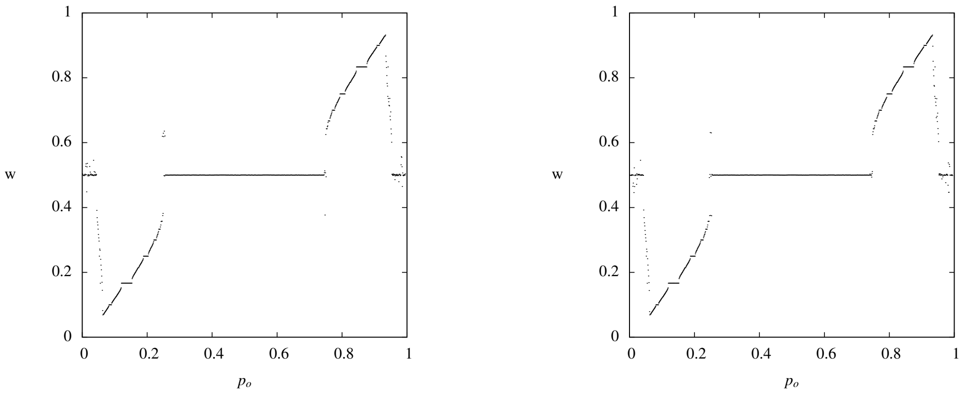

(a) $N = 2^{10}$ (b) $N = 2^{11}$

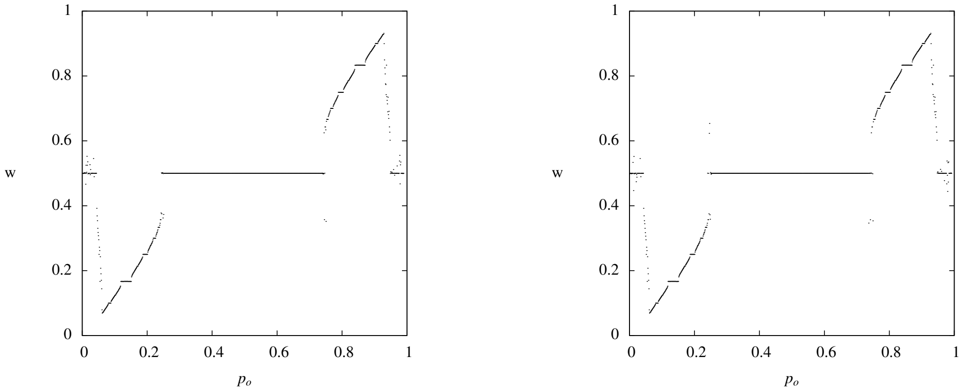

(c) $N = 2^{13}$ (d) $N = 2^{14}$

Figure 4.1: Frequencies and the devil's staircase in the standard map. Compare Figure 1.4. Increasing the number of samples N increases the accuracy of the calculated frequencies (cf. Table 4.1 and 4.2).

Table 4.1: Frequencies of the Integrable Standard Map, $k = 0$ (I). For $k = 0$, the frequencies of the standard map are the initial action-like values (p_o,first column). We compute the frequencies using the FFT collocation method for $N = 2^{10}$, 2^{14},2^{17}, and 2^{20}. This demonstrates that frequencies are accurate to nineteen decimal places.

p_o	ω (2^{10})	ω (2^{14})	ω (2^{17})	ω (2^{20})
0.0100000000000000000	0.0099999999999999991	0.0100000000000000000	0.0100000000000000000	0.0100000000000000000
0.0100000000000314159	0.0100000000000314158	0.0100000000000314159	0.0100000000000314159	0.0100000000000314159
0.0100000000000628319	0.0100000000000628316	0.0100000000000628319	0.0100000000000628319	0.0100000000000628319
0.0100000000000942478	0.0100000000000942471	0.0100000000000942478	0.0100000000000942478	0.0100000000000942478
0.0100000000001256637	0.0100000000001256631	0.0100000000001256637	0.0100000000001256637	0.0100000000001256637
0.0100000000001570796	0.0100000000001570780	0.0100000000001570796	0.0100000000001570796	0.0100000000001570796
0.0100000000001884956	0.0100000000001884943	0.0100000000001884956	0.0100000000001884956	0.0100000000001884956
0.0100000000002199115	0.0100000000002199107	0.0100000000002199115	0.0100000000002199115	0.0100000000002199115
0.0100000000002513274	0.0100000000002513257	0.0100000000002513274	0.0100000000002513274	0.0100000000002513274
0.0100000000002827433	0.0100000000002827424	0.0100000000002827433	0.0100000000002827433	0.0100000000002827433
0.0100000000003141593	0.0100000000003141572	0.0100000000003141593	0.0100000000003141593	0.0100000000003141593
0.0100000000003455752	0.0100000000003455744	0.0100000000003455752	0.0100000000003455752	0.0100000000003455752
0.0100000000003769911	0.0100000000003769895	0.0100000000003769911	0.0100000000003769911	0.0100000000003769911
0.0100000000004084070	0.0100000000004084060	0.0100000000004084070	0.0100000000004084070	0.0100000000004084070
0.0100000000004398230	0.0100000000004398221	0.0100000000004398230	0.0100000000004398230	0.0100000000004398230
0.0100000000004712389	0.0100000000004712385	0.0100000000004712389	0.0100000000004712389	0.0100000000004712389
0.0100000000005026548	0.0100000000005026535	0.0100000000005026549	0.0100000000005026548	0.0100000000005026548
0.0100000000005340708	0.0100000000005340696	0.0100000000005340707	0.0100000000005340707	0.0100000000005340707
0.0100000000005654867	0.0100000000005654850	0.0100000000005654866	0.0100000000005654867	0.0100000000005654867
0.0100000000005969026	0.0100000000005969012	0.0100000000005969026	0.0100000000005969026	0.0100000000005969026
0.0100000000006283185	0.0100000000006283187	0.0100000000006283185	0.0100000000006283185	0.0100000000006283185
0.0100000000006597345	0.0100000000006597338	0.0100000000006597345	0.0100000000006597345	0.0100000000006597345
0.0100000000006911504	0.0100000000006911500	0.0100000000006911504	0.0100000000006911504	0.0100000000006911504
0.0100000000007225663	0.0100000000007225650	0.0100000000007225664	0.0100000000007225663	0.0100000000007225663
0.0100000000007539822	0.0100000000007539815	0.0100000000007539822	0.0100000000007539823	0.0100000000007539822

4.3.2.2 The Coupled Cubic-Quadratic Map

Here we consider the four-dimensional cubic quadratic mapping introduced earlier. The uncoupled phase portraits and frequencies of the system are shown below. The subscripts denote frequencies of the cubic and quadratic maps, respectively, and we scan the frequencies along the 1:1 diagonal (r) from the origin (Figure 4.4).

Upon coupling ($a = .1$), we see that the respective regions around the resonances have become irregular (Figure 4.6), and frequencies around the higher resonances are missing. To determine the fate of these missing frequencies, we visualize the frequency map as suggested by Laskar [76]. For a grid of 90,000 initial conditions in four dimensions, we iterate the map for 2^{10} iterations, obtain the frequencies and plot the result for different values of the coupling constant a (Figure 4.7). In general, we find that as we increase the number of initial conditions, more stable orbits are observed in the frequency space. This matches the description given by KAM in which tori are pathologically distributed, but rare.

4.4 Evidence of Arnol'd Diffusion and Generalized Transport Phenomena

Here we describe some results related to the Arnol'd Diffusion (see Sec. 1.5, [18, 5]) and generalized motion around tori in the the higher dimensional phase space of the 4D mapping. In this chapter we focus on results related to the frequency analysis. In Chap. 6 we provide further evidence of motion

Table 4.2: Frequencies of the Integrable Standard Map, $k = 0$ (II). Frequencies computed over a greater range of initial conditions than the previous table. For $k = 0$, the frequencies of the standard map are the initial action-like values (p_o, first column). This demonstrates that frequencies are accurate to nineteen decimal places.

p_o	$\omega\ (2^{17})$
0.0010000000000000000	0.0010000000000000000
0.0410000000000000000	0.0410000000000000000
0.0810000000000000000	0.0810000000000000000
0.1210000000000000000	0.1210000000000000000
0.1610000000000000000	0.1610000000000000000
0.2010000000000000000	0.2010000000000000000
0.2410000000000000000	0.2410000000000000000
0.2810000000000000000	0.2810000000000000000
0.3210000000000000000	0.3210000000000000000
0.3610000000000000000	0.3610000000000000000
0.4010000000000000000	0.4010000000000000000
0.4410000000000000000	0.4410000000000000000
0.4810000000000000000	0.4810000000000000000
0.5210000000000000000	0.5210000000000000000
0.5610000000000000000	0.5610000000000000000
0.6010000000000000000	0.6010000000000000000
0.6410000000000000000	0.6410000000000000000
0.6810000000000000000	0.6810000000000000000
0.7210000000000000000	0.7210000000000000000
0.7610000000000000000	0.7610000000000000000
0.8010000000000000000	0.8010000000000000000
0.8410000000000000000	0.8410000000000000000
0.8810000000000000000	0.8810000000000000000
0.9210000000000000000	0.9210000000000000000
0.9610000000000000000	0.9610000000000000000

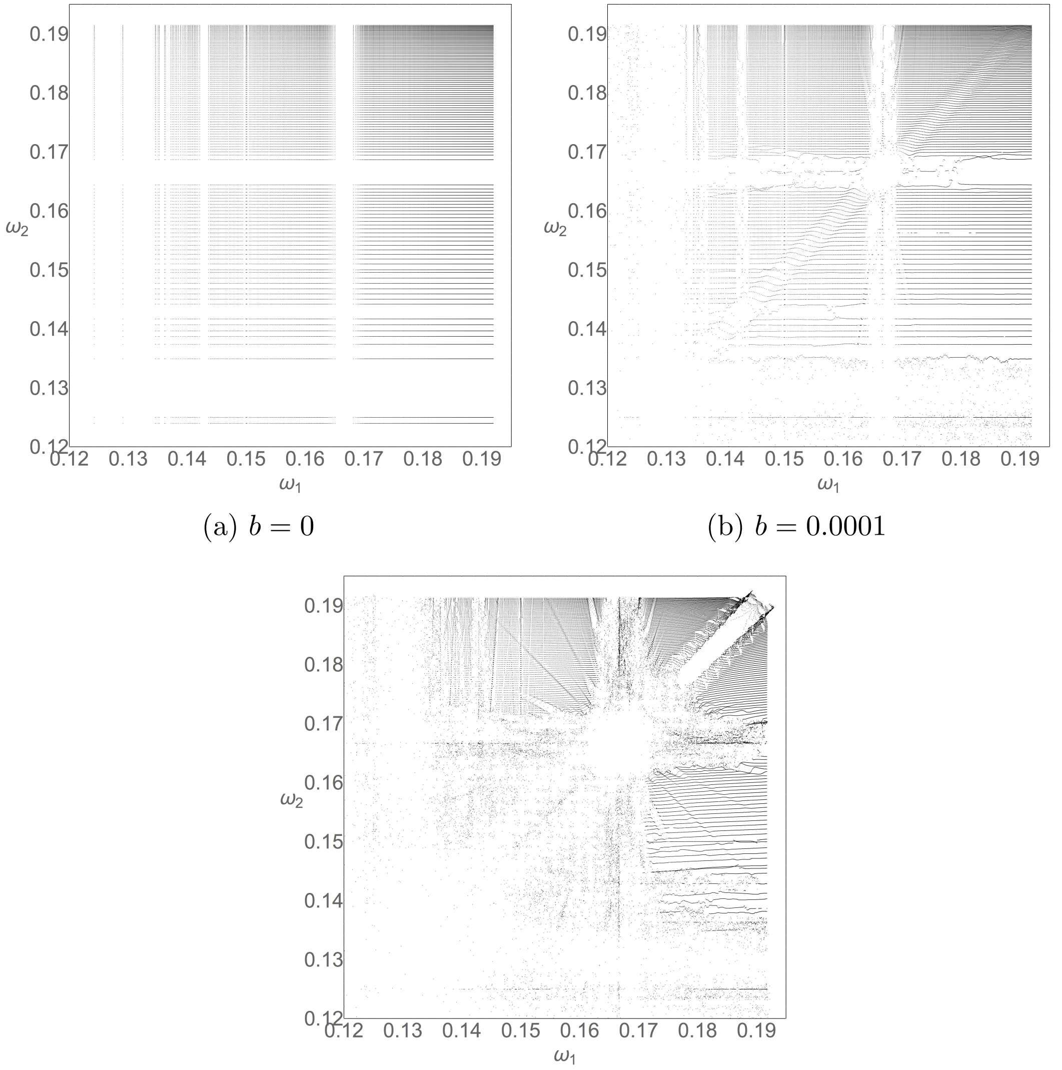

(a) $b = 0$

(b) $b = 0.0001$

(c) $b = 0.01$

Figure 4.2: Frequency maps of the Froeschlé mapping. Compare to [76]. As a demonstration of the frequency method, we generate the frequency map for the mapping of Eq. (1.46) around the 1/6 resonance for various values of the coupling parameter b.

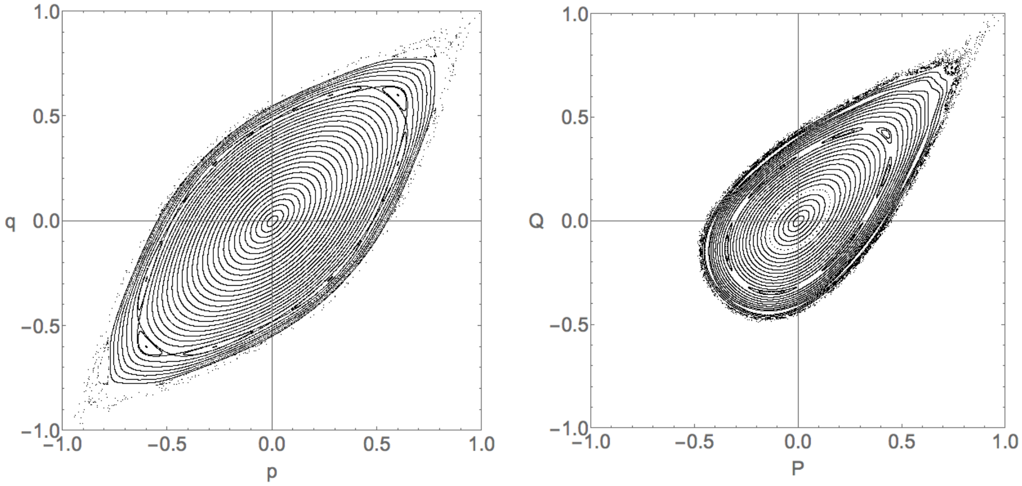

Figure 4.3: Phase portraits of the uncoupled cubic-quadratic mapping (Form$_2$, $t = \tau = 1.1$).

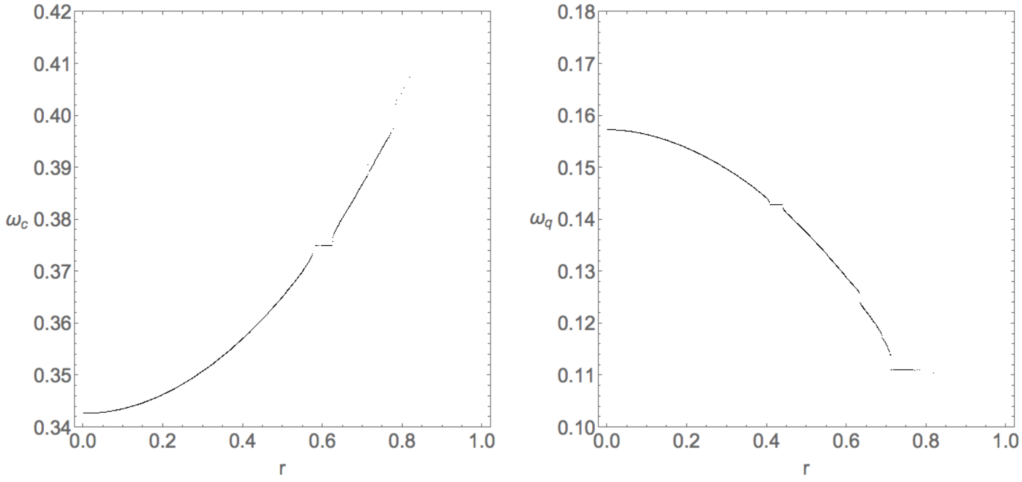

Figure 4.4: Frequencies of the uncoupled cubic-quadratic mapping (Form$_2$, $t = \tau = 1.1, a = .1$).

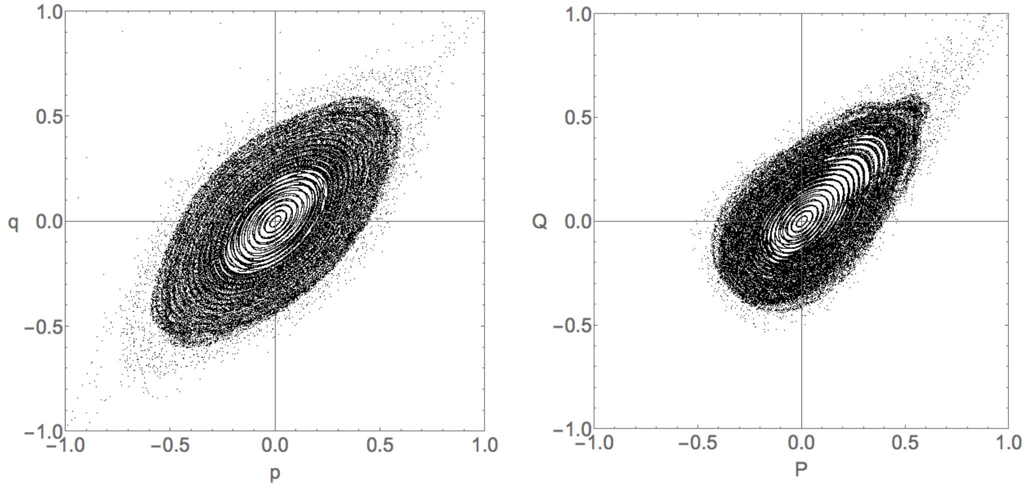

Figure 4.5: Phase portraits of the coupled cubic-quadratic mapping (Form$_2$, $t = \tau = 1.1, a = .1$).

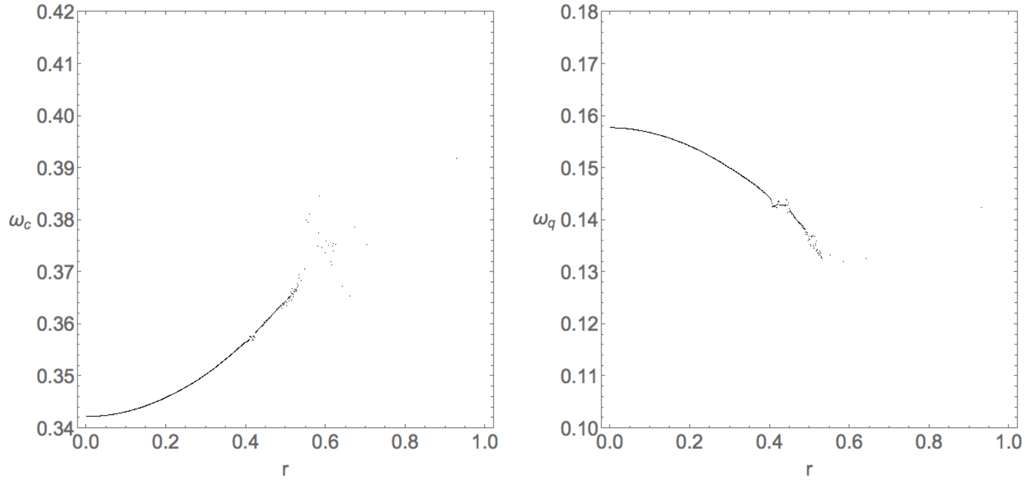

Figure 4.6: Frequencies of the coupled cubic-quadratic mapping (Form$_2$, $t = \tau = 1.1, a = .1$).

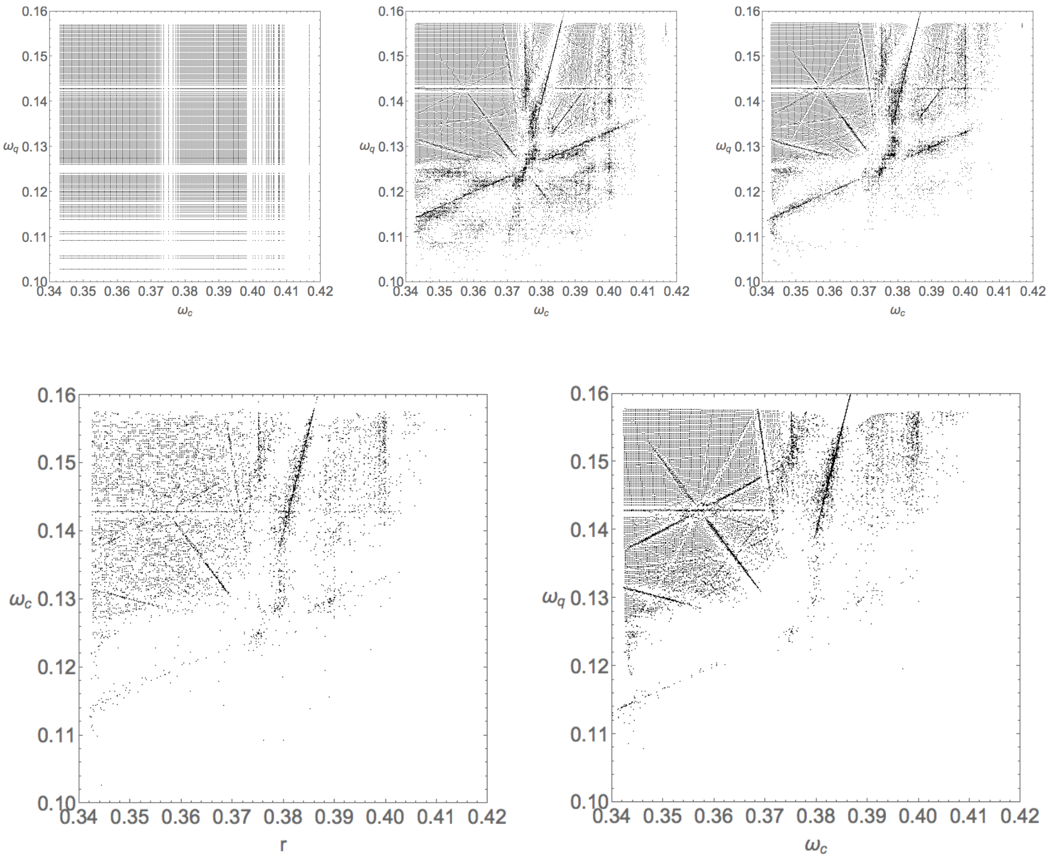

Figure 4.7: The frequency map for various a values. Frequency maps for $a = 0$ (top left), 0.025 (top middle), 0.05 (top right), 0.075 (bottom left), and 0.1 (bottom right). Note the appearance of the resonance near (.38, .16).

around tori by investigating the escape times of the mapping and the long-term stability of orbits.

4.4.1 Example I

We iterate the initial condition $(.623, .6253, 0.0, 0.0)$ for $a = 0.01$, $t = 1.1$, $\tau = 1.1$ using Form_1 of the mapping. See Figures 4.8–4.10. In Figure 4.8, we plot three snapshots consisting of 2^{16} iterations each in the respective sub-planes for an orbit that escapes after approximately 10^6 iterations. Note the difference in the orbit in each successive row. With these parameters, escape can occur quickly (Chap. 6). Figure 4.9 shows an alternative, closer view of the last 2^{16} before escape, as in the bottom row of Figure 4.8. Looking closely, one can see the points of the orbit diverge in the bottom pane of Figure 4.8 and in Figure 4.9. To demonstrate evidence of diffusion in frequency space, we analyze the frequencies of the orbit (Figure 4.10).

For comparison, we analyze the cubic and quadratic frequencies of the coupled map (Figure 4.10) and the uncoupled maps. Figures 4.11 and 4.12, respectively, show the uncoupled quadratic and cubic frequencies in chunks of 2^9 and 2^{10} for an orbit of total length 2^{19}. We observe numerical artifacts in the short time ($n = 2^9$) frequency analysis of the uncoupled quadratic. However, note the regularity of this uncoupled frequency (Figure 4.11) relative to the frequency of the coupled orbit analyzed in the same manner (Figure 4.10, top). It appears that the artifact is due mainly to the small amplitude of the quadratic, as we observe nothing similar in the $n = 2^9$

uncoupled cubic frequency analysis. At approximately $T = 10^6$ (Figure 4.8, bottom; Figure 4.9) the orbit suddenly increases in amplitude in a short number of iterations and becomes unbounded. This transition takes place too quickly to be observed in the frequency space (Figure 4.10), but we observe the transition in phase space (Figure 4.8, 4.9). Next we introduce two examples with longer exits that may be observed in frequency space.

4.4.2 Example II

We iterate the initial condition $(.69, .7, 0.0, 0.0)$ for $a = 0.1$, $t = \tau = 1.1$ using Form_2 of the mapping and plot the frequencies of the orbit in Figure 4.13. The frequencies diffuse near the initial value, suggesting the existence of a torus. Suddenly, the orbit jumps to a new frequency in the quadratic, and eventually escapes after approximately 10^8 iterations.

From the frequency analysis of the trajectory we note three types of orbits; nearly regular, chaotic, and a transitory orbit that "flips" between two frequencies. To investigate further, we record and plot the (p, q, P, Q) coordinates in their respective sub-planes for 10^5 iterations corresponding to qualitatively different regions of Figure 4.8. The $p_i - q_i$ projections are shown in Figure 4.15. In frequency space, the orbit diffuses along a resonance, where nearby exist stable orbits, before jumping to a new resonance (Figures 4.14 and 4.17) and exiting, suggesting the existence of Arnol'd Diffusion.

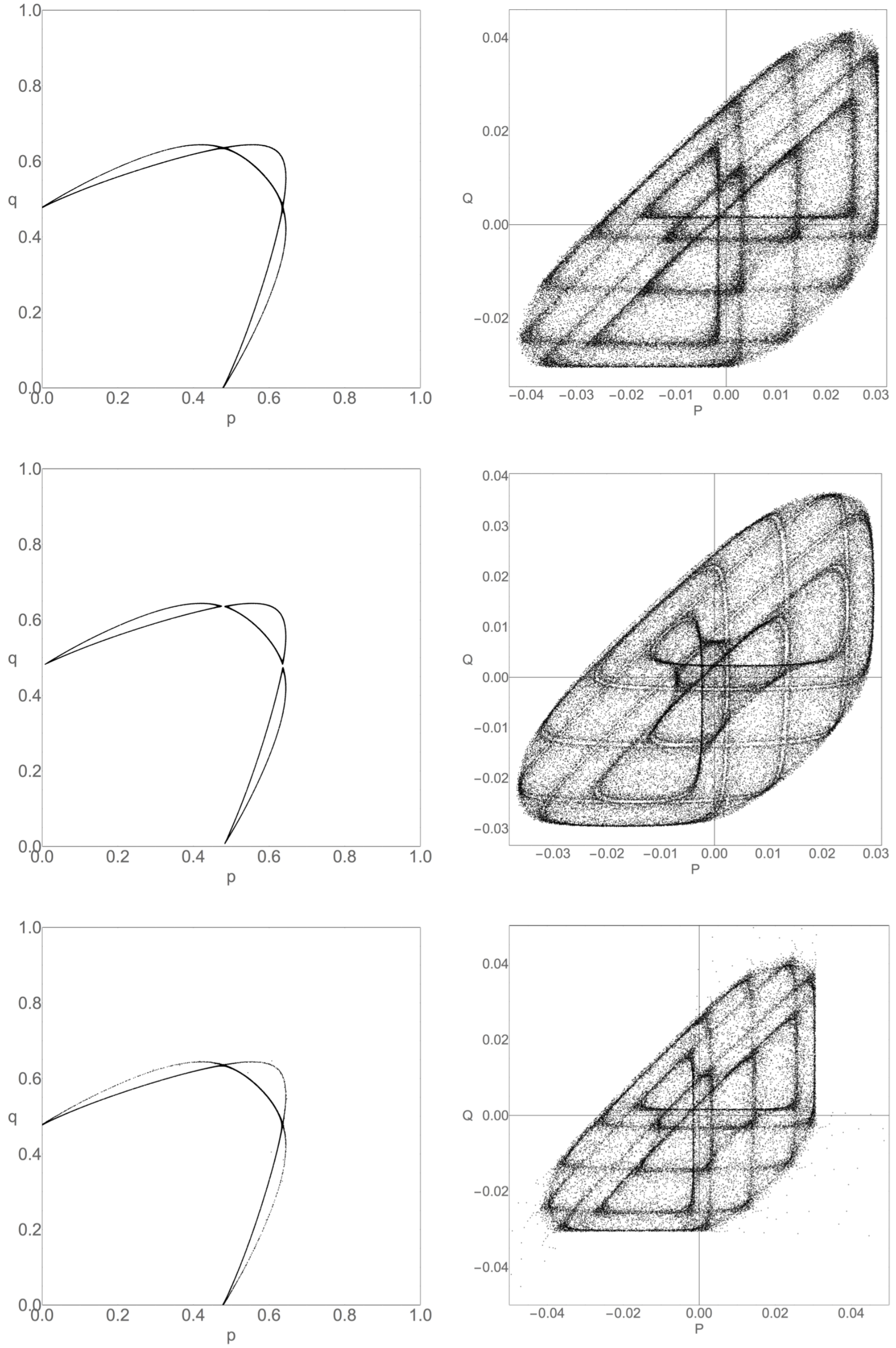

Figure 4.8: Escape orbit for Form_1 of the coupled map (I). ICs $(.623, .6253, 0, 0)$, Form_1 of the map. With these parameters, escape (bottom row) occurs quickly (also see Chap. 6).

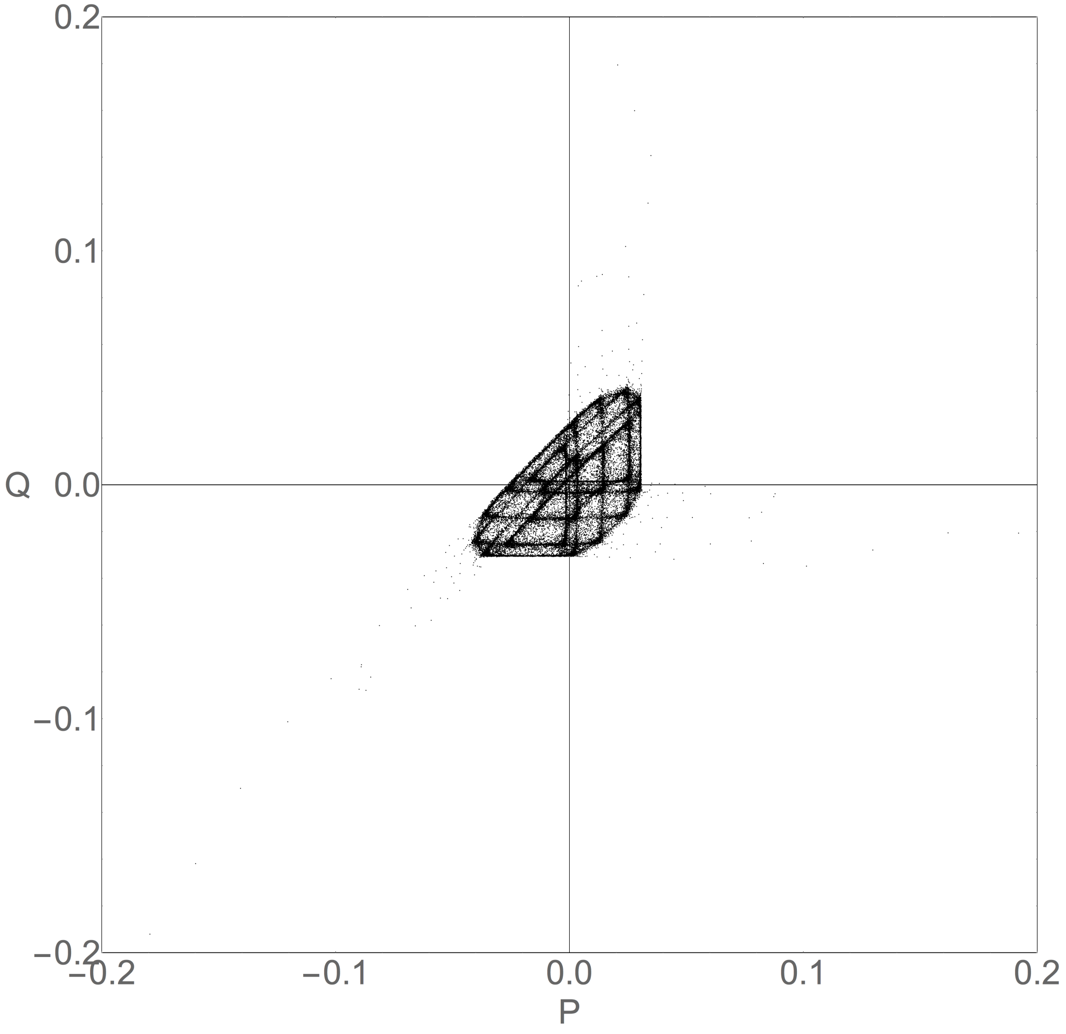

Figure 4.9: Escape orbit for Form_1 of the coupled map (II). ICs $(.623, .6253, 0, 0)$, Form_1 of the map. With these parameters, escape occurs quickly.

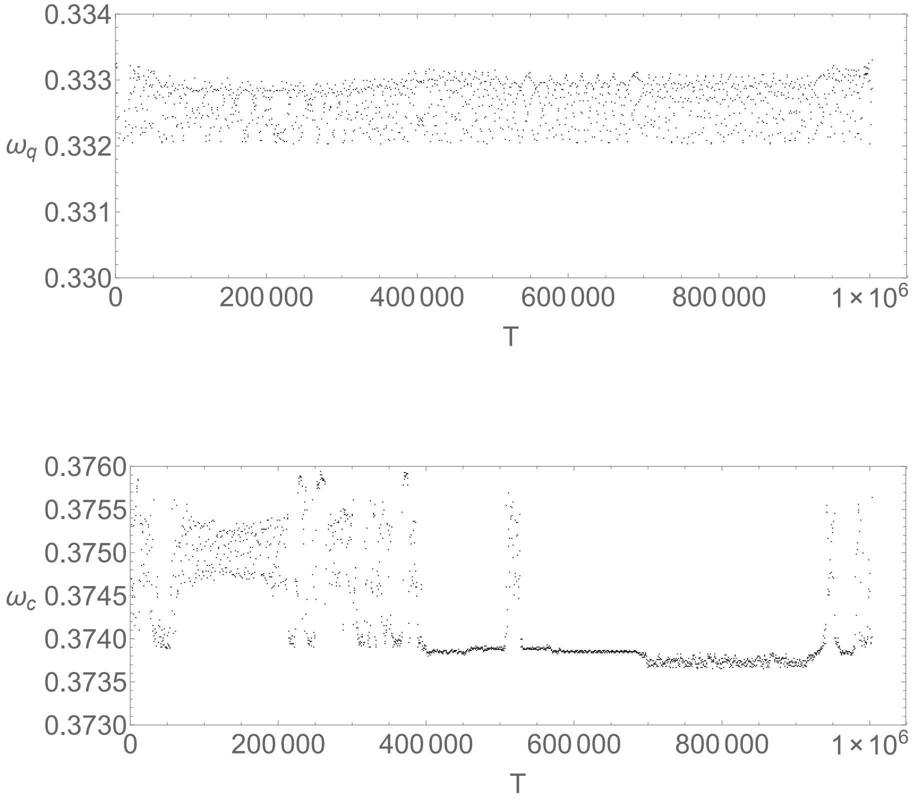

Figure 4.10: Frequencies of the coupled mapping, Example I. Frequencies corresponding to ICs $(.623, .6253, 0, 0)$, Form$_1$ of the map (orbits shown in Figure 4.7, this section).

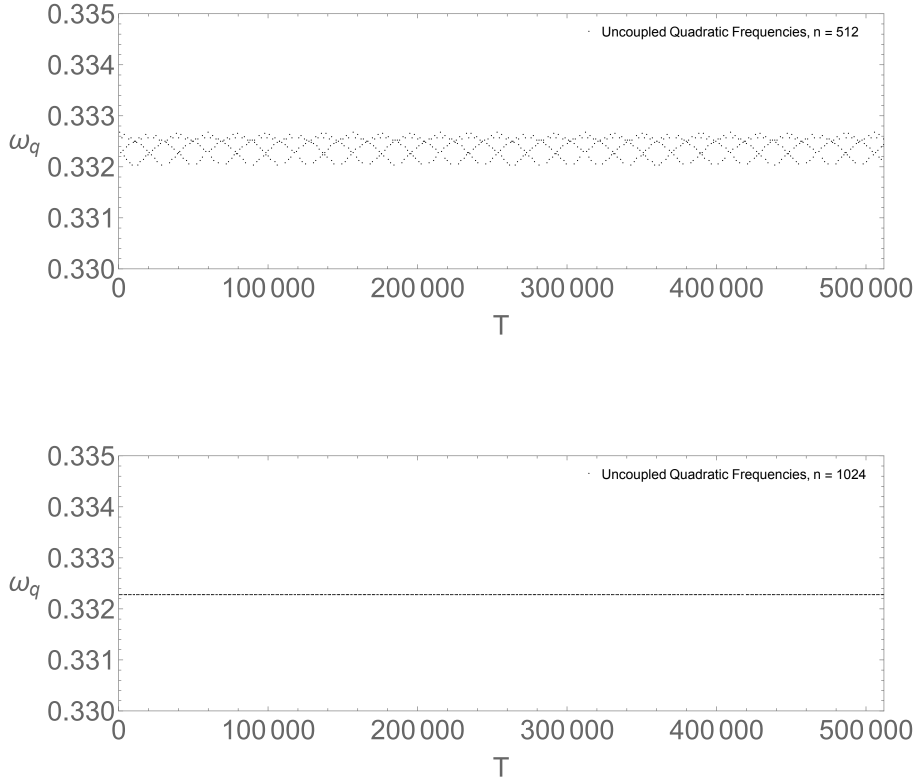

Figure 4.11: Frequency analysis of the uncoupled quadratic map, $n = 2^9, 2^{10}$. Frequencies of an orbit of the uncoupled quadratic mapping, analyzed in chunks of $n = 2^9, 2^{10}$. Note the disappearance of the numerical artifact when using 1024 data points.

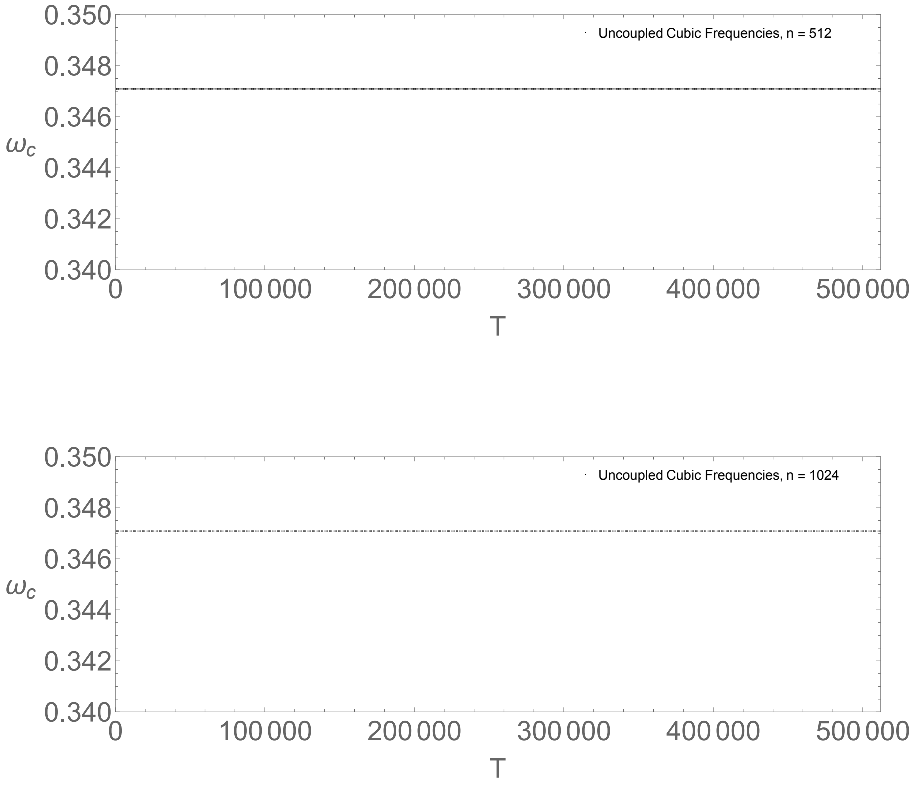

Figure 4.12: Frequency analysis of the uncoupled cubic map, $n = 2^9, 2^{10}$ Frequencies of an orbit of the uncoupled quadratic mapping, analyzed in chunks of $n = 2^9, 2^{10}$. Note that, for the much larger in scale orbit of the cubic contribution to the mapping, there is little uncertainty in the frequency even for $n = 512$.

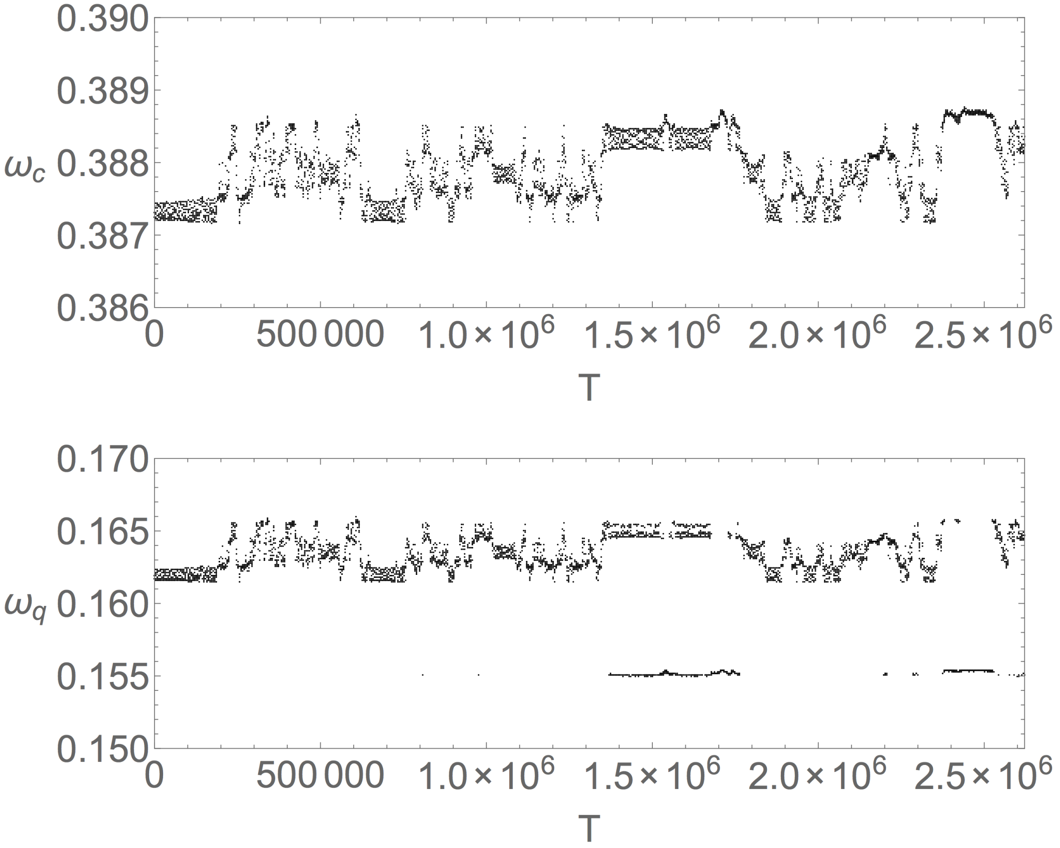

Figure 4.13: Diffusion along resonances (I). initial condition $(.69, .7, 0.0, 0.0)$. (Form_2, $t = \tau = 1.1$). Diffusion in the frequency space reveals three distinct regions.

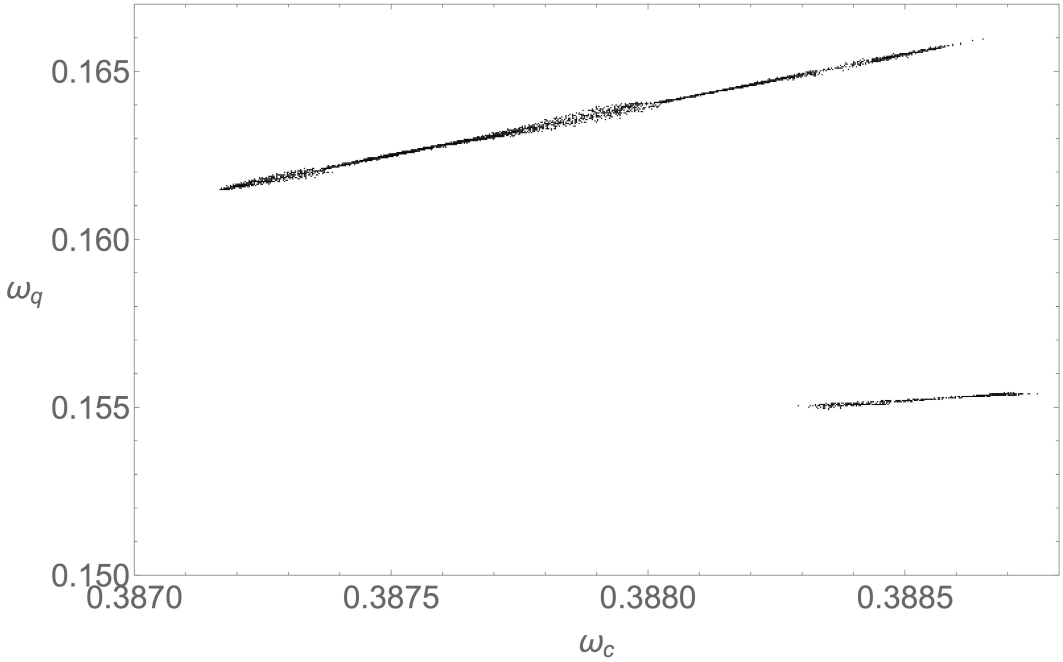

Figure 4.14: Diffusion along resonances (II). initial condition $(.69, .7, 0.0, 0.0)$, (Form$_2$, $t = \tau = 1.1$). The trajectory diffuses along the primary resonance for approximately 10^6, then suddenly jumps to a new resonance (cf. Figure 4.12).

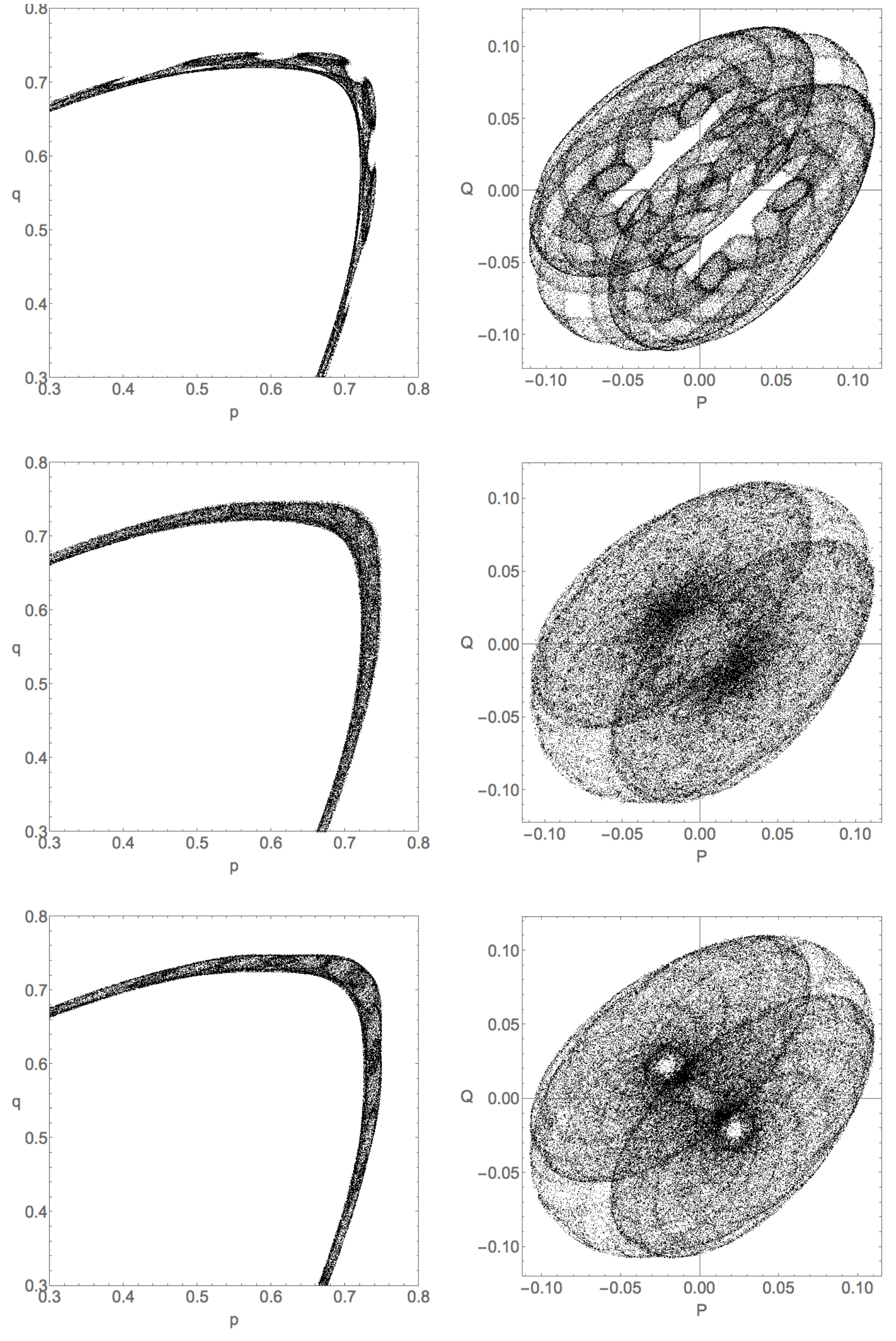

Figure 4.15: Diffusion along resonances: orbits. Sub-plane projections corresponding to three qualitatively different regions of Figure 4.13. We characterize three types of orbits that are described by their behavior in the frequency space: nearly regular, chaotic, and transitory. See text for further description. The initial condition is $(.69, .7, 0.0, 0.0)$, (Form$_2$, $t = \tau = 1.1$).

```
0.3873820792953745461    0.1621462378861236383        0.3873871266684237957    0.1621613800052715139
0.3873820792953745462    0.1621462378861236385        0.3873871266684238798    0.1621613800052716129
0.3873820792953745462    0.1621462378861236385        0.3873871266684238395    0.1621613800052714519
0.3873825894552893133    0.1621477683658679395        0.3873876530904673998    0.1621629592714017973
0.3873825894552885895    0.1621477683658657760        0.3873876530904644513    0.1621629592713924111
0.3873825894552890632    0.1621477683658672753        0.3873876530904642882    0.1621629592713916759
0.3873830981139022707    0.1621492943417068081        0.3873881535506188188    0.1621644606518555082
0.3873830981139021802    0.1621492943417066387        0.3873881535506182226    0.1621644606518557100
0.3873830981139021287    0.1621492943417064823        0.3873881535506177650    0.1621644606518536318
0.3873836056003951729    0.1621508168011855101        0.3873886502275230103    0.1621659506825690308
0.3873836056003950073    0.1621508168011851084        0.3873886502275230102    0.1621659506825690307
0.3873836056003948193    0.1621508168011845977        0.3873886502275230103    0.1621659506825690308
0.3873841122954118389    0.1621523368862355168        0.3873891501448784044    0.1621674504346352133
0.3873841122954118389    0.1621523368862355168        0.3873891501448784044    0.1621674504346352133
0.3873841122954118389    0.1621523368862355168        0.3873891501448784044    0.1621674504346352133
0.3873846180811683463    0.1621538542435050390        0.3873896502616218875    0.1621689507848656625
0.3873846180811683463    0.1621538542435050390        0.3873896502616218874    0.1621689507848656624
0.3873846180811683463    0.1621538542435050390        0.3873896502616218874    0.1621689507848656623
0.3873851230685039094    0.1621553692055119105        0.3873901502091302945    0.1621704506273908833
0.3873851230685043530    0.1621553692055136252        0.3873901502091302944    0.1621704506273908833
0.3873851230685043222    0.1621553692055136497        0.3873901502091302945    0.1621704506273908834
0.3873856272674152057    0.1621568818022456170        0.3873906498811384840    0.1621719496434154520
0.3873856272674152057    0.1621568818022456170        0.3873906498811384839    0.1621719496434154516
0.3873856272674152057    0.1621568818022456170        0.3873906498811384838    0.1621719496434154514
0.3873861305168519061    0.1621583915505557174        0.3873911492408558371    0.1621734477225675116
0.3873861305168519057    0.1621583915505557176        0.3873911492408558371    0.1621734477225675107
0.3873861305168519061    0.1621583915505557181        0.3873911492408558369    0.1621734477225675106
0.3873866321489164736    0.1621598964467494103        0.3873916482761501892    0.1621749448284505669
0.3873866321489164691    0.1621598964467493269        0.3873916482761501881    0.1621749448284505641
0.3873866321489164624    0.1621598964467495048        0.3873916482761501876    0.1621749448284505638
```

Figure 4.16: Frequency scan near the irregular orbit. For a series of initial conditions near $(.69, .7, 0.0, 0.0)$ (Form$_2$, $t = \tau = 1.1$) we obtain the frequency of three consecutive chunks of 2^{20} iterations. We note the existence of several orbits with constant frequencies, suggestive of tori.

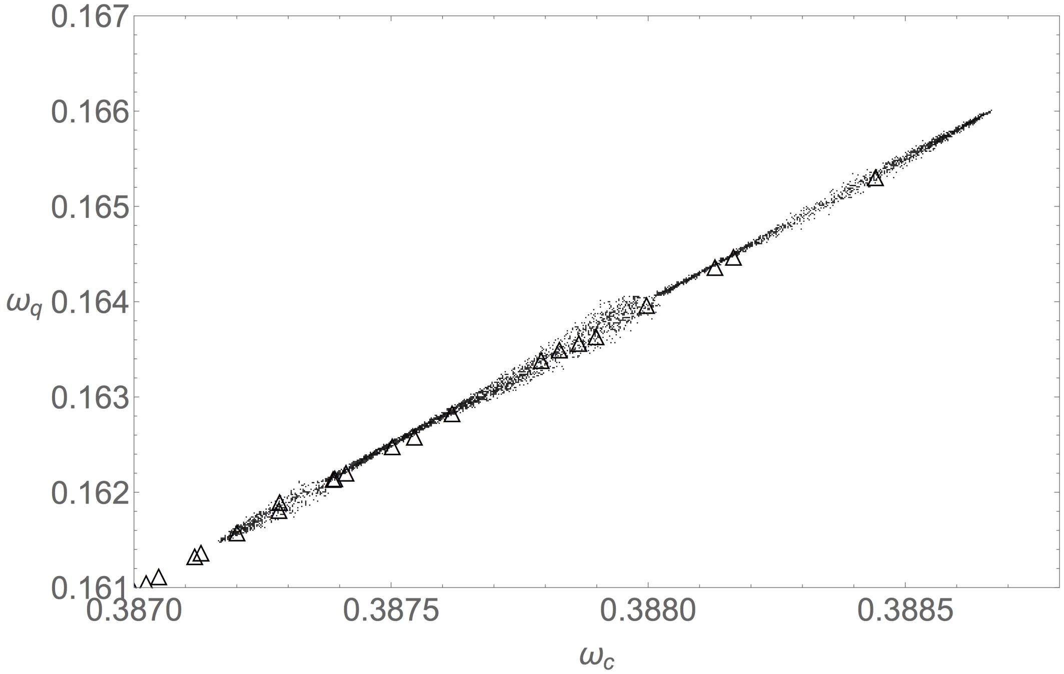

Figure 4.17: Resonance frequencies with tori. We plot the frequencies from an irregular orbit with possible tori (Δ) obtained from the frequency map analysis.

```
0.1576284254263390570    0.1576269363708741672    0.1576254367565704311    0.1576239078887933632    0.1576223888405986428
0.1576284254263390570    0.1576269363708741658    0.1576254367565703269    0.1576239078887933719    0.1576223888405986428
0.1576284254263390570    0.1576269363708741669    0.1576254367565704843    0.1576239078887933676    0.1576223888405986428
0.1576283512532998821    0.1576268616179074710    0.1576253616289585036    0.1576238332180744527    0.1576223122553486946
0.1576283512532998821    0.1576268616179074715    0.1576253616289585028    0.1576238332180746986    0.1576223122553486946
0.1576283512532998821    0.1576268616179074723    0.1576253616289585029    0.1576238332180744554    0.1576223122553486946
0.1576282770505225283    0.1576267868365937299    0.1576252865151310378    0.1576237582075701195    0.1576222356322781332
0.1576282770505225282    0.1576267868365937300    0.1576252865151310378    0.1576237582075701197    0.1576222356322781332
0.1576282770505225283    0.1576267868365937300    0.1576252865151310378    0.1576237582075701198    0.1576222356322781332
0.1576282028180417310    0.1576267120276481047    0.1576252114259532568    0.1576236829458893948    0.1576221589720670467
0.1576282028180417310    0.1576267120276481048    0.1576252114259532567    0.1576236829458893950    0.1576221589720670466
0.1576282028180417310    0.1576267120276481047    0.1576252114259532568    0.1576236829458893949    0.1576221589720670467
0.1576281285558962104    0.1576266371915562900    0.1576251363757604873    0.1576236074923128642    0.1576220822753092871
0.1576281285558962104    0.1576266371915562900    0.1576251363757604873    0.1576236074923066427    0.1576220822753092868
0.1576281285558962104    0.1576266371915562900    0.1576251363757604872    0.1576236074923115085    0.1576220822753092884
0.1576280542641291552    0.1576265623287632668    0.1576250613841002998    0.1576235318868136488    0.1576220055425271735
0.1576280542641291552    0.1576265623287632668    0.1576250613841002997    0.1576235318868136488    0.1576220055425271734
0.1576280542641291552    0.1576265623287632668    0.1576250613841002997    0.1576235318868136488    0.1576220055425271734
0.1576279799427888339    0.1576264874397325028    0.1576249864781785538    0.1576234561581610598    0.1576219287741834636
0.1576279799427888339    0.1576264874397325028    0.1576249864781784802    0.1576234561581610598    0.1576219287741834636
0.1576279799427888339    0.1576264874397325028    0.1576249864781783953    0.1576234561581610598    0.1576219287741834636
0.1576279055919293749    0.1576264125249738206    0.1576249116967444616    0.1576233803263520317    0.1576218519706914443
0.1576279055919293749    0.1576264125249738206    0.1576249116967444611    0.1576233803263520317    0.1576218519706914443
0.1576279055919293749    0.1576264125249738206    0.1576249116967444613    0.1576233803263520318    0.1576218519706914443
0.1576278312116118079    0.1576263375850626396    0.1576248370962594235    0.1576233044061804413    0.1576217751324234636
0.1576278312116118079    0.1576263375850626396    0.1576248370962594227    0.1576233044061804413    0.1576217751324234636
0.1576278312116118079    0.1576263375850626396    0.1576248370962594215    0.1576233044061804413    0.1576217751324234636
0.1576277568019055357    0.1576262626206577266    0.1576247627607648919    0.1576232284086276295    0.1576216982597182702
0.1576277568019055356    0.1576262626206577266    0.1576247627607648900    0.1576232284086276293    0.1576216982597182702
0.1576277568019055356    0.1576262626206577266    0.1576247627607648871    0.1576232284086276294    0.1576216982597182702
0.1576276823628905799    0.1576261876325204983    0.1576246888166949129    0.1576231523418226187    0.1576216213528874506
0.1576276823628905799    0.1576261876325204983    0.1576246888166948929    0.1576231523418226163    0.1576216213528874505
0.1576276823628905799    0.1576261876325204983    0.1576246888166948940    0.1576231523418226178    0.1576216213528874506
0.1576276078946613484    0.1576261126215377578    0.1576246154501288171    0.1576230762101745742    0.1576215444122211964
0.1576276078946613484    0.1576261126215377578    0.1576246154501287443    0.1576230762101734314    0.1576215444122211964
0.1576276078946613484    0.1576261126215377578    0.1576246154501288080    0.1576230762101748681    0.1576215444122211964
0.1576275333973337103    0.1576260375887495468    0.1576245428991605553    0.1576230000381534070    0.1576214674379936230
0.1576275333973337103    0.1576260375887495468    0.1576245428991604697    0.1576230000382654112    0.1576214674379936229
0.1576275333973337105    0.1576260375887495468    0.1576245428991601755    0.1576230000381604848    0.1576214674379936230
0.1576274588710602247    0.1576259625353840316    0.1576244712599467415    0.1576229237933773448    0.1576213904304678338
0.1576274588710602245    0.1576259625353840316    0.1576244712599457170    0.1576229237933773481    0.1576213904304678338
0.1576274588710602246    0.1576259625353840316    0.1576244712599432334    0.1576229237933773453    0.1576213904304678338
0.1576273843160683982    0.1576258874629018693    0.1576243989412819695    0.1576228475036244045    0.1576213133899009398
0.1576273843160674921    0.1576258874629018693    0.1576243989412057127    0.1576228475036244045    0.1576213133899009397
0.1576273843160675472    0.1576258874629018693    0.1576243989413049387    0.1576228475036244045    0.1576213133899009397
0.1576273097327885873    0.1576258123730533524    0.1576242717730357526    0.1576227711671329634    0.1576212363165491883
0.1576273097327885886    0.1576258123730533524    0.1576242717730635197    0.1576227711671329634    0.1576212363165491883
0.1576273097327885915    0.1576258123730533524    0.1576242717731448878    0.1576227711671329634    0.1576212363165491882
0.1576272351224240096    0.1576257372679529057    0.1576241996995650098    0.1576226947856721838    0.1576211592106735242
0.1576272351224240071    0.1576257372679529057    0.1576241996995649871    0.1576226947856721838    0.1576211592106735241
0.1576272351224239779    0.1576257372679529057    0.1576241996995653319    0.1576226947856721838    0.1576211592106735240
0.1576271604937685128    0.1576256621501773783    0.1576241281895806433    0.1576226183609332896    0.1576210820725460318
0.1576271604921835826    0.1576256621501773783    0.1576241281895813748    0.1576226183609332896    0.1576210820725460318
0.1576271604920682447    0.1576256621501773783    0.1576241281895815184    0.1576226183609332896    0.1576210820725460315
0.1576270857608678438    0.1576255870228972961    0.1576240556067124983    0.1576225418943760321    0.1576210049024565665
0.1576270857692524724    0.1576255870228972961    0.1576240556067125533    0.1576225418943760321    0.1576210049024565665
0.1576270857676542103    0.1576255870228972961    0.1576240556067124673    0.1576225418943760321    0.1576210049024565664
0.1576270110935562835    0.1576255118900535599    0.1576239820852037010    0.1576224653872441726    0.1576209277007222972
0.1576270110935571118    0.1576255118900535599    0.1576239820852037251    0.1576224653872441726    0.1576209277007222966
0.1576270110935567182    0.1576255118900535599    0.1576239820852037018    0.1576224653872441726    0.1576209277007222964
```

Figure 4.18: Frequency scan for the coupled mapping (I). To find tori we perform a frequency search near the regular region of the frequency map. Shown are the frequencies obtained from P (cf. Eq. (3.15)).

```
0.3567464248932053765    0.3568908905957549562    0.3570355742761351004    0.3571860108590664934    0.3573305562563379332
0.3567464248932053765    0.3568908905957549551    0.3570355742761346383    0.3571860108590664938    0.3573305562563379332
0.3567464248932053765    0.3568908905957549543    0.3570355742761347592    0.3571860108590664941    0.3573305562563379332
0.3567536340779492394    0.3568981272418268704    0.3570427744920002648    0.3571929297536093580    0.3573378929939023463
0.3567536340779492394    0.3568981272418268735    0.3570427744920002621    0.3571929297536069430    0.3573378929939023463
0.3567536340779492394    0.3568981272418268738    0.3570427744920002578    0.3571929297536088178    0.3573378929939023463
0.3567608448690222910    0.3569053647754180506    0.3570499630750754799    0.3571999413736740175    0.3573452335177710338
0.3567608448690222902    0.3569053647754180513    0.3570499630750754799    0.3571999413736740175    0.3573452335177710337
0.3567608448690222910    0.3569053647754180506    0.3570499630750754799    0.3571999413736740175    0.3573452335177710337
0.3567680572528160592    0.3569126031073632636    0.3570571367940445249    0.3572070197331990067    0.3573525776283562551
0.3567680572528160592    0.3569126031073632650    0.3570571367940445249    0.3572070197331990067    0.3573525776283562551
0.3567680572528160592    0.3569126031073632629    0.3570571367940445249    0.3572070197331990067    0.3573525776283562551
0.3567752712146390022    0.3569198421363602332    0.3570642913273287533    0.3572141474335011879    0.3573599251526514390
0.3567752712146390023    0.3569198421363602332    0.3570642913273287533    0.3572141474335078324    0.3573599251526514337
0.3567752712146390023    0.3569198421363602332    0.3570642913273287533    0.3572141474335018368    0.3573599251526514606
0.3567824867386073360    0.3569270817473843794    0.3570714207822342158    0.3572213125754625081    0.3573672759399659972
0.3567824867386073360    0.3569270817473843794    0.3570714207822342158    0.3572213125754625080    0.3573672759399659972
0.3567824867386073360    0.3569270817473843794    0.3570714207822342158    0.3572213125754625079    0.3573672759399659972
0.3567897038075231715    0.3569343218094595056    0.3570785169490392195    0.3572285068172563446    0.3573746298584529874
0.3567897038075231715    0.3569343218094595056    0.3570785169490386555    0.3572285068172563446    0.3573746298584529874
0.3567897038075231715    0.3569343218094595056    0.3570785169490379493    0.3572285068172563446    0.3573746298584529874
0.3567969224027377502    0.3569415621728721960    0.3570855681221204003    0.3572357241814654869    0.3573819867922632589
0.3567969224027377502    0.3569415621728721960    0.3570855681221204003    0.3572357241814654871    0.3573819867922632589
0.3567969224027377502    0.3569415621728721960    0.3570855681221204002    0.3572357241814654868    0.3573819867922632590
0.3568041425039975078    0.3569488026657457387    0.3570925572084624775    0.3572429602873942052    0.3573893466391980822
0.3568041425039975078    0.3569488026657457387    0.3570925572084624773    0.3572429602873942052    0.3573893466391980822
0.3568041425039975078    0.3569488026657457387    0.3570925572084624775    0.3572429602873942052    0.3573893466391980822
0.3568113640892706467    0.3569560430898218558    0.3570994586987709591    0.3572502118618704722    0.3573967093087619389
0.3568113640892706467    0.3569560430898218558    0.3570994586987709587    0.3572502118618704722    0.3573967093087619389
0.3568113640892706467    0.3569560430898218558    0.3570994586987709593    0.3572502118618704722    0.3573967093087619389
0.3568185871345516794    0.3569632832152389450    0.3571062340497850265    0.3572574764160233796    0.3574040747205376974
0.3568185871345516794    0.3569632832152389450    0.3571062340497849543    0.3572574764160233780    0.3574040747205376974
0.3568185871345516794    0.3569632832152389450    0.3571062340497849160    0.3572574764160233801    0.3574040747205376973
0.3568258116136416004    0.3569705227740228197    0.3571128260878580892    0.3572647520334995421    0.3574114428028240052
0.3568258116136416004    0.3569705227740228197    0.3571128260878580994    0.3572647520335007151    0.3574114428028240052
0.3568258116136416004    0.3569705227740228197    0.3571128260878580859    0.3572647520335011018    0.3574114428028240052
0.3568330374979027096    0.3569777614519084232    0.3571191601880122326    0.3572720371280103192    0.3574188134914865302
0.3568330374979027093    0.3569777614519084232    0.3571191601880122329    0.3572720371280703590    0.3574188134914865302
0.3568330374979027086    0.3569777614519084232    0.3571191601880122333    0.3572720371281379935    0.3574188134914865302
0.3568402647559919943    0.3569849988779757876    0.3571251992481033149    0.3572793306456936240    0.3574261867289848826
0.3568402647559919942    0.3569849988779757876    0.3571251992481033236    0.3572793306456936266    0.3574261867289848826
0.3568402647559919942    0.3569849988779757876    0.3571251992481033104    0.3572793306456936206    0.3574261867289848826
0.3568474933535551449    0.3569922346113934984    0.3571313938470501532    0.3572866315242978477    0.3574335624635445109
0.3568474933534984092    0.3569922346113934984    0.3571313938470501624    0.3572866315242978477    0.3574335624635445109
0.3568474933535019093    0.3569922346113934983    0.3571313938470501418    0.3572866315242978477    0.3574335624635445109
0.3568547232532760786    0.3569994681242913137    0.3571540071500970082    0.3572939389982428195    0.3574409406484482460
0.3568547232532760629    0.3569994681242913137    0.3571540071500968048    0.3572939389982428195    0.3574409406484482460
0.3568547232532760607    0.3569994681242913137    0.3571540071500972154    0.3572939389982428196    0.3574409406484482460
0.3568619544151148399    0.3570066987793903310    0.3571602599365223132    0.3573012524262172572    0.3574483212414299999
0.3568619544151148488    0.3570066987793903310    0.3571602599365223132    0.3573012524262172572    0.3574483212414299994
0.3568619544151148374    0.3570066987793903310    0.3571602599365223130    0.3573012524262172572    0.3574483212414299993
0.3568691868099689688    0.3570139258004411414    0.3571662953908482383    0.3573085712763213057    0.3574557042041382923
0.3568691868047818571    0.3570139258004411414    0.3571662953908491064    0.3573085712763213057    0.3574557042041382923
0.3568691868056720203    0.3570139258004411414    0.3571662953908481266    0.3573085712763213057    0.3574557042041382924
0.3568764202169887242    0.3570211482326569531    0.3571726271579654821    0.3573158951043279243    0.3574630895017084054
0.3568764202302474703    0.3570211482326569531    0.3571726271579654821    0.3573158951043279243    0.3574630895017084054
0.3568764202237645302    0.3570211482326569531    0.3571726271579654821    0.3573158951043279243    0.3574630895017084054
0.3568836549139714838    0.3570283648890145809    0.3571792239572601880    0.3573232235365215821    0.3574704771023316391
0.3568836549139726616    0.3570283648890145809    0.3571792239572601895    0.3573232235365215821    0.3574704771023316392
0.3568836549139729324    0.3570283648890145809    0.3571792239572601884    0.3573232235365215821    0.3574704771023316392
```

Figure 4.19: Frequency scan for the coupled mapping (II). To find tori we perform a frequency search near the regular region of the frequency map. Shown are the frequencies obtained from p (cf. Eq. (3.15)).

```
0.3567969224027377502      0.3567969224027377502      0.3567969224027377502
0.3567969224027377502      0.3567969224027377502      0.3567969224027377502
0.3567969224027377502      0.3567969224027377502      0.3567969224027377502
0.3567969224027377502      0.3567969224027377502      0.3567969224027377502
0.3567969224027377502      0.3567969224027377502      0.3567969224027377502
0.3567969224027377502      0.3567969224027377502      0.3567969224027377502
0.3567969224027377502      0.3567969224027377502      0.3567969224027377502
0.3567969224027377502      0.3567969224027377502      0.3567969224027377502
0.3567969224027377502      0.3567969224027377502      0.3567969224027377502
0.3567969224027377502      0.3567969224027377502      0.3567969224027377502
0.3567969224027377502      0.3567969224027377502      0.3567969224027377502
0.3567969224027377502      0.3567969224027377502      0.3567969224027377502
0.3567969224027377502      0.3567969224027377502      0.3567969224027377502
0.3567969224027377502      0.3567969224027377502      0.3567969224027377502
0.3567969224027377502      0.3567969224027377502      0.3567969224027377502
0.3567969224027377502      0.3567969224027377502      0.3567969224027377502
0.3567969224027377502      0.3567969224027377502      0.3567969224027377502
0.3567969224027377502      0.3567969224027377502      0.3567969224027377502
0.3567969224027377502      0.3567969224027377502      0.3567969224027377502
0.3567969224027377502      0.3567969224027377502      0.3567969224027377502
0.3567969224027377502      0.3567969224027377502      0.3567969224027377502
0.3567969224027377502      0.3567969224027377502      0.3567969224027377502
0.3567969224027377502      0.3567969224027377502      0.3567969224027377502
0.3567969224027377502      0.3567969224027377502      0.3567969224027377502
0.3567969224027377502      0.3567969224027377502      0.3567969224027377502
0.3567969224027377502      0.3567969224027377502      0.3567969224027377502
0.3567969224027377502      0.3567969224027377502      0.3567969224027377502
0.3567969224027377502      0.3567969224027377502      0.3567969224027377502
0.3567969224027377502      0.3567969224027377502      0.3567969224027377502
0.3567969224027377502      0.3567969224027377502      0.3567969224027377502
0.3567969224027377502      0.3567969224027377502      0.3567969224027377502
0.3567969224027377502      0.3567969224027377502      0.3567969224027377502
0.3567969224027377502      0.3567969224027377502      0.3567969224027377502
```

Figure 4.20: Frequency analysis of a possible torus (I). Frequency analysis (of the first 100 x 10^7 x 2^{20} iterations) for one of the initial conditions above. We iterate the map for 10^7, then obtain the frequency of the next 2^{20} iterations, and repeat 100 times for an orbit length of approximately 10^{10}.

```
0.1576279055919293749      0.1576279055919293749      0.1576279055919293749
0.1576279055919293749      0.1576279055919293749      0.1576279055919293749
0.1576279055919293749      0.1576279055919293749      0.1576279055919293749
0.1576279055919293749      0.1576279055919293749      0.1576279055919293749
0.1576279055919293749      0.1576279055919293749      0.1576279055919293749
0.1576279055919293749      0.1576279055919293749      0.1576279055919293749
0.1576279055919293749      0.1576279055919293749      0.1576279055919293749
0.1576279055919293749      0.1576279055919293749      0.1576279055919293749
0.1576279055919293749      0.1576279055919293749      0.1576279055919293749
0.1576279055919293749      0.1576279055919293749      0.1576279055919293749
0.1576279055919293749      0.1576279055919293749      0.1576279055919293749
0.1576279055919293749      0.1576279055919293749      0.1576279055919293749
0.1576279055919293749      0.1576279055919293749      0.1576279055919293749
0.1576279055919293749      0.1576279055919293749      0.1576279055919293749
0.1576279055919293749      0.1576279055919293749      0.1576279055919293749
0.1576279055919293749      0.1576279055919293749      0.1576279055919293749
0.1576279055919293749      0.1576279055919293749      0.1576279055919293749
0.1576279055919293749      0.1576279055919293749      0.1576279055919293749
0.1576279055919293749      0.1576279055919293749      0.1576279055919293749
0.1576279055919293749      0.1576279055919293749      0.1576279055919293749
0.1576279055919293749      0.1576279055919293749      0.1576279055919293749
0.1576279055919293749      0.1576279055919293749      0.1576279055919293749
0.1576279055919293749      0.1576279055919293749      0.1576279055919293749
0.1576279055919293749      0.1576279055919293749      0.1576279055919293749
0.1576279055919293749      0.1576279055919293749      0.1576279055919293749
0.1576279055919293749      0.1576279055919293749      0.1576279055919293749
0.1576279055919293749      0.1576279055919293749      0.1576279055919293749
0.1576279055919293749      0.1576279055919293749      0.1576279055919293749
0.1576279055919293749      0.1576279055919293749      0.1576279055919293749
0.1576279055919293749      0.1576279055919293749      0.1576279055919293749
0.1576279055919293749      0.1576279055919293749      0.1576279055919293749
0.1576279055919293749      0.1576279055919293749      0.1576279055919293749
0.1576279055919293749      0.1576279055919293749      0.1576279055919293749
0.1576279055919293749      0.1576279055919293749      0.1576279055919293749
```

Figure 4.21: Frequency analysis of a possible torus. Frequency analysis (of the first 100 x 10^7 x 2^{20} iterations) for one of the initial conditions above. We iterate the map for 10^7, then obtain the frequency of the next 2^{20} iterations, and repeat 100 times for an orbit length of approximately 10^{10}.

4.4.3 Regular Orbits

To search for regular orbits (e.g., Figure 4.22) and provide good evidence of orbits that lie on or near tori, we scan for constant frequencies (Figure 4.16) around the irregular orbits of the previous sections. Figure 4.16 shows a scan of frequencies that were obtained in three consecutive chunks of 2^{20}. A deeper search is illustrated in Figures 4.18 - 4.22. First, we scan in the frequency space to find likely candidates. Then, for a given initial condition, the map is iterated for 10^7, the frequency of the next 2^{20} iterations is obtained, and the procedure is repeated 100 times for an orbit length of approximately 10^{10} (Figures 4.20 and 4.21). In general, we find many such orbits that correspond with the frequency map and escape time analysis (Chap. 6).

4.5 Accuracy and Precision

4.5.1 Shadowing of Orbits

We use the arbitrary precision GNU MPFR library [26] or FORTRAN quadruple (128 bit) precision[1] for accurate computation of the mappings. While the Shadowing Theorem [45, 46] guarantees the existence of true orbits for the dissipative Hénon Map, high-accuracy computations are necessary to avoid small-scale diffusion in the frequency space due to the

---

[1] Through shadowing computations we find that quadruple precision, corresponding to 38-39 decimal places, is usually sufficient to retain over 20 decimal places of accuracy for orbits up to length 10^{12}.

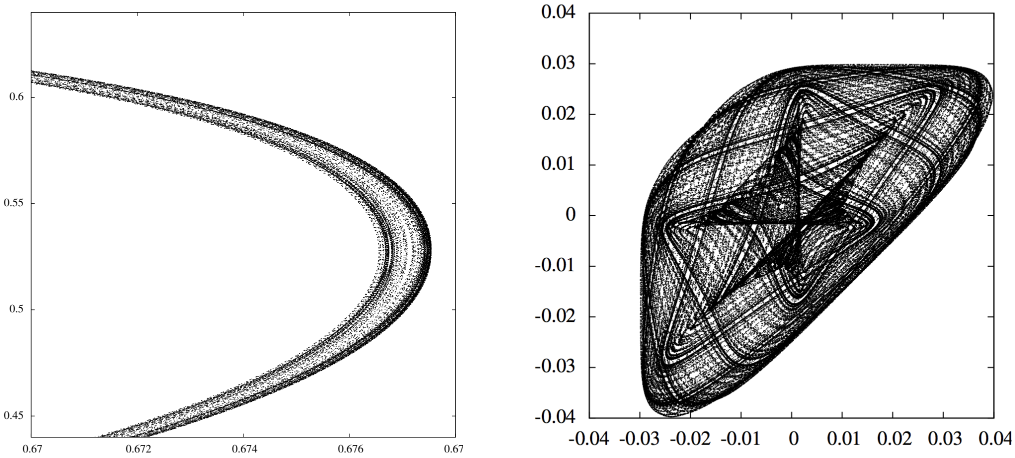

(a) (b)

Figure 4.22: A regular orbit for Form$_1$ of the coupled map. ICs $(.65, .65, 0, 0)$, Form 1 of the map. With these parameters, the orbit remains bounded and well-defined for at least 10^{12} iterations. For regular orbits, we can find constant frequencies (see Figures 4.18 - 4.21).

random error introduced from finite-precision calculations [65] and provide good evidence that our computations successively approximate a true orbit as we increase precision. The accuracy of trajectories is easily determined by a trial and error process in which an initial condition is iterated with increasing precision. In this manner one can obtain the number of iterations before the trajectories differ by some finite amount, and hence a lower bound for accuracy within that specified value. In the language of the Shadowing Theorem, we show that true orbits exist that remain within 10^{-64} of the noisy orbit for 10^{12} iterations. This is proved by observing that for nearby initial conditions ($\delta << 10^{-64}$), the two highest precision computations (of each initial condition) are identical to 64 decimal places after 10^{12} iterations.

Generally speaking, orbits of the mapping that are used to compute frequencies are accurate to 32 or more decimal places, and one hopes for an accuracy of at least $1/T^4$ in the KAM frequencies when T is the time interval of interest [127, 78]. However, the collocation method relies upon the FFTW [27] and LAPACK [3] libraries, which were compiled with long double precision options (80 bits; about 24 decimal places). This represents an improvement of several orders of magnitude over the the precision used in most modern scientific computations; double precision (53 bits, or 15-17 decimal places) binary floating-point specified by the IEEE 754 standard.

The Shadowing Theorem [45, 46] is a proof by construction of the accuracy of computing trajectories. In short, by incrementally increasing the precision of computations and comparing the separation distance between nearby trajectories, it is demonstrated that for an initial amount of noise (or separation) δ_i, we remain within a specified amount of separation δ for an orbit of length N.

The shadowing plots show the dependence of the separation time N on the noise amplitude δ. Hammel, et al. [45] found that $N \sim 1/\sqrt(\delta)$ for the dissipative Hénon mapping. Following a similar procedure, the uncoupled cubic, uncoupled quadratic, and coupled cubic-quadratic mappings were iterated until a separation of $1/\sqrt(\delta)$ occurred. The maximum number of iterations is 10^9, which explains the saturation at higher N of the plot. Saturation occurs at the lower end since we plot anything under 10^3 at that point.

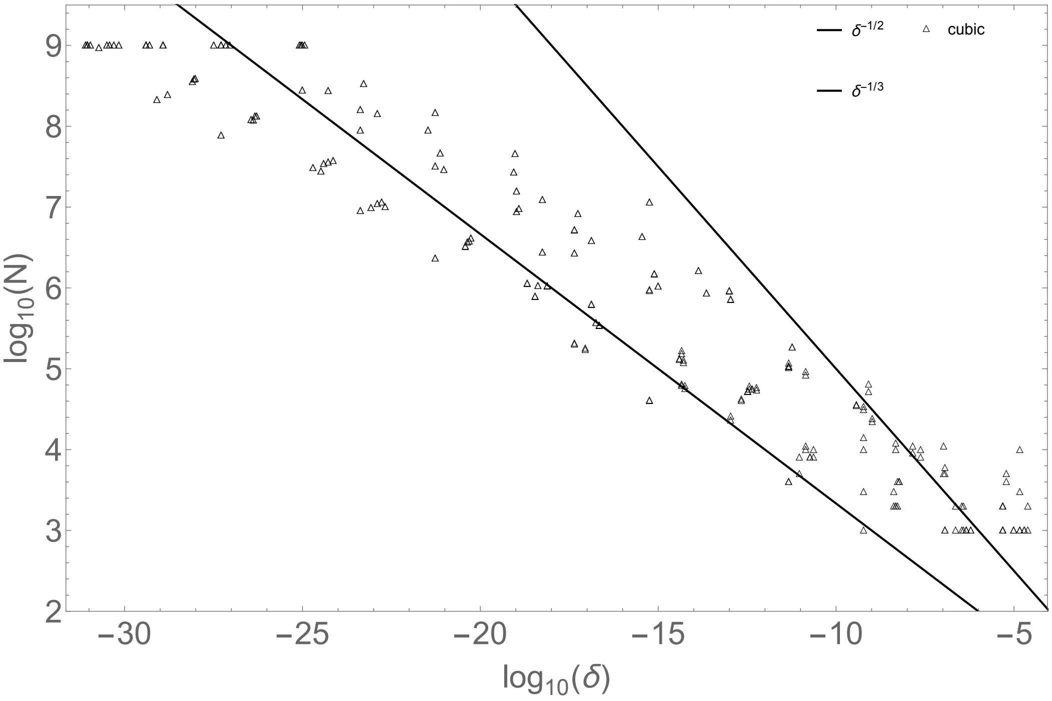

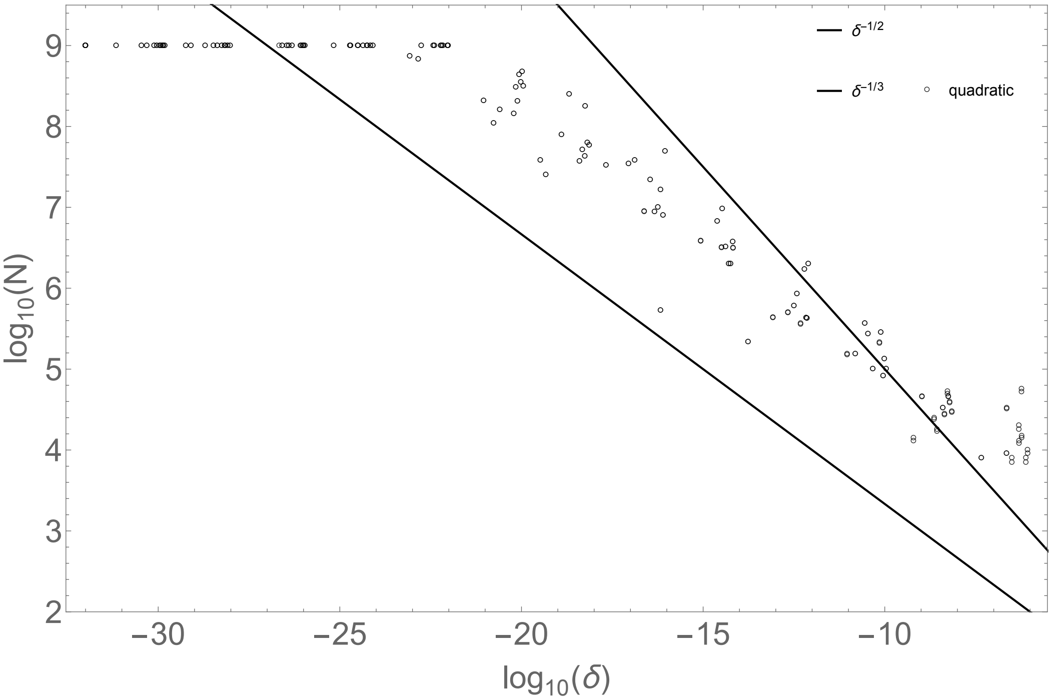

Figure 4.23: Shadowing plots for the uncoupled cubic (top) and quadratic (bottom) mappings.

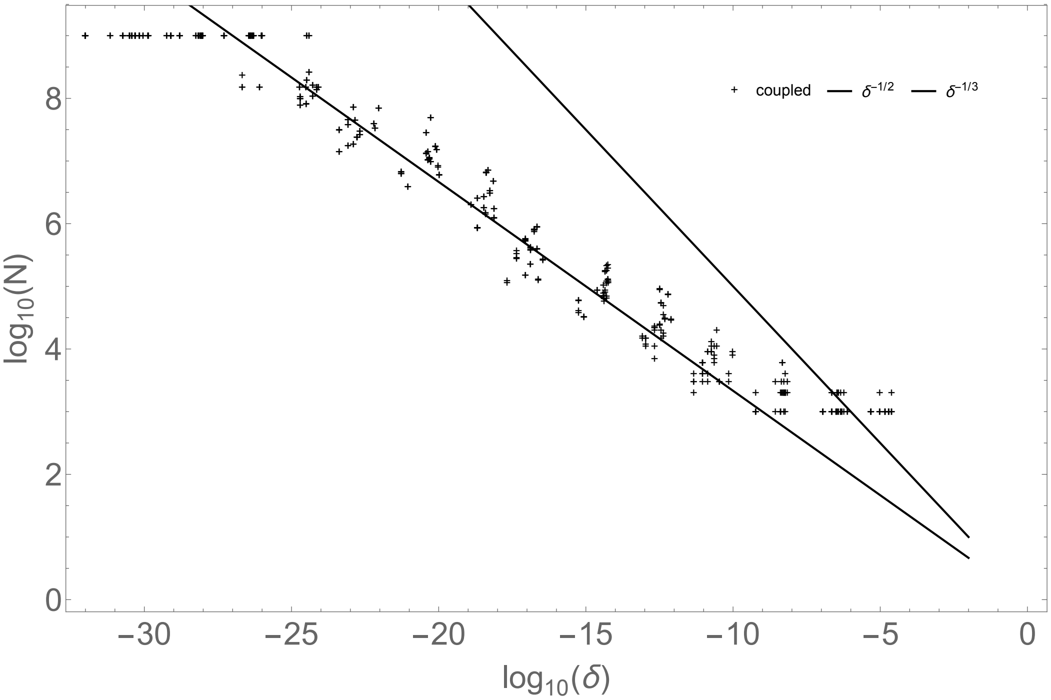

Figure 4.24: Shadowing plot for the coupled cubic and quadratic mapping.

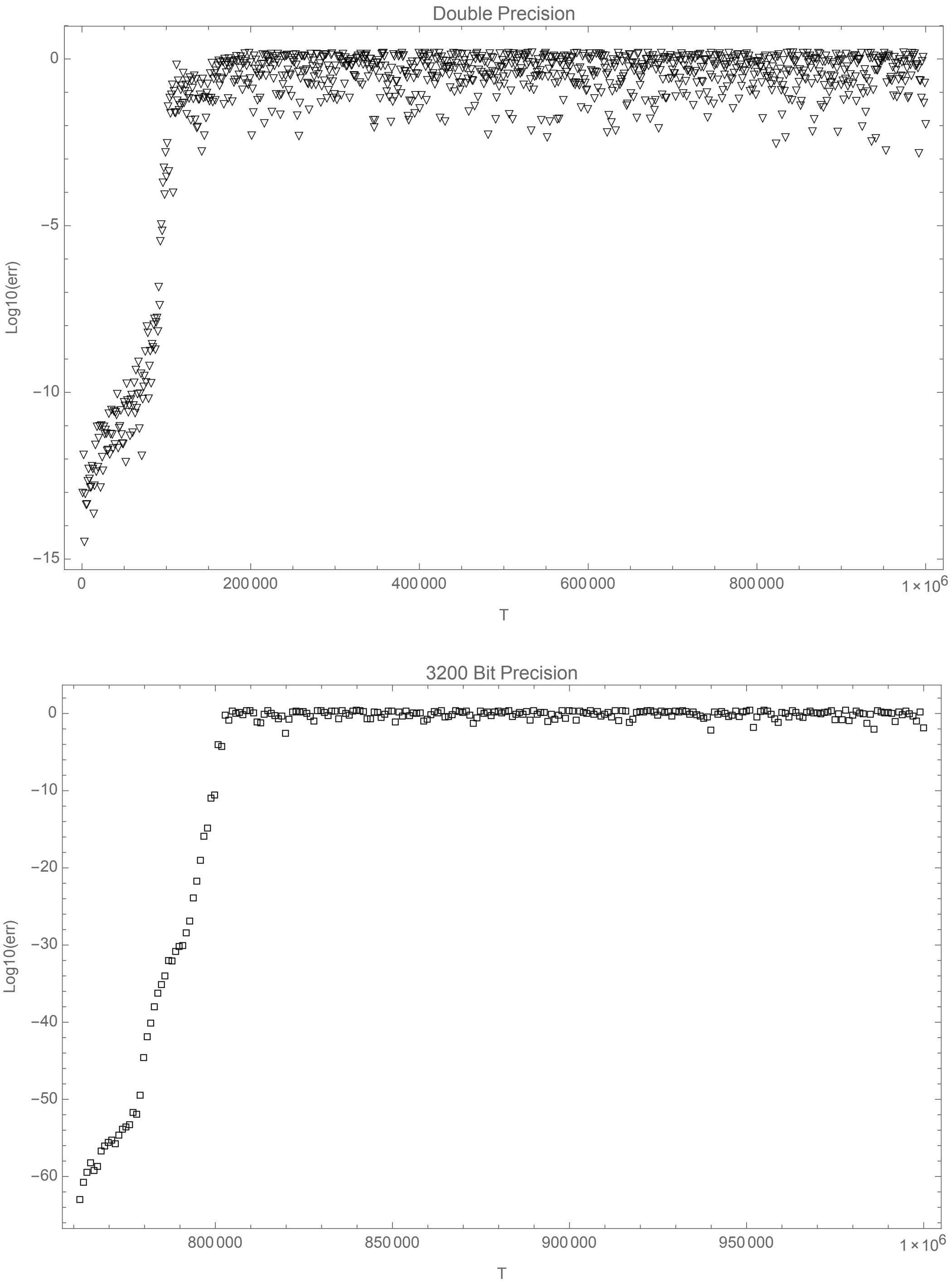

Figure 4.25: Shadowing of orbits. Shadowing for double and 3200 bit precision. We plot the RMSD, respectively, from the 6400 Bit trajectory. Note that the 3200 bit trajectory is within 10^{-20} after 8 x 10^5 iterations.

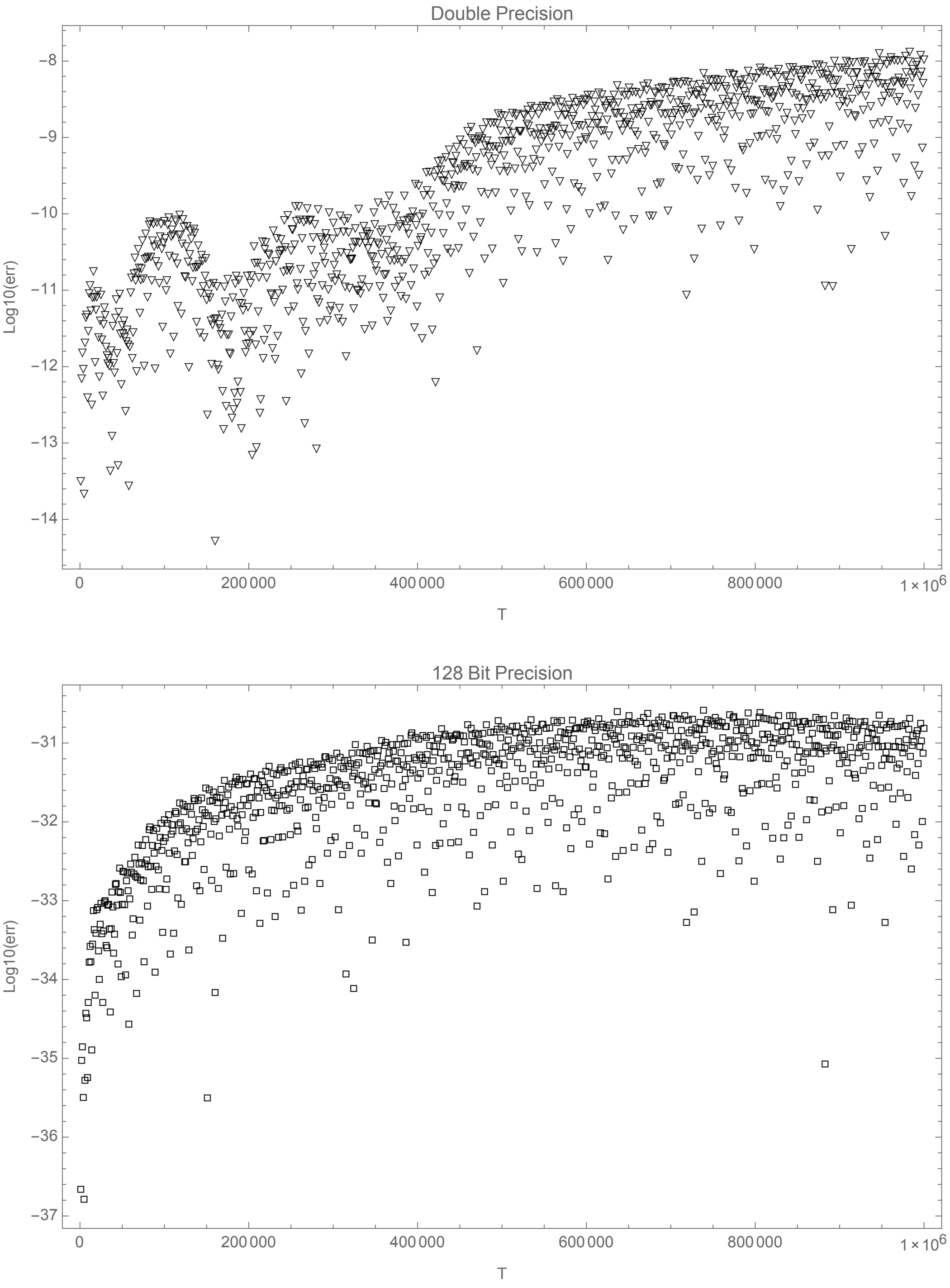

Figure 4.26: Shadowing plot for a regular orbit.

4.5.2 Accuracy and Precision of Frequencies

By using the shadowing results for orbits, we are now in a position to demonstrate the accuracy of frequencies by choosing a high enough precision for our orbit computations. Starting with an initial condition of $(.69, .7, 0, 0)$, we analyze the frequency with increasing precision and observe consistent diffusion in the frequency space. Observe that the frequencies of the 3200 bit and 6400 bit orbits are identical to approximately 10^6 iterations.

As a further test and illustration of the frequency analysis and to gain insight into the authenticity of the orbit, we perform the frequency analysis over 2.5 x 10^6 iterations in chunks of $2^8, 2^9, 2^{10}, 2^{14}, 2^{16}, 2^{18}$ for the initial condition (.69,.7,0,0). On a torus, we expect the frequencies to converge as we increase the number of data points, but for this wandering orbit we note that the irregularity of the frequencies persists to high sample lengths up to 2^{18} (Figure 4.30). Although we observe a kind of averaging effect with increasing sample length (Figures 4.29 and 4.30), it is important to note that for longer sample lengths (e.g., 2^{20}) (not shown), the FFT method does not converge for this orbit. In general, we find that a lack of convergence at any sample length is an indicator of chaotic orbits or orbits that escape in too short a time for an accurate FFT.

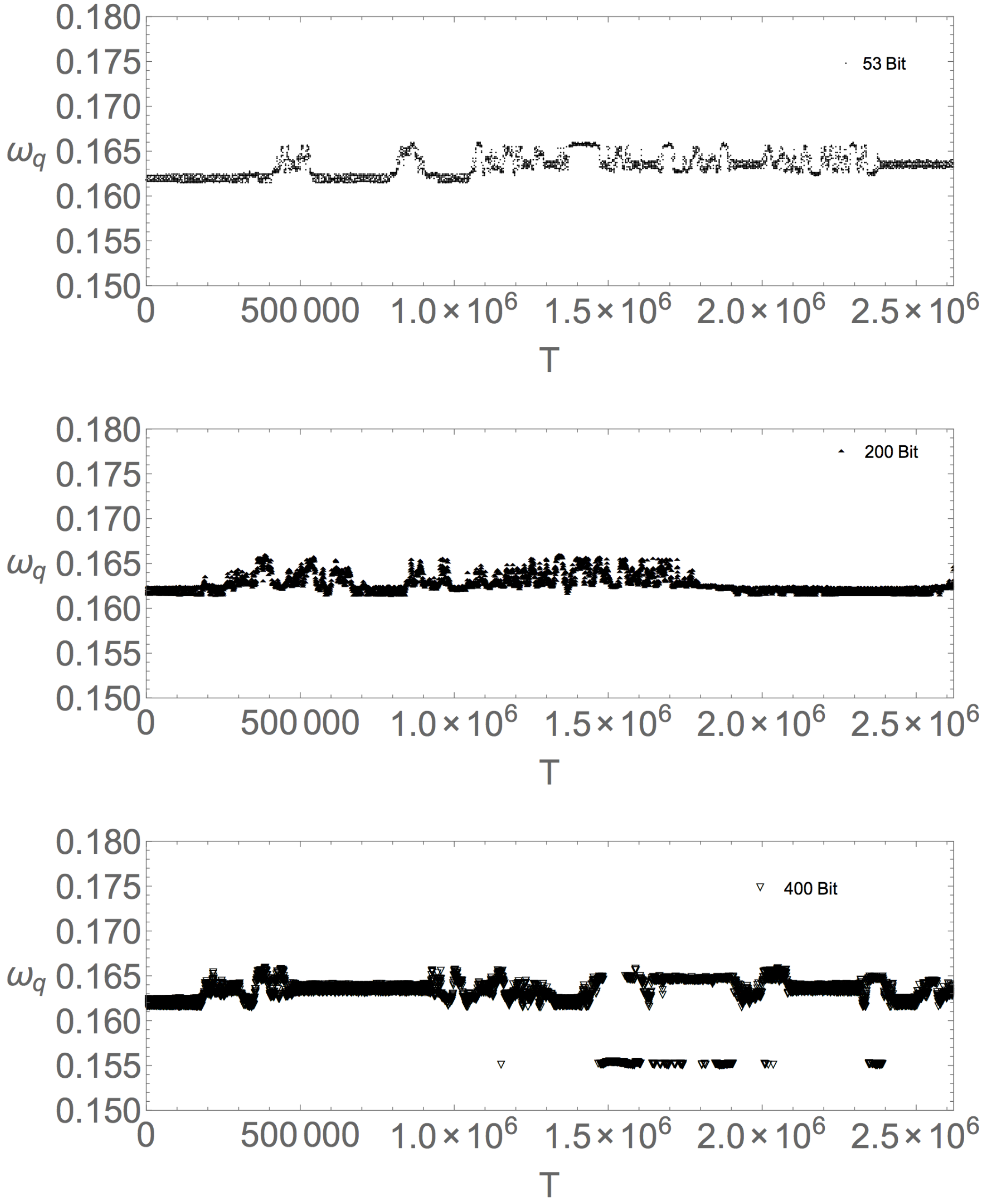

Figure 4.27: Frequency shadowing for the coupled cubic-quadratic mapping (I). Although all plots are qualitatively similar, notice the similarity between successive plots as we increase precision.

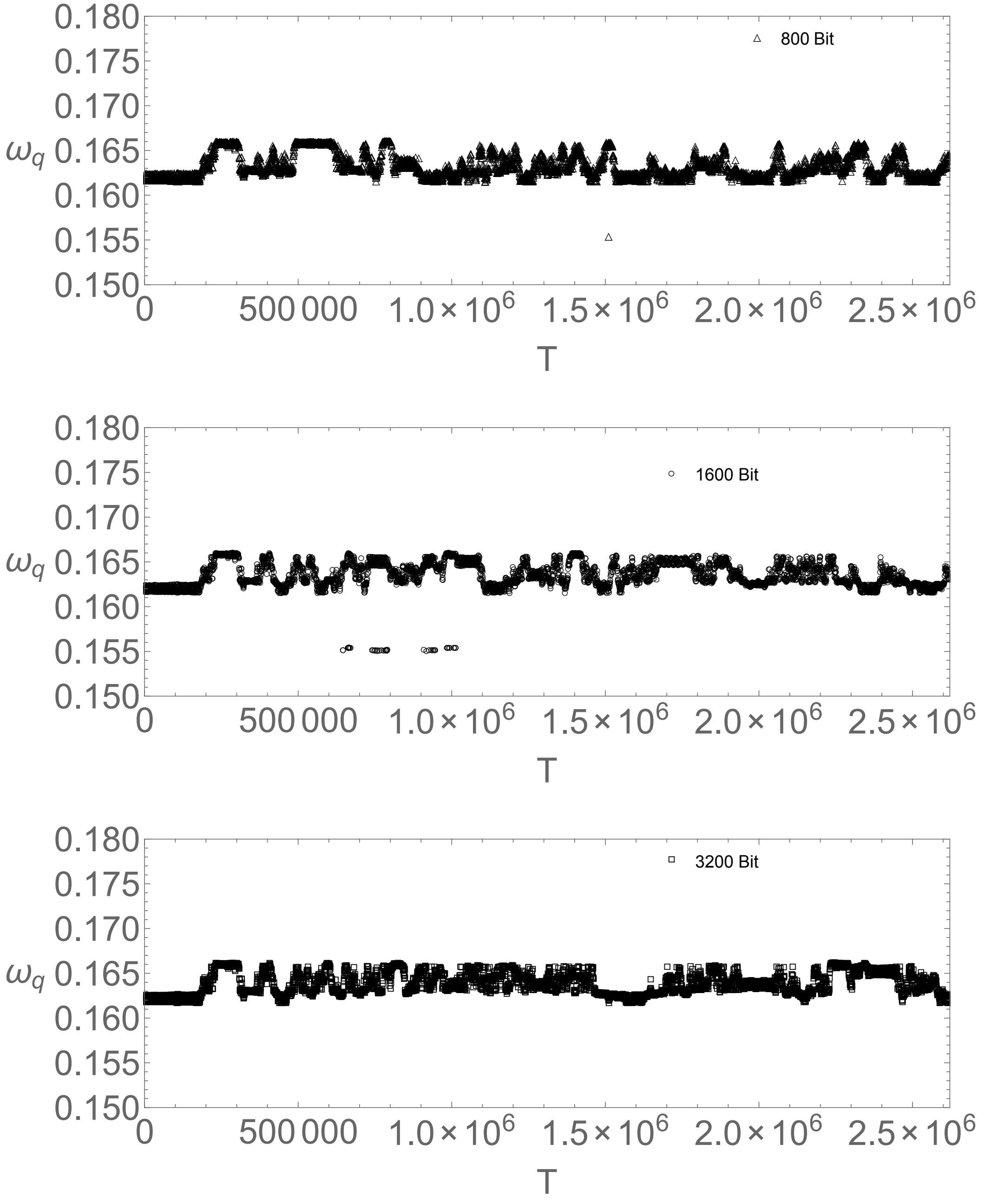

Figure 4.28: Frequency shadowing for the coupled cubic-quadratic mapping (II). Although all plots are qualitatively similar, notice the similarity between successive plots as we increase precision.

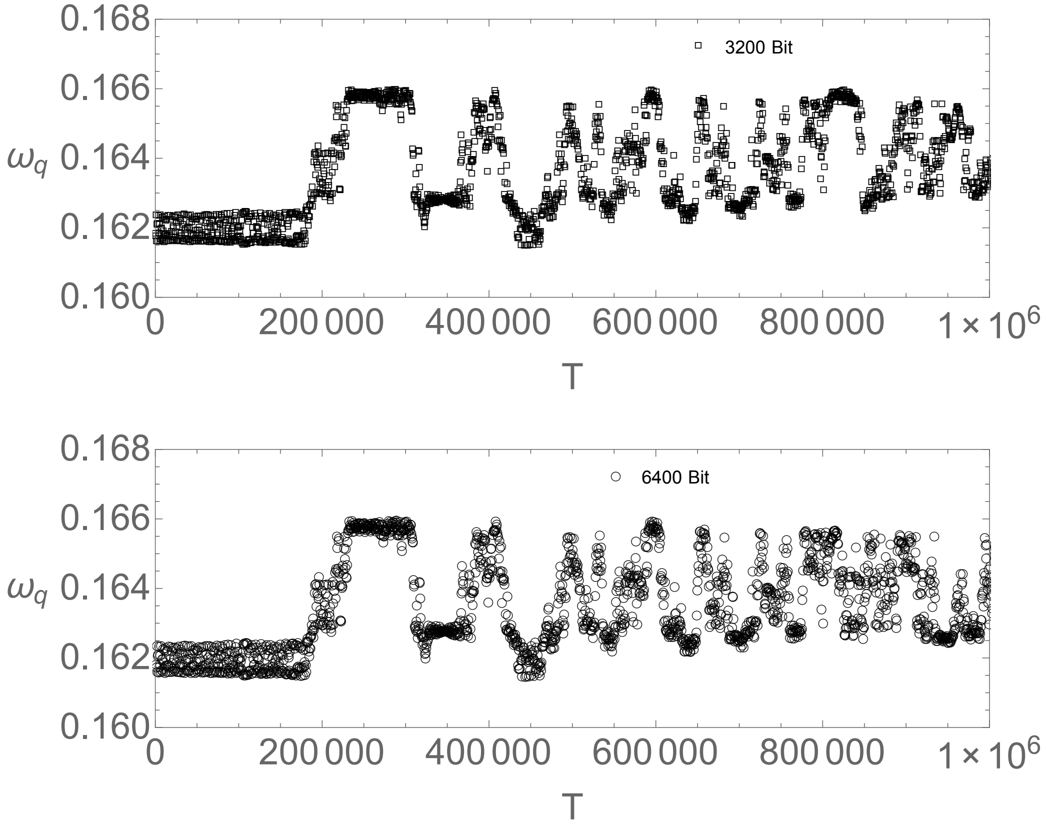

Figure 4.29: Frequency shadowing for the coupled cubic-quadratic mapping (III). Comparison of the 3200 bit and 6400 bit trajectories reveals that the frequencies are identical until approximately 10^6 iterations.

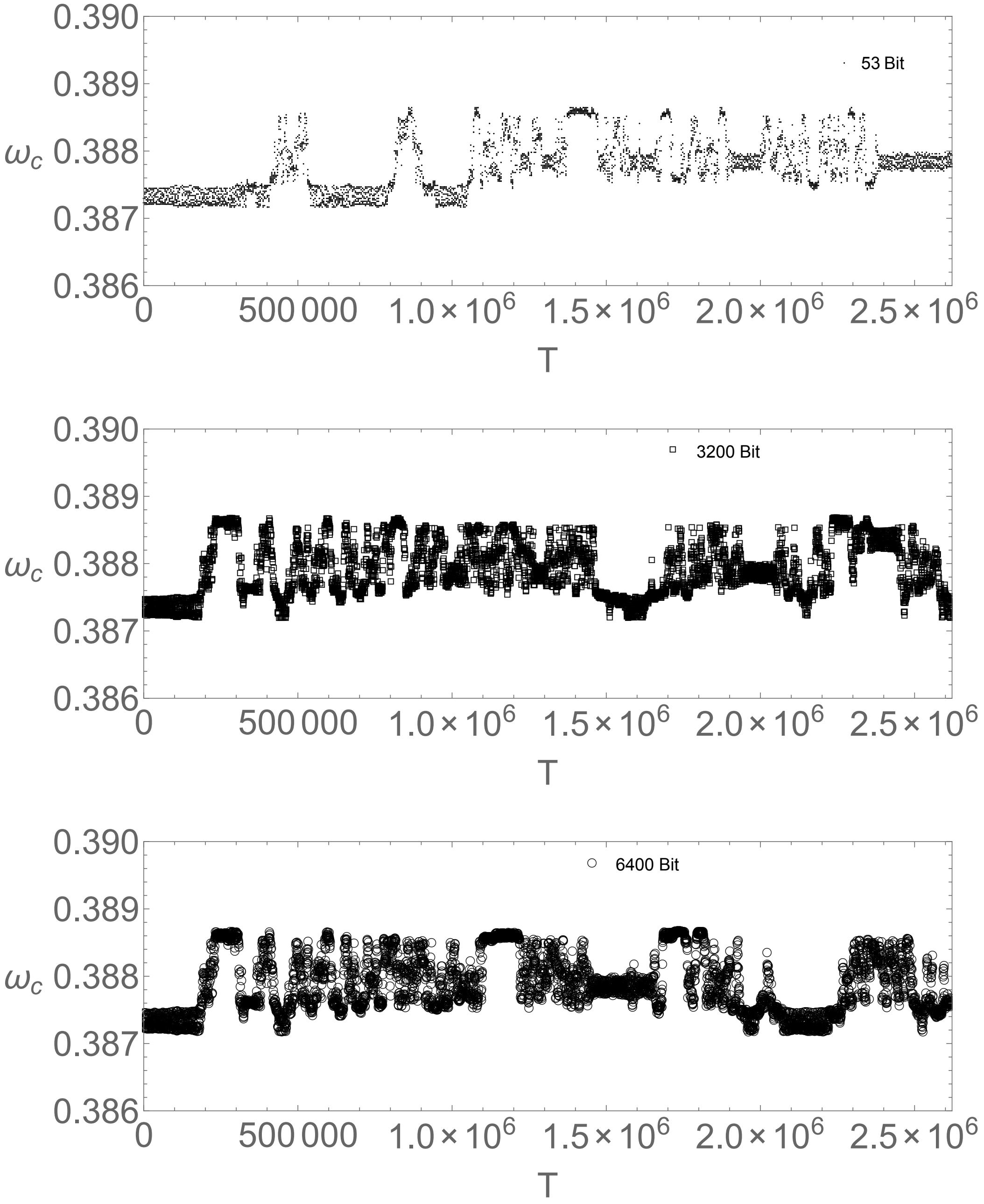

Figure 4.30: Frequency shadowing for the coupled cubic-quadratic mapping (IV). The 53 bit (double precision), 3200 bit, and 6400 bit trajectories are qualitatively similar.

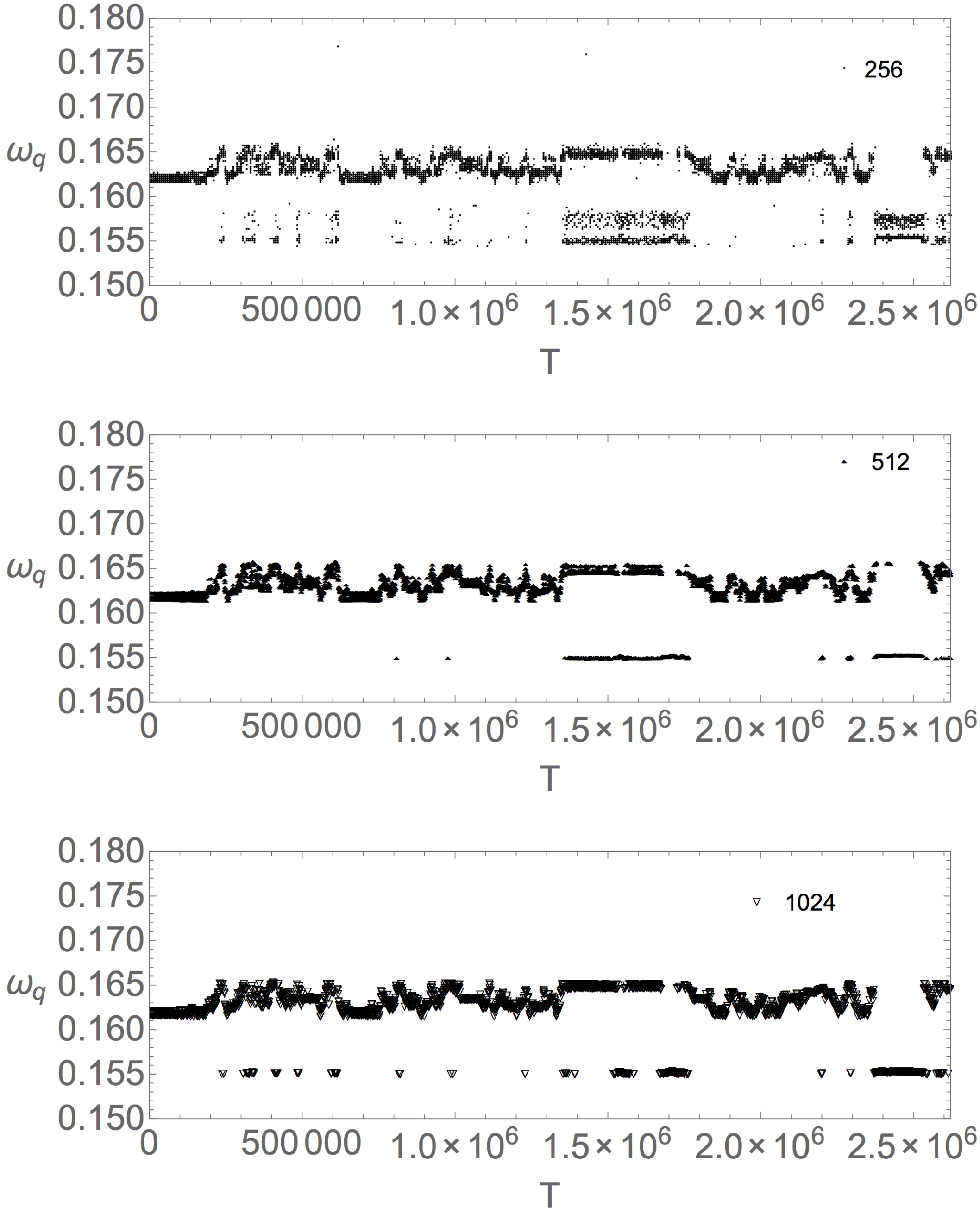

Figure 4.31: Frequency shadowing at different sample lengths (I). Frequencies of the orbit with initial condition of $(.69, .7, 0, 0)$ in chunks of $2^8, 2^9, 2^{10}, 2^{14}, 2^{16}, 2^{18}$. Note that the irregularity of the frequencies persists to high sample length.

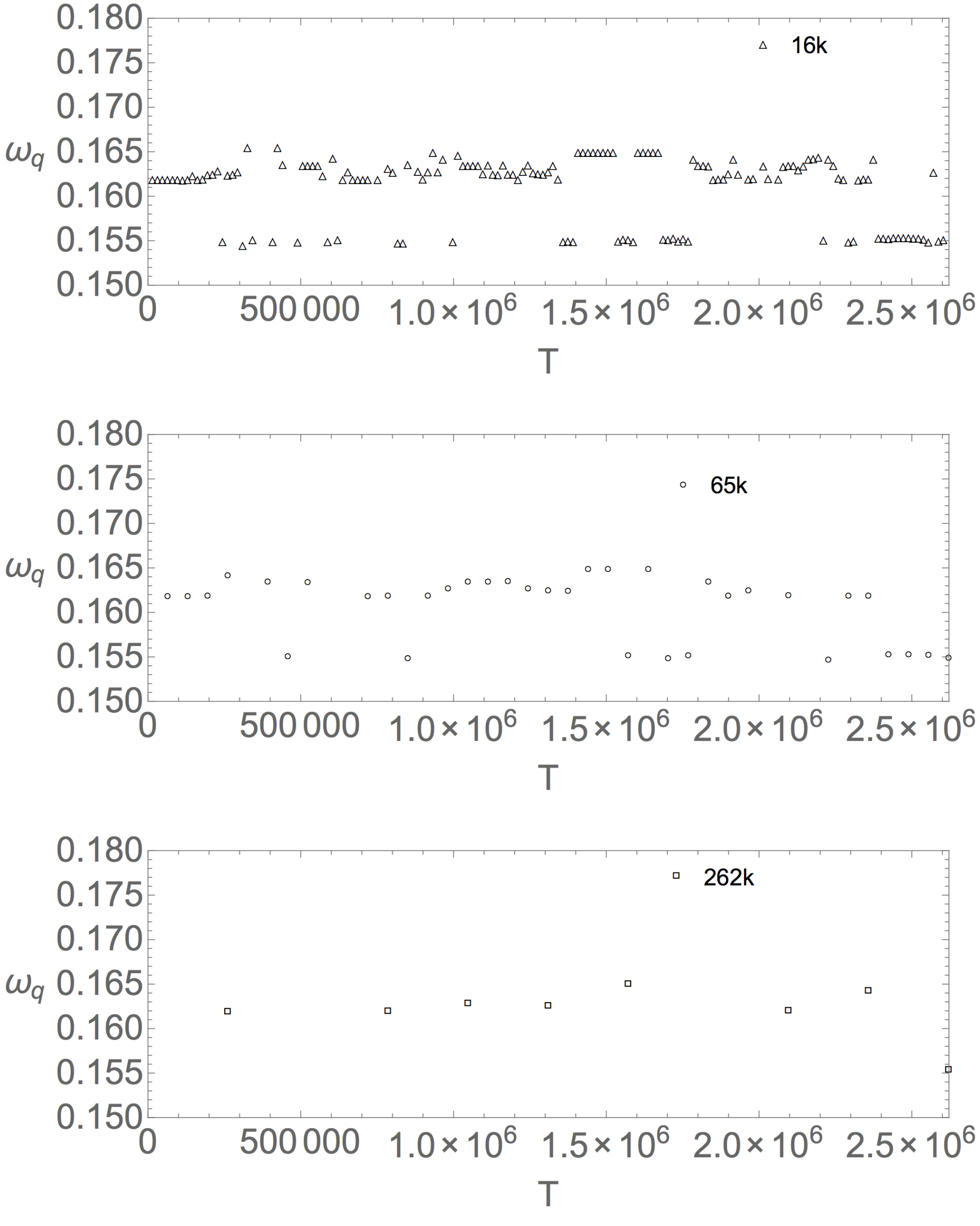

Figure 4.32: Frequency shadowing at different sample lengths (II). Frequencies of the orbit with initial condition of $(.69, .7, 0, 0)$ in chunks of $2^8, 2^9, 2^{10}, 2^{14}, 2^{16}, 2^{18}$. Note that the irregularity of the frequencies persists to high sample length.

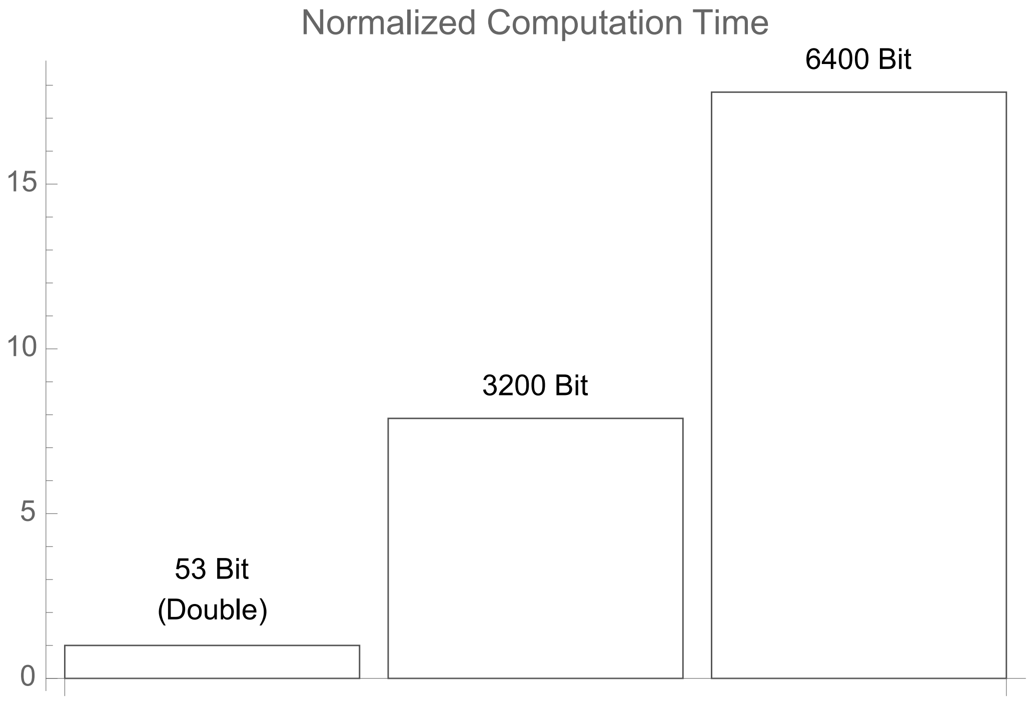

Figure 4.33: Normalized computation times for various precisions.

Chapter 5

Visualizing Tori in Higher Dimensions

5.1 Canonical Transformations and Higher Dimensional Symplectic Mappings

As we have seen in earlier chapters (Chap. 1, Figure 1.7; Chap. 3), coupling an additional degree of freedom leads to complicated pictures in the usual $p_i - q_i$ projections in phase space. Since these are not simple, closed curves in this projection, it is not possible to take the correct rotation number (by measuring the angle of rotation around a center as in Eq. (1.36)) of the orbit in these planes. As added evidence that we are no longer in the correct projection space, taking the rotation number (not shown) of these curves no longer agrees with the frequencies obtained via FFT (Chap. 4). When the perturbation from the other degree of freedom is small (cf. Figures 3.7 and 4.22 (a), the rotation number obtained may remain close but takes even longer to converge than usual. Taking the rotation number of the more complicated sub-plane projections (e.g., Figure 1.7, 3.7, and 4.22 (b)) yields an incorrect value due to the contribution from the additional frequency.

The difficulty arises because of the increased dimensionality of the system, which increases the number of frequencies. Upon coupling, each curve in the $p_i - q_i$ plane has a contribution from the other frequency. For example, in two dimensions, we are used to seeing a simple curve in the $p-q$ plane, as shown for the uncoupled cubic and quadratic maps in Chap. 3. These simple curves can be thought of as resulting from the Poincaré section of a higher dimensional quasiperiodic flow on a torus. Upon coupling however, the trajectory is no longer a simple closed curve, due to the effect of one degree of freedom on the other. One can think of the quadratic orbit being "carried" along this new torus some distance corresponding to the frequency of the cubic contribution, and vice versa; hence, upon one iterate of the map, a point in the $P-Q$ plane is carried to a new point that is remarkably different from the equivalent uncoupled motion. This is responsible for the complex curves depicted in Chap. 1 for the coupled standard mapping, and Chap. 3 for the coupled cubic-quadratic. Figure 5.1b shows a projection of this higher dimensional torus, and reveals how the triangular orbit of the quadratic mapping is coupled to an elliptic cubic orbit. In the usual $P-Q$ projection, the orbit is complicated (Figure 5.1a), but an appropriately oriented Poincaré section (Figure 5.2 and Sec. 5.3) reveals simple, closed curves.

To visualize a higher-dimensional trajectory, it is desirable to decompose the orbit into a set of $p_i - q_i$ projections in phase space [82]. In two dimensions, these are just the usual $p-q$ (cubic) and $P-Q$ (quadratic) planes, respectively. But in higher dimensions, the addition of an extra degree of freedom means that these projections may no longer be ideal. Tori become warped and rippled from coupling (e.g., Figures 3.7, 3.9, 5.1, 5.3, and

5.4), and the new projection plane must be appropriately oriented to account for these effects and yield a simple, closed curve. If one tries to take the rotation number of a higher dimensional curve by projection into a two dimensional plane, it must be the correct plane; one that results in a simple closed curve.

To arrive at the correct projection, one looks for a canonical transformation S satisfying

$$S_i^{\alpha} J_c^{ij} S_j^{\beta} = J_c^{\alpha\beta}, \tag{5.1}$$

where J is the canonical matrix given in Eq. (1.4). That is, we look to transform the coupled cubic-quadratic mapping into a set of new coordinates that reveal the existence of two simple closed curves in the phase space. The simplest such transformation[1] is a linear one given by

$$\begin{aligned} p' &= a_{11}p + a_{12}q + a_{13}P + a_{14}Q \\ q' &= a_{21}p + a_{22}q + a_{23}P + a_{24}Q \\ P' &= a_{31}p + a_{32}q + a_{33}P + a_{34}Q \\ Q' &= a_{41}p + a_{42}q + a_{43}P + a_{44}Q. \end{aligned} \tag{5.2}$$

Note that the primes indicate a coordinate transformation here. Below, we use the data visualization software GGOBI to visualize the four-dimensional data and obtain preliminary data toward projections of this form.

---

[1] This rotation is only a first step toward transforming the coordinates. Due to the warping, rippling effect of the coupling a rotation alone may not suffice, but as we will see, provides an effective means of visualizing the higher-dimensional data.

5.2 Projections of Higher Dimensional Data: Unwinding the Torus

GGOBI is an open-source visualization system for exploring data in higher dimensions [130]. GGOBI was developed and is mainly utilized as statistics software, but for our purposes, it allows one to manipulate data in higher dimensions and obtain projection coefficients that will transform the raw data into the projection shown onscreen. Screenshots of a typical GGOBI session are shown in Figure 5.1. In Figure 5.1(a), we see the $Q-P$ projection of a trajectory resulting from 10^5 iterations of the coupled cubic-quadratic mapping with initial conditions $(.65, .65, 0, 0)$. Figure 5.1(c) shows the $p-q$ projection, and Figure 5.1(b) shows a projection into a plane given by the projection coefficients shown in the bottom right of the screenshot. The selection of highlighted points is the same in each subfigure, merely in different projections. Notice that the projection in Figure 5.1(b) resembles a torus with triangular (highlighted) and elliptical cross-sections. This is a preliminary indication that in the appropriate projection two simple closed curves will be revealed, providing further evidence of tori.

As demonstrated in Chap. 3, orbits of the uncoupled cubic (with $t = 1.1$) and quadratic (with $\tau = .9864$) maps are elliptic and triangular, respectively. It is helpful to consider the first iterate of the coupled map when the initial conditions begin at $(p, q, P, Q) = (p_o, q_o, 0, 0)$. Due to the coupling (Eq. (3.10)), the trajectory "jumps" to a set of values (p_1, p_2, P_1, Q_1) where P_1 and Q_1 are non-zero. In a sense, one can think of the quadratic

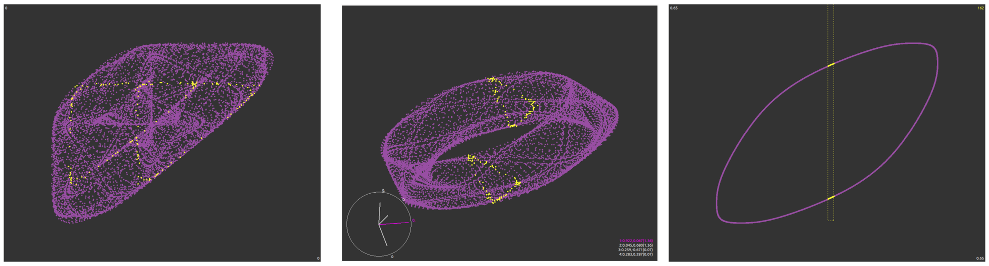

(a) (b) (c)

Figure 5.1: The coupled cubic-quadratic map in GGOBI. (a). The $Q-P$ plane. (b) A projection of the mapping's four-dimensional phase space, suggesting a torus with a elliptical and triangular cross-sections. (c) The $p-q$ plane.

trajectory starting at a new set of initial conditions (P_1, Q_1) that determine the orbit and frequency of the quadratic contribution to the mapping. For example, $(P, Q) = (0, 0)$ is an equilibrium point in the uncoupled quadratic map, but $(p_0, q_0, 0, 0)$ in the coupled map usually has a non-zero frequency that is close to the frequency of an uncoupled orbit of the quadratic mapping with initial conditions close to the (P, Q) coordinates after one iteration of the map (p_1, q_1, P_1, Q_1). We can calculate the frequencies of the coupled orbit via the FFT method (Chap. 4) and find an uncoupled orbit with an identical (to as many decimals as accuracy permits) frequency (Figure 5.5). For these reasons, in some projection space we expect to find a closed curve that closely resembles[2] a triangular-shaped orbit of the uncoupled quadratic map.

What is the projection in Figure 5.1b? In other words, what are we looking at? We are looking at a two dimensional projection of the

---

[2] It may be necessary to apply an additional transformation to undo the warping of the axes.

four-dimensional Poincaré section corresponding to the 4D coupled mapping. Below, we will visualize this four-dimensional object in another manner. For now, we refine the results from GGOBI to obtain a good approximation of a closed curve in the appropriate sub-planes given by Eq. (5.2).

5.2.1 The Projection Matrix

We obtain a projection that approximately locates a simple closed curve resulting from the quadratic contribution to the coupled mapping (Figure 5.2). This is the triangular orbit that we expect from the uncoupled quadratic map (cf. Figures 3.1 and 3.4). The projection coefficients from GGOBI (Figure 5.2), in matrix form (cf. Eq. (5.2)), are

$$S = \begin{pmatrix} a_{11} & a_{12} & a_{13} & a_{14} \\ a_{21} & a_{22} & a_{23} & a_{24} \\ -3.81/1.36 & -.002/1.36 & .925/.07 & 0 \\ -.002/1.36 & -3.76/1.36 & 0 & .927/.07 \end{pmatrix}. \tag{5.3}$$

The numbers obtained from the GGOBI projection are the projection coefficients for half of the transformation; the half corresponding to the plane shown in Figure 5.2. Eq. (5.1) can be written as $SJS^T = J$, and since we look for an orthogonal coordinate transformation, we have $S^T = S^{-1}$. This leads us to solve the equation $J^{-1}SJ = S$ by comparison for the coefficients in Eq. (5.2). Doing so, we have

$$S = \begin{pmatrix} 0.999775 & 0 & 0.0211956 & 0.000111263 \\ 0 & 0.999782 & -.000111023 & 0.0208724 \\ (-3.81/1.36 & -.002/1.36 & .925/.07 & 0)/13.2172550 \\ (-.002/1.36 & -3.76/1.36 & 0 & .927/.07)/13.245742 \end{pmatrix}. \tag{5.4}$$

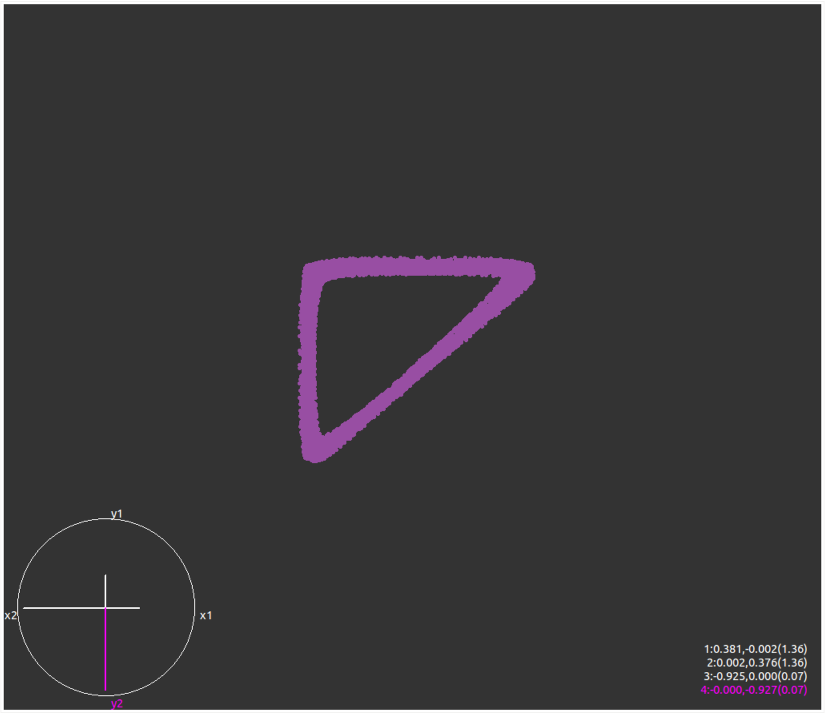

```
1:0.381,-0.002(1.36)
2:0.002,0.376(1.36)
3:-0.925,0.000(0.07)
4:-0.000,-0.927(0.07)
```

Figure 5.2: Projection of the coupled cubic-quadratic map in GGOBI. Note the four-dimensional axis (left) and projection coefficients (right). We rotate the data in four dimensions until we observe an approximately simple, closed curve.

The dividing factors in rows 1 and 2 are to normalize the vector to unity. Simplifying gives

$$S = \begin{pmatrix} 0.999775 & 0 & 0.0211956 & 0.000111263 \\ 0 & 0.999782 & -0.000111023 & 0.0208724 \\ -0.0211956 & -.000111023 & 0.999775 & 0 \\ 0.000111023 & -0.0208724 & 0 & 0.999782 \end{pmatrix}. \tag{5.5}$$

Checking to see if this satisfies Eq. (5.1), we compute $S_i^\alpha J^{ij} S_j^\beta$, which should yield

$$J_c^{\alpha\beta} = \begin{pmatrix} 0 & 0 & 1 & 0 \\ 0 & 0 & 0 & 1 \\ -1 & 0 & 0 & 0 \\ 0 & -1 & 0 & 0 \end{pmatrix}. \tag{5.6}$$

We obtain

$$J_c^{\alpha\beta} = \begin{pmatrix} -1.86 \times 10^{-18} & 9.40 \times 10^{-22} & 1 & 0 \\ 0 & -3.47\times^{-18} & 8.47\times^{-22} & 1 \\ -1 & 4.24 \times 10^{-22} & 0 & 0 \\ -8.47 \times 10^{-22} & -1 & 0 & 0 \end{pmatrix}. \tag{5.7}$$

Figures 5.3 and 5.4 illustrates the effect of the transformation. In the cubic plane ($p' - q'$, approximately the usual $p - q$ plane of the uncoupled cubic), the effects are small (Figure 5.3, (a) and (b)). This is because the amplitude of the perturbation from the quadratic on the cubic is small; the scale of the quadratic trajectories is approximately 0.01 while orbits of the cubic map range from [-1,1] (Chap. 3). However, clearly an effect is observed. The cubic trajectory flattens out and becomes less whorled. The transformation in the $P - Q$ plane is much more drastic. The complex pattern of Figure 5.4(a) is revealed to be to be a simple, closed curve of

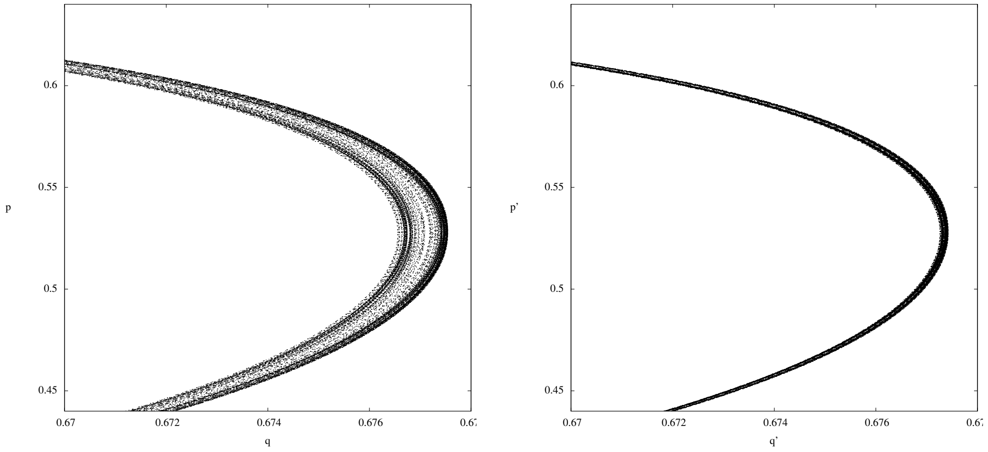

(a) (b)

Figure 5.3: The coupled and transformed cubic orbit.

triangular fashion (Figure 5.4, (b) and (c)), as we would expect from the phase portrait of the uncoupled quadratic. For comparison, we include a comparison between the transformed curve and an orbit of the uncoupled quadratic mapping which has the same frequency (Figure 5.5). By choosing initial conditions (uncoupled), we find an orbit of the uncoupled quadratic mapping with the same frequency (to nineteen decimals) as the coupled orbit.

5.2.2 Unwinding the Torus via a Simple Canonical Transformation

The form of S suggests seeking a transformation

$$S' = \begin{pmatrix} \cos\psi & 0 & \sin\psi & 0 \\ 0 & \cos\psi & 0 & \sin\psi \\ -\sin\psi & 0 & \cos\psi & 0 \\ 0 & -\sin\psi & 0 & \cos\psi \end{pmatrix}, \tag{5.8}$$

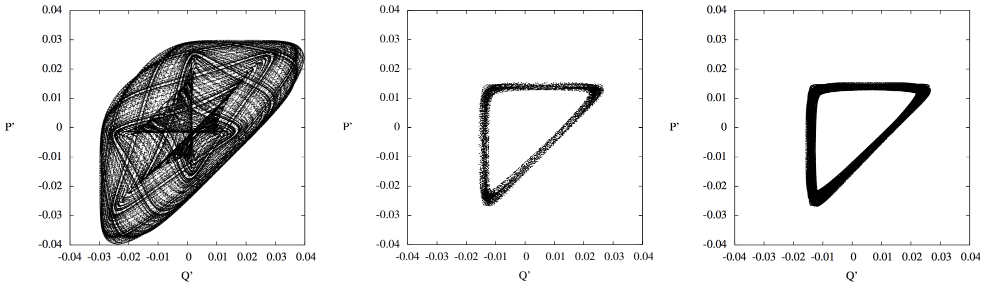

(a) (b) (c)

Figure 5.4: Symplectic transformation of the coupled cubic-quadratic mapping. (a) The map is plotted in the $P-Q$ plane and (b), (c) the transformed coordinates obtained from GGOBI and given in Eq. (5.2). 2×10^5 iterations are shown in (a) and (c), and the first 10^4 in (b).

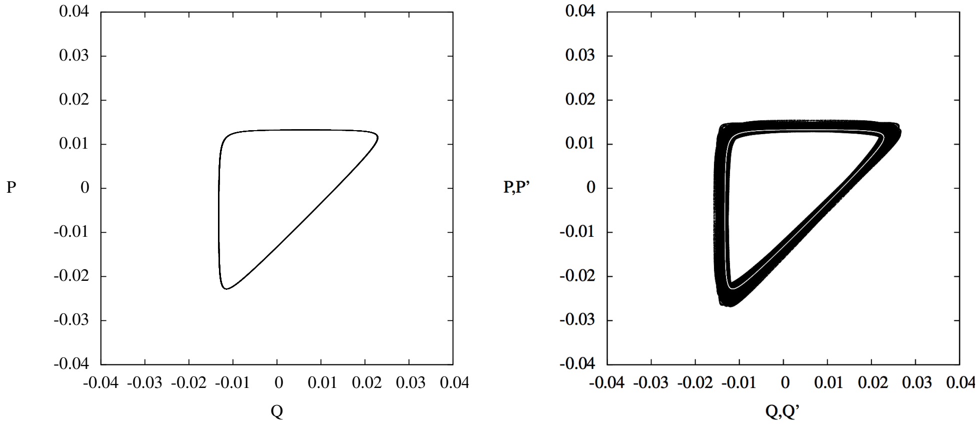

(a) (b)

Figure 5.5: Comparison of the uncoupled and transformed quadratic orbit. By choosing initial conditions, we find an orbit of the uncoupled quadratic mapping with the same frequency (to nineteen decimals) as the coupled orbit.

where ψ is an angle of rotation that can be systematically varied to find the best projection. In Figure 5.6 we show a series of projections in the $P' - Q'$ plane that demonstrate this procedure. Notice that if ψ is zero, we recover the identity matrix; i.e., if there is no perturbation to the $p_i - q_i$ coordinates, the $p_i - q_i$ sub-planes are the appropriate choice of coordinates.

5.3 A Higher Dimensional Poincaré Section Method

In Chap. 4, the frequency analysis method was used to demonstrate evidence for the existence of tori; in this chapter, we have shown that it is possible to find a projection demonstrating the existence of an approximately simple, closed curve (Figures 5.3-5.5). In this section we propose a method to demonstrate the existence of a simple, closed one-dimensional curve in an appropriate two dimensional sub-surface of the phase space (Figure 5.8). The rotation number (or frequency; see Figure 5.9) of this curve in the appropriate surface-of-section matches exactly (to numerical accuracy) that of the frequency analysis method, providing good evidence that the orbit lies on or near a torus.

In the literature, one finds reference to the "decompositions" of a higher dimensional Poincaré section. These are the $p_i - q_i$ projections referred to throughout this work, particularly in the previous section. However, it also possible to decompose a torus into two cross-sections. Ordinarily, one forms a torus from the cross product of two circles (or closed curves). One can then reverse the process and slice the torus in two orthogonal directions, yielding

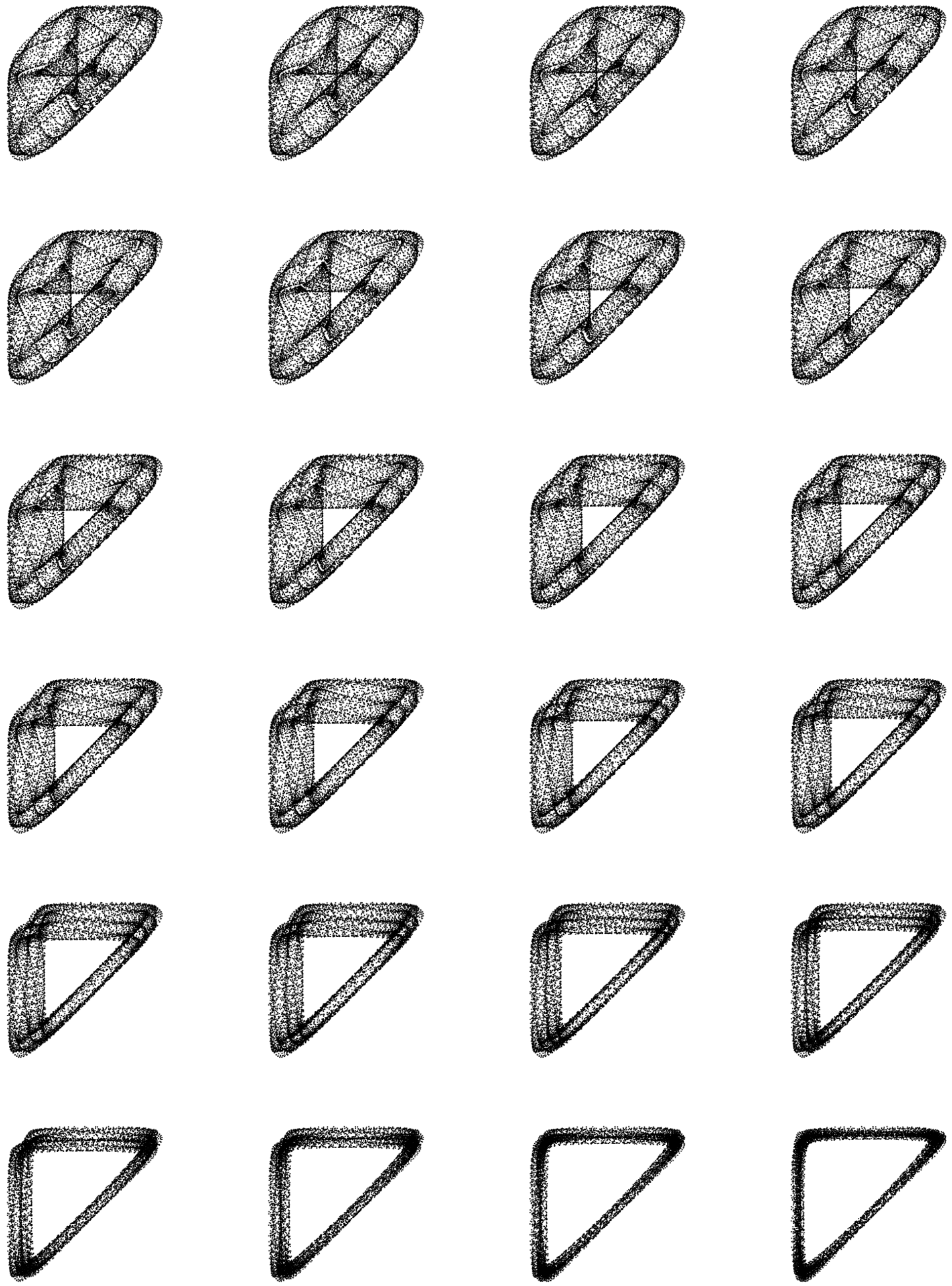

Figure 5.6: Unwinding the torus via a canonical transformation. We apply the transformation described in the text, successively increasing the angle until we approximate a simple, closed curve.

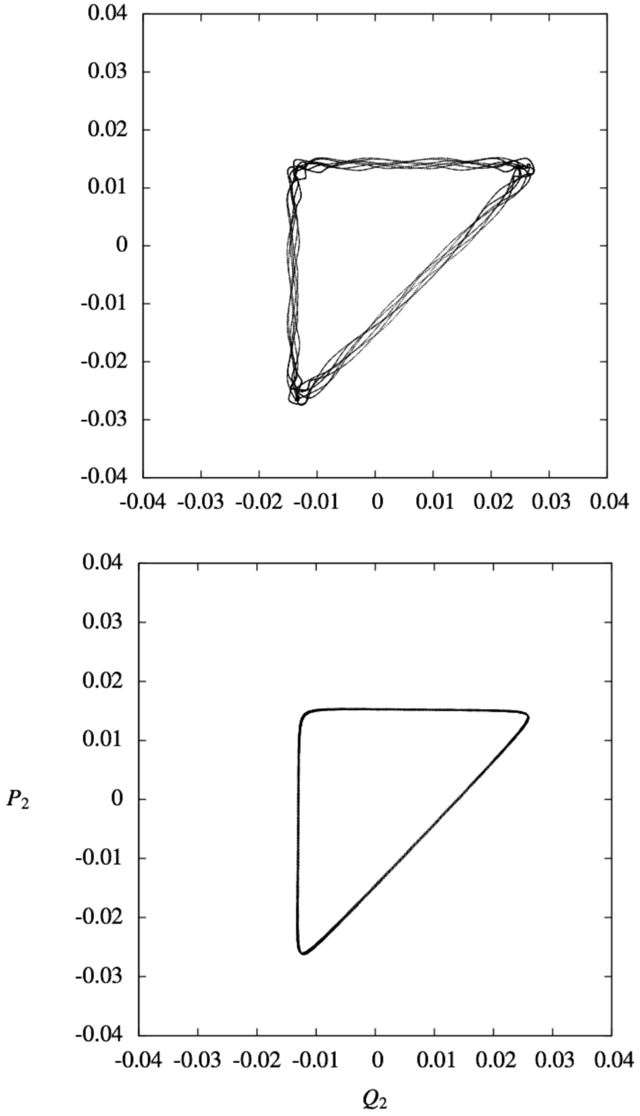

Figure 5.7: Comparison of unwound coupled orbit (top) and uncoupled orbit with matching frequency (to nineteen decimals). top: (.6419, .6419, 0,0), 10k iterations. bottom: uncoupled w matching frequency.

the two original closed curves. The familiar Poincaré section of flow on a torus is such a slice that yields a one-dimensional curve (Chap. 1, Figure 1.1). In higher dimensions, the section is itself a torus, as we now argue.

Consider the flow obtained from the Hamiltonian $H(J_i, \theta_i,)$ where $i = 1, 2, 3, \ldots N$. The phase space is $2N$-dimensional, the energy surface is $2N - 1$-dimensional, and the dynamics takes place on a N-dimensional torus. It is possible to take an appropriate Poincaré section of this torus to yield a $N - 1$-dimensional torus which is defined by $N - 1$ angles. If N is odd, we can decompose this torus into further sections defined by holding each respective angle constant. For example, if $N = 3$, the Poincaré section is a 2-dimensional torus. We can slice this two-dimensional section and yield two cross sections. If the flow is quasiperiodic, we will obtain two closed curves. We now demonstrate this process for the coupled cubic-quadratic mapping.

The process is simple and amounts to holding the angle of rotation, as defined in Eq. (1.36), for each respective $p_i - q_i$ sub-plane. To do this, we iterate the map and impose a condition to select points around (p_o, q_o). In a sense, we are taking a Poincaré section of an orbit in the cubic plane (cf. Figure 2.2), which is a line that is intersected by the orbit as the map is iterated. However, drawing a line in this manner would result in twice the number of points and a doubling effect when we plot the points in the $P - Q$ plane. Selecting points around (p_o, q_o) avoids this. this is analogous to taking a Poincaré section through a torus that selects only one “side”, which is the usual method that we are accustomed to seeing in discussions of the derivation of twist maps and reducing the flow by one dimension (Chapters 1 and 2; [82]). Results are shown in Figures 5.8 and 5.9. With an appropriate choice of the thickness of the Poincaré section, we obtain a simple, closed curve in a projection space (Figure 5.8) with a rotation number (Figure 5.9) that closely matches the results of the frequency analysis $\omega = 0.332656682319030....$

5.4 Discussion: Tori or Not Tori?

We note that the transformations of (5.2) and (5.8) are not perfect; we do not obtain a set of points that can be considered a one dimensional curve. Indeed, the trajectory seems “fuzzy”, and it may seem possible that this is in fact not a torus, but a stochastic orbit or a trajectory that is diffusing between tori[3]. Here we discuss these concerns. One, the GGOBI process is far from perfect. Rotating four dimensions of data by hand on a two dimensional screen is not easy, and not likely to yield an exact transformation. Second, the tori in question are perturbed by the coupling. The surface acquires ripples and is tilted in phase space. If one considers what a projection of such a rippled, tilted surface would look like, it is quite plausible that a projection will not yield a one-dimensional curve. No matter how we may project the surface, the curvature and ripples mean that there will always be some thickness to the curve obtained. It may be helpful to

---

[3] However, it is also possible that the fuzziness comes from the warping of the coordinates and cannot be removed by a simple rotation. This is left to future work.

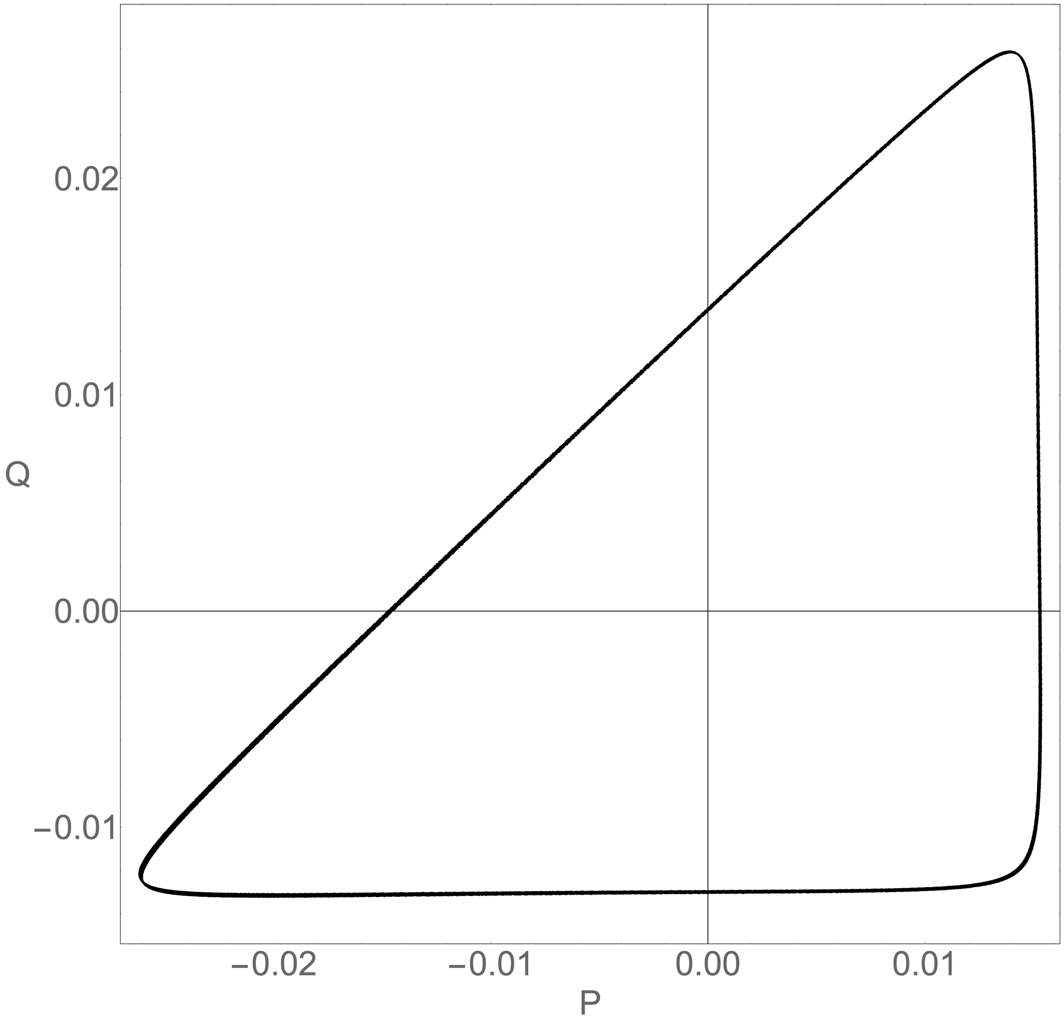

Figure 5.8: A higher dimensional Poincaré section We apply the surface of section method (Chap. 1) to the four-dimensional map by selecting those points in the $P - Q$ plane that correspond to the intersection of the plane $p = .65, q = .65$.

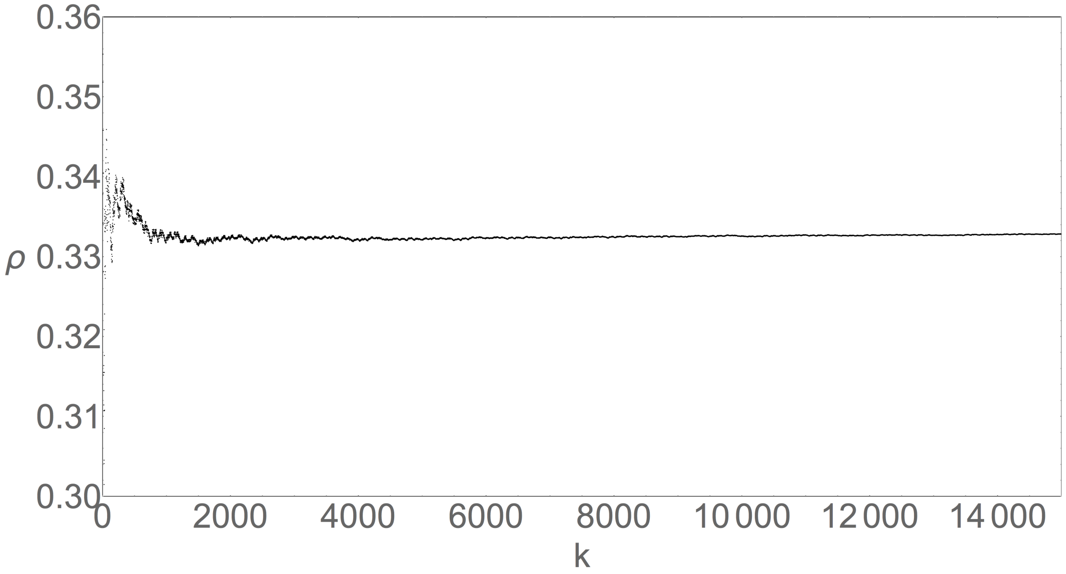

Figure 5.9: Rotation number via Poincaré section. We apply the surface of section method to the four-dimensional map and calculate the rotation number as described in Chap. 1. The result is close to that obtained via the frequency method ($\omega = .0.332656682319030...$).

think of this process as shining a light on a distorted three dimensional object with a rippled surface and casting a shadow on a wall behind the object. If the surface is rippled in each direction, then there are no perspectives that will yield a one-dimensional curve.

If the trajectory is in fact executing motion near but not on a torus, or wandering between two tori, we observe this in the frequency analysis (Chap. 4). In the case of constant frequencies (to nineteen decimals; see Chap. 4), we have good evidence that the orbit is near or on a torus. If we are not on a torus, there are two possibilities to consider: one, that the orbit is very close to a torus, but slightly wandering, and two, that the trajectory is well off. If the first case is occurring, then the only way to observe the “fuzzy” curve would be at a highly skewed perspective. In other words, if there are in fact two curves very close together, which would be necessary to escape detection in the frequency analysis, then the only way to observe their separation via a projection would be at a highly skewed perspective. If this is the case, there would be many other $P' - Q'$ projections that show the two nearby curves as one; we do not observe this.

It may seem from Figures 5.2 and 5.5 that in fact the trajectory is not a torus. After all, the width of the triangle is roughly a tenth of the amplitude of the orbit. But the regularity of the orbit in the projection (and a constant frequency of the orbit) is precisely what makes unlikely the possibility of this being an orbit that wanders between nearby tori. If an orbit wandered in such a manner, we would see a corresponding change in the frequency over the duration of the orbit (recall Chap. 4). We do not. In fact, we argue that it is the ripples in the surface in higher dimensions that result in this appearance. One might compare this to shining a light straight down a rippled piece of string or piece of paper, and projecting the results on the floor. Or perhaps more enjoyably, a piece of bacon that is cooked and rippled in every direction. Attempting to do this results in a projection that has more thickness than the object itself, because the ripples are what is projected.

We admit the possibility that the first scenario of an orbit executing motion between two nearby tori is occurring below the resolution of the frequency analysis method; we can only detect frequencies to nineteen decimals of accuracy. However, the structure of phase space and the long-term stability (10^{12}) of the orbit in question provides further evidence of the existence of a torus. See Chap. 6 for further discussion of this nature. Essentially, the stability of the orbit and the constancy of the frequencies implies that the curve lies on a torus or is sandwiched between tori.

Chapter 6

Numerical Explorations of Symplectic Mappings

6.1 Escape Times for the Coupled Cubic-Quadratic Mapping

To gain insight into the stability of orbits in the phase space, we scan along the $p - q$ diagonal for the initial conditions $(p, q, 0, 0)$ and plot the escape time [64, 97] (Figure 6.1). Notice the similarity between single (32 bits), double (53 bits), and 6400 bit precision. Further, the histograms (Figure 6.2) of the escape times for different precisions are similar, indicating that the results are qualitatively unchanged at different precisions.

6.2 The Escape Mapping: A Fast Tool for Visualizing Dynamics

To extend the results of the previous section to higher dimensions, we pick two coordinates and plot the escape times of orbits with different colors [100, 91] in the plane of the remaining coordinates (Figures 6.4 and 6.5). First, we implement the method for the Hénon Mapping (Chap. 3), as demonstrated by Figure 6.1. Escape times are colored with different colors for exit times. To investigate a region of interest, one may pick a series of

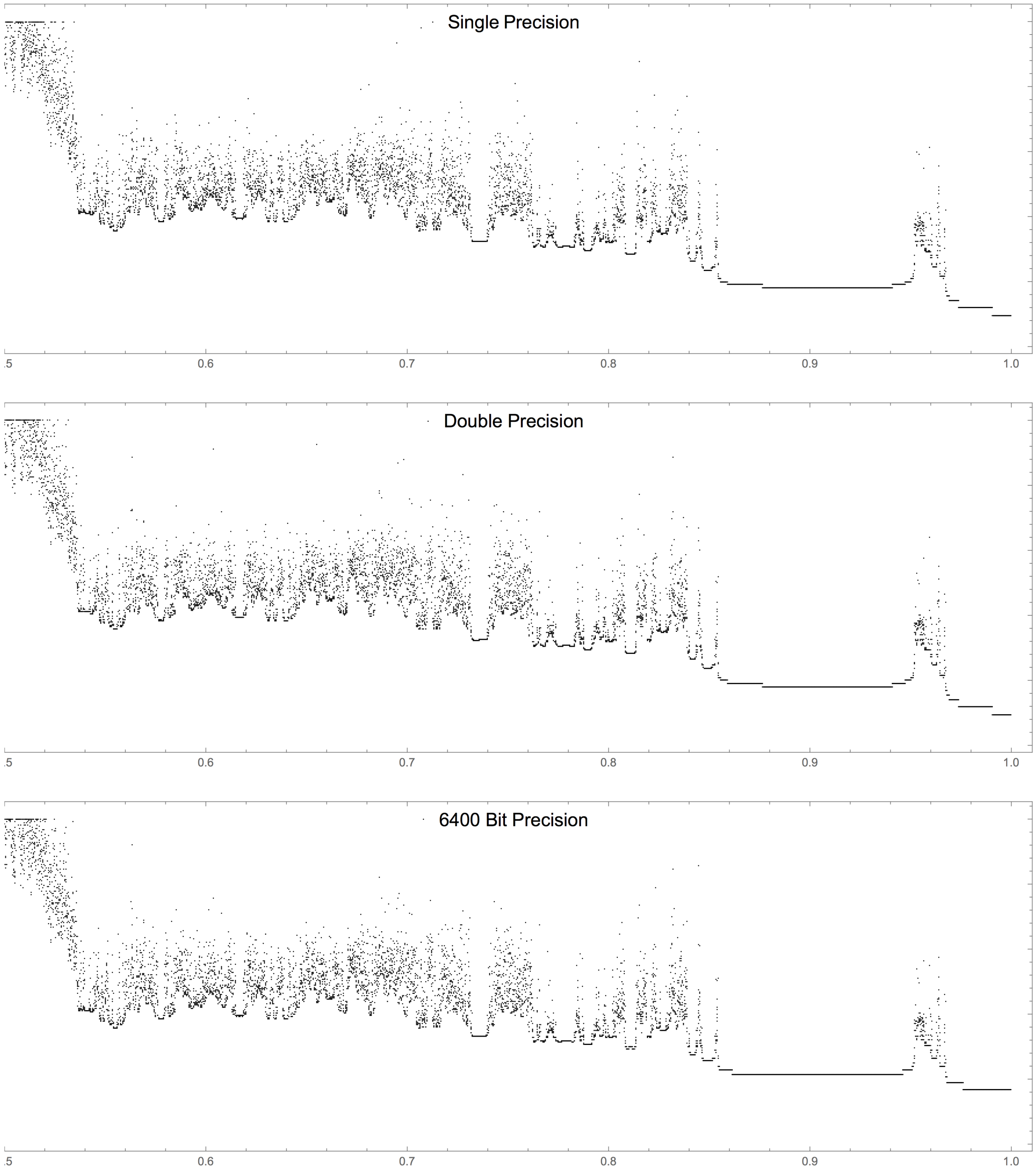

Figure 6.1: Exit times for the coupled cubic-quadratic mapping. We scan along the $q = p$ axis for the initial conditions $(q, p, 0, 0$ and measure the number of iterations before the 4D distance from the origin exceeds some threshold.

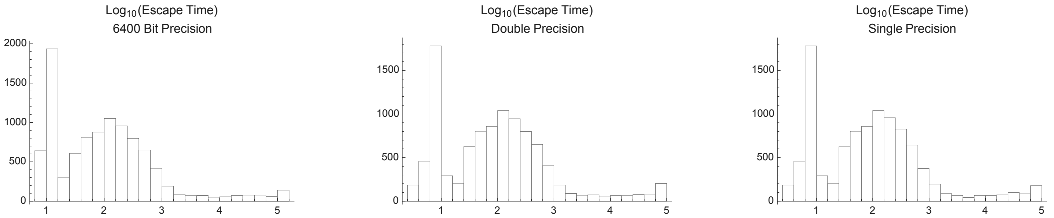

Figure 6.2: Histograms of escape times.

points in the $P - Q$ plane, and observe how the distribution of orbits in the $p - q$ plane changes. In this way, one may examine the stability of orbits in well-defined neighborhoods.

The chief advantage of the escape mapping is that it may be implemented in OpenCL or CUDA to utilize the massively parallel processing power of Graphics Processing Units. The advantage of GPU computing for these types of massively parallel tasks can be seen in Figure 6.3. As an example of a massively parallel computation, the Hénon Mapping was iterated for a 400×400 grid. Computation times are shown for CPU (Xeon) and GPU (others).

6.2.1 The Escape Mapping for the Hénon Map

Figure 6.4 shows the escape times of the quadratic Hénon Map,

$$x' = y + 1 - ax^2, \qquad y = bx, \tag{6.1}$$

for $a = 1.4, b = .3$. These were the values chosen in the original paper by Michelitsch and Rössler in their 1989 paper [100]. We include this example

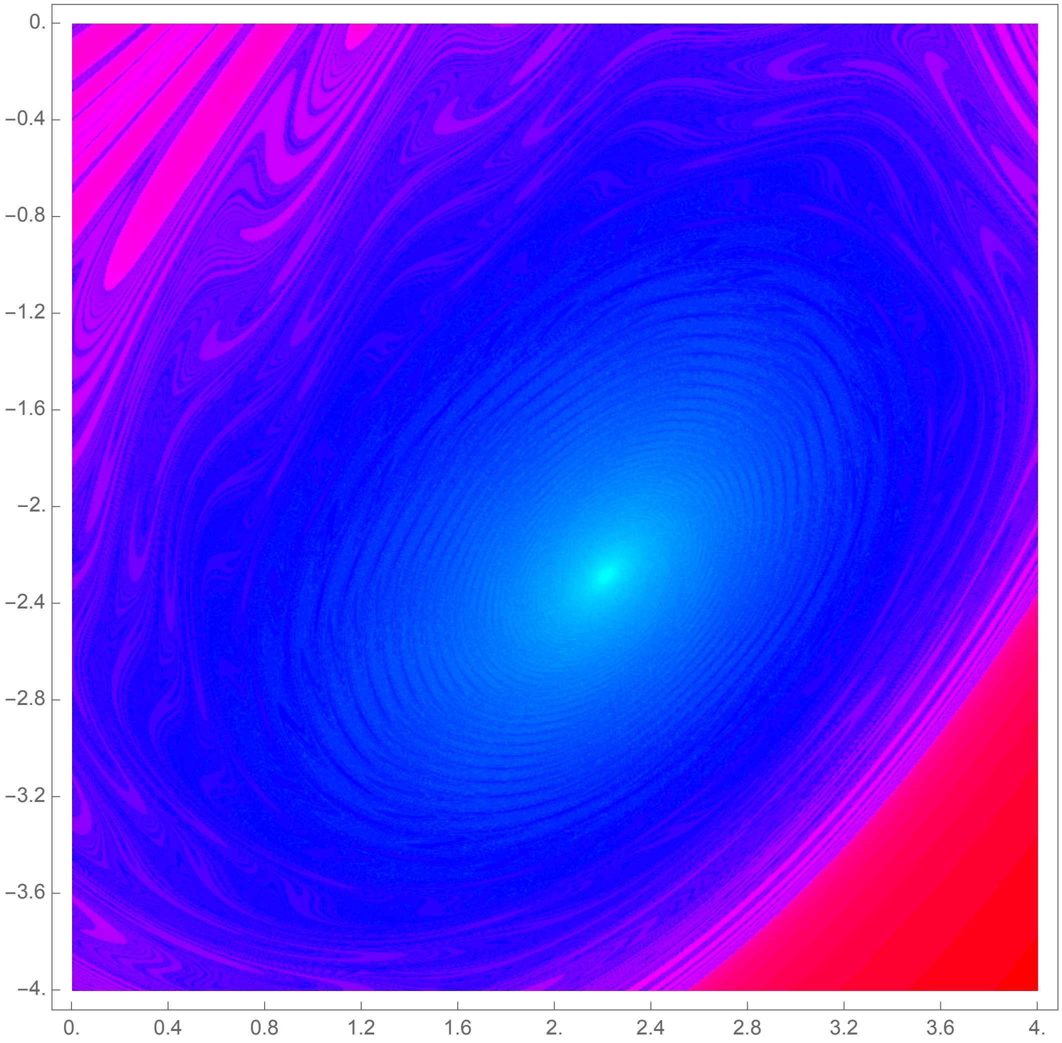

Figure 6.3: Escape times for the Hénon map. Increasing times are colored from red to blue.

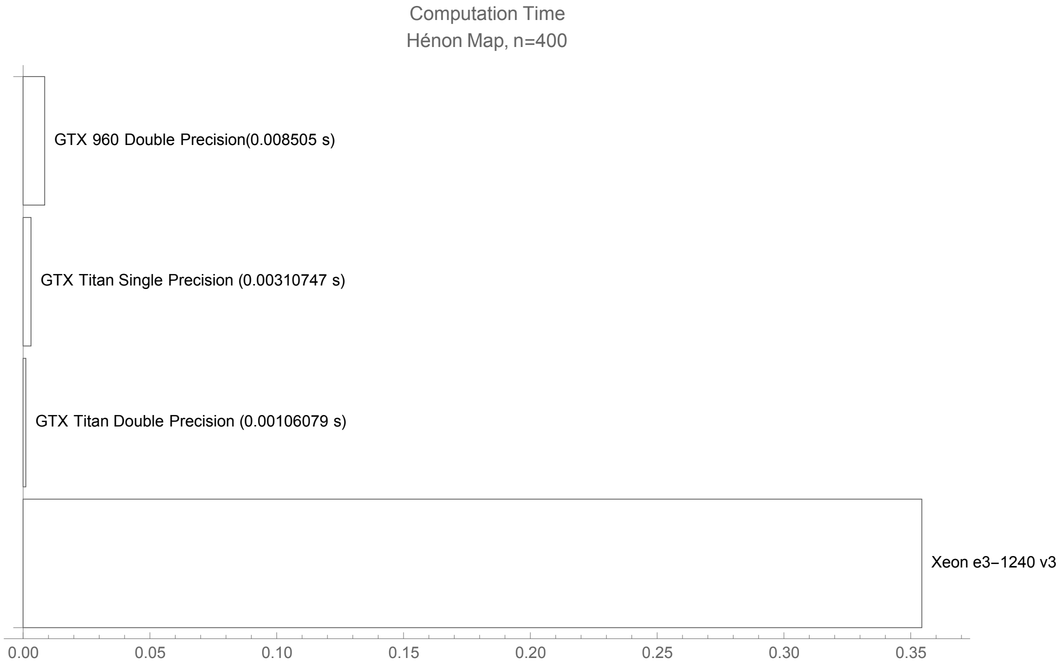

Figure 6.4: Benchmarking the escape times of the Hénon mapping. As an example of a massively parallel computation, the quadratic Hénon map was iterated for a 400×400 grid. Computation times are shown for CPU (Xeon) and GPU (others).

to demonstrate the escape time method for two dimensions and as a benchmark of GPU computing.

6.2.2 The Escape Mapping for Higher Dimensional Systems

A collection of escape maps is shown in Figures 6.5 and 6.6 for interesting parameters of $t = 1.1$ and $\tau = -.9$, $a = .01$. The $p - q$ escape map is obtained by iterating a grid of 400×400 initial conditions in the $p - q$ plane coupled with a chosen point in the $P - Q$ plane. To obtain a picture of the full four-dimensional space, the (P, Q) can then be varied, usually in real time due to the computational speedup of the GPU. As an example, the six plates in Figure 6.5 correspond to (p, q, P, Q), where (p, q) are the coordinates in the visible sub-plane, and $(P, Q$ takes on the values [(0,0), (.1,.1), (.2,.2), (.6,.6), (.7,.7), (.9,.9)]. A similar $P - Q$ escape map is shown in Figure 6.6 for the $p - q$ values of [(([(0,0), (.1,.1), (.2,.2), (.3,.3), (.8,.8), (.9,.9)]. Note the resemblance of the escape maps to the respective phase portraits of earlier chapters.

6.3 Toward Real-Time Frequency Maps

One of the chief advantages of the escape time procedure or “escape mapping” is the computational speedup provided by a GPU implementation. In contrast, generating a frequency map (Figures 4.2 and 4.7) takes several orders of magnitude longer and provides less information about the long term stability of orbits. Here, we coupled the method of frequency analysis

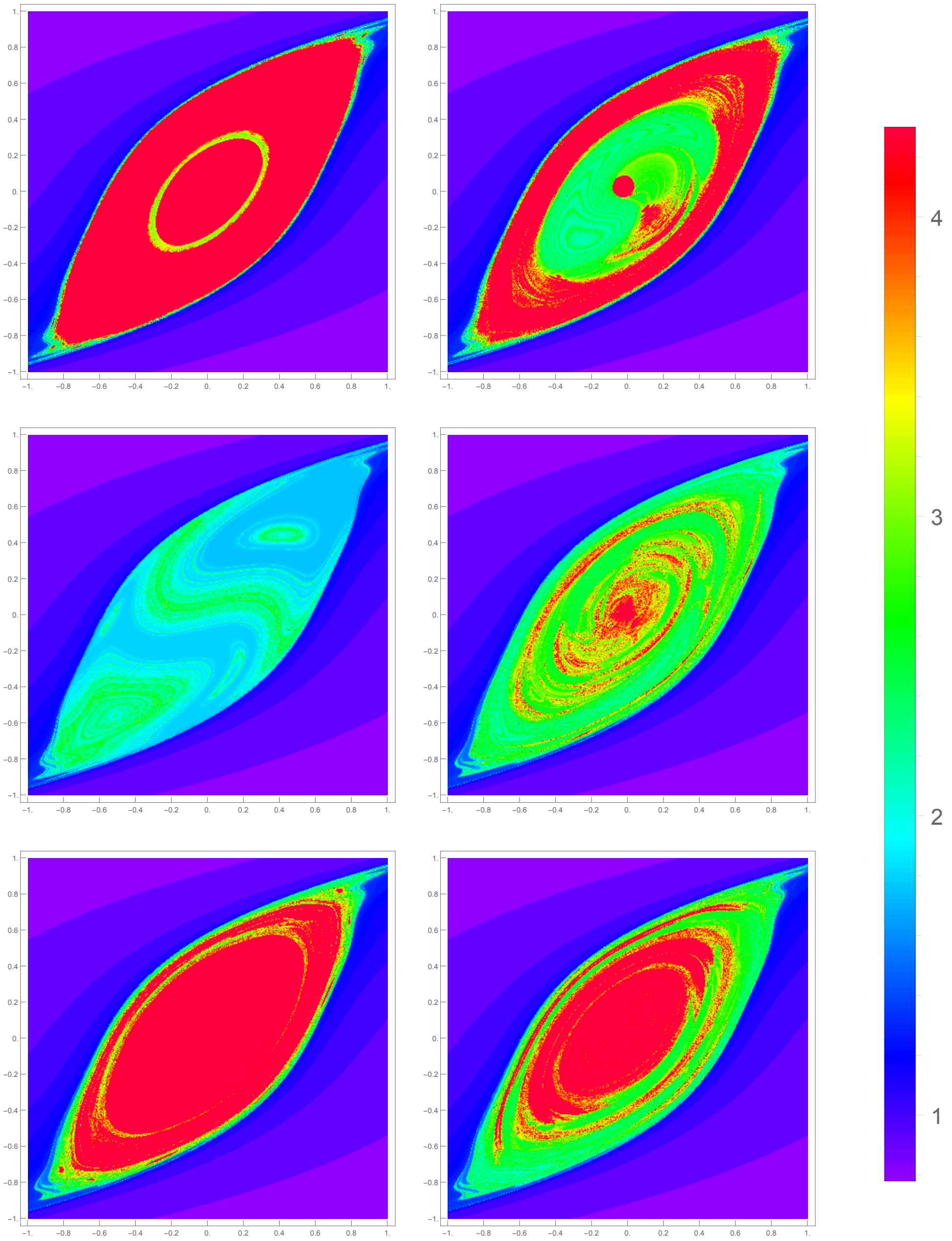

Figure 6.5: Escape map sections for the cubic-quadratic. A collection of escape maps for interesting parameters of $t = 1.1$ and $\tau = -.9$, $a = .01$. The $p - q$ sub-plane section is shown; each panel corresponds to a different (Q,P) value. Numbers in the legend indicate Log_{10} of the escape time.

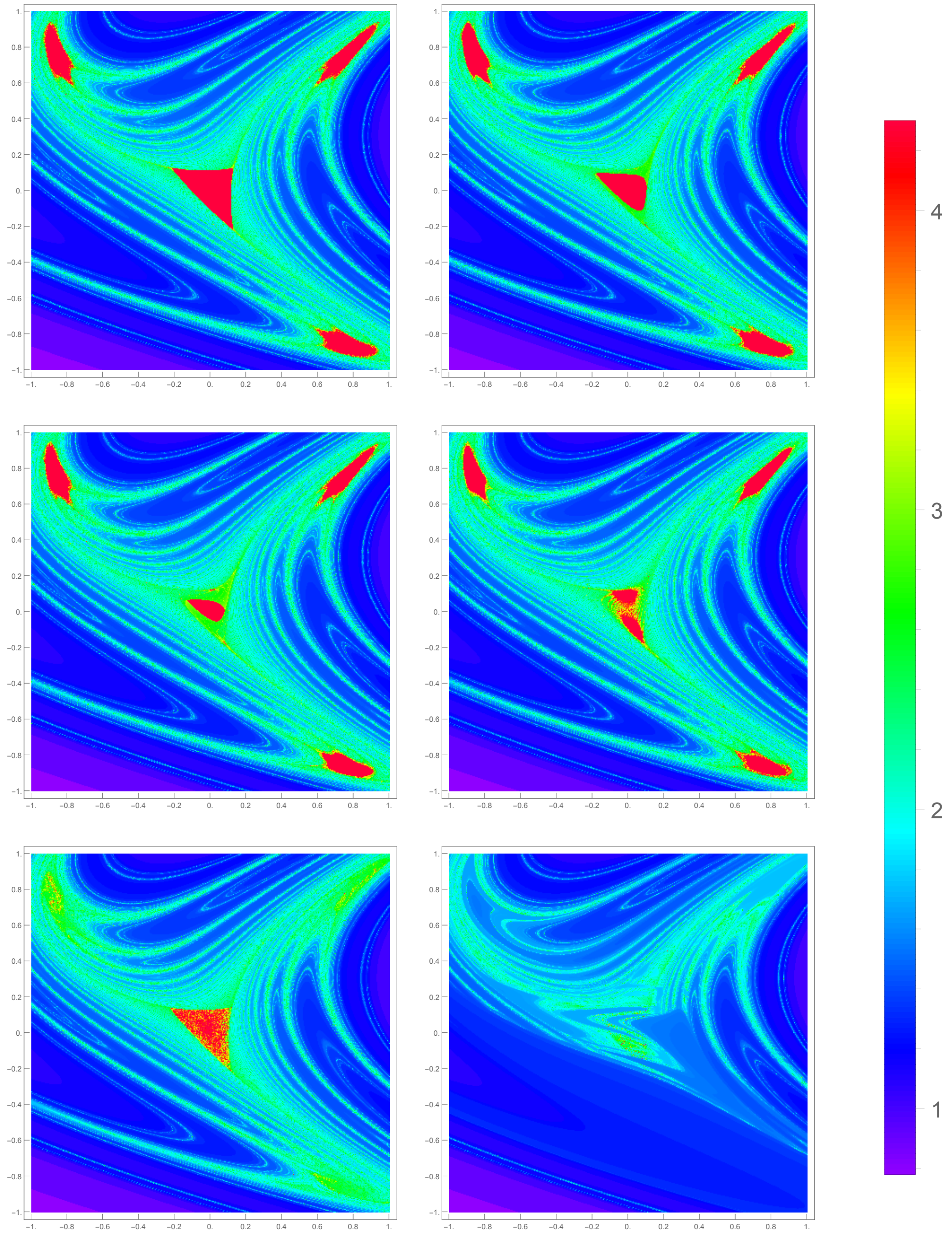

Figure 6.6: Escape map sections for the cubic-quadratic. A collection of escape maps The $P-Q$ sub-plane section is shown. Numbers in the legend indicate Log_{10} of the escape time.

with the exit times to provide a deeper picture of the dynamics. Figure 6.11 contains the results for a range of the coupling parameter a (cf. Figure 4.7). Essentially, we superimpose the exit times on top of the uncoupled Arnol'd Web (it is possible to use the frequency maps for larger a). Comparing Figure 4.7 to Figure 6.11 demonstrates that it may be possible to obtain qualitatively similar information about the dynamics of the system in real time from an exit time analysis as from the frequency map. In Figure 6.12, we simply plot the escape times obtained from the initial conditions used to generate the frequency maps shown in Figure 4.7 without superimposing them on top of the Arnol'd Web.

6.4 Comparing the Frequency and Escape Mappings

As discussed in Chap. 4, the accuracy of the frequency analysis method is usually around $1/T^4$, where T is the number of data points. Further, we have demonstrated that 2^{20} (1,048,576) iterations are necessary to accurately determine a frequency to nineteen decimals for the integrable Standard Map (Table 4.1, Chap. 4).

When looking for evidence of Arnol'd Diffusion and in general investigations of stability, long term behavior is of paramount importance. "Long-term" in many cases, means 10^9 or greater [9, 75] even 10^{15} which is beyond current practical reaches of computing. A modern CPU performs approximately 10^9 cycles per second. Since iterating one initial condition is a serial operation, and numerous floating point operations (FLOPs) are required for even a simple map, iterating for 10^9 and returning the result[1] requires around one second of real time at best. In reality, we find that 10^8 iterations of the coupled 4D map requires around one second. Thus, it would take 10^7 seconds or around 110 days to iterate one initial condition for 10^{15}. Although it is common for supercomputer users to leverage up to 1,000 or even 10,000 cores, this still only results in one small part of the parameter space available to the system.

For example, to obtain the escape maps obtained in this chapter, 16,000 initial conditions were iterated for up to 10^5, and this is at the lower end of the computational capabilities available; we typically iterate 16,000 initial conditions for 10^7 in real time on the GPU of a personal workstation. The convenience of quickly computing a massive number of orbits for "long-time" scales allows greater insight into the structure of phase space.

---

[1] Recording the data to a file or translating the data into a graphical representation which is directly displayed onscreen; either way, this takes time.

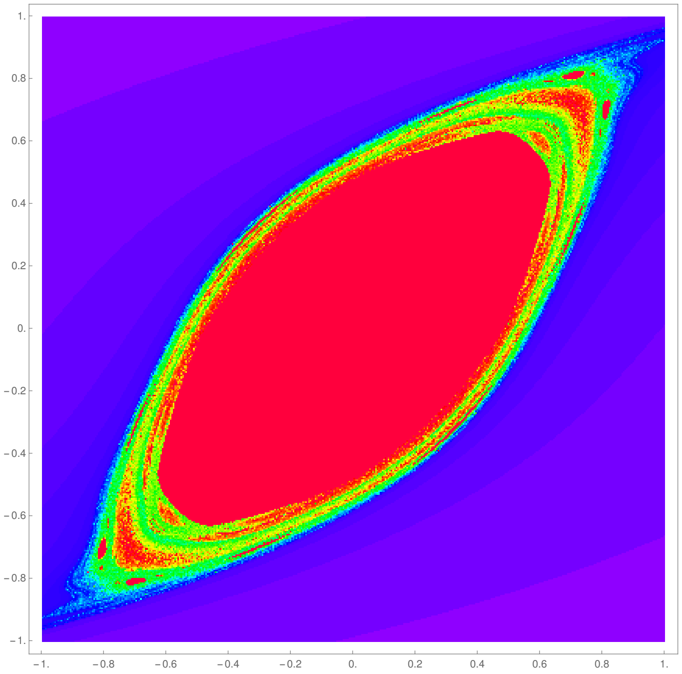

(a) Single Precision

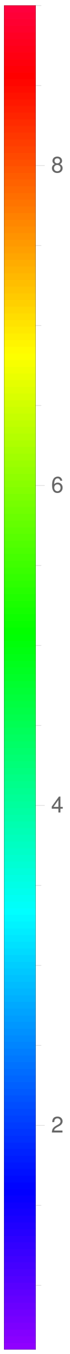

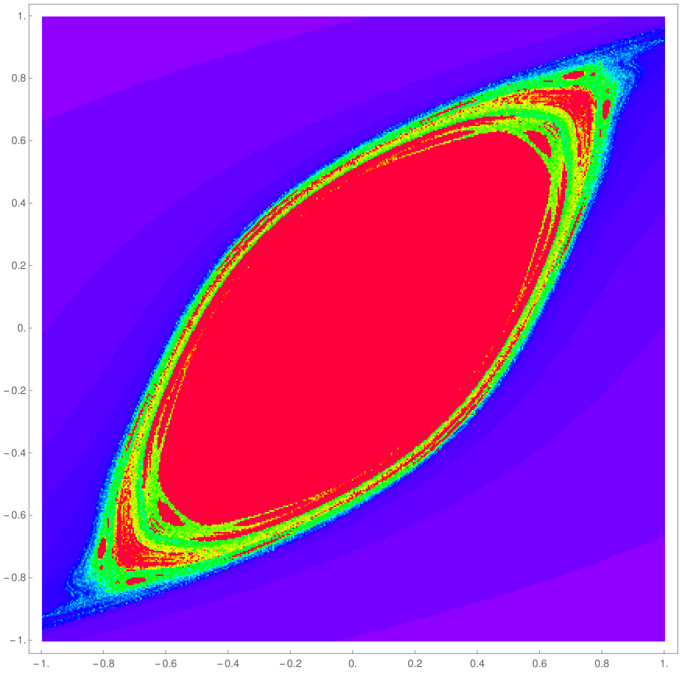

(b) Double Precision

Figure 6.7: Single vs. double precision Form$_2$ (I). Numbers in the legend indicate Log_{10} of the escape time.

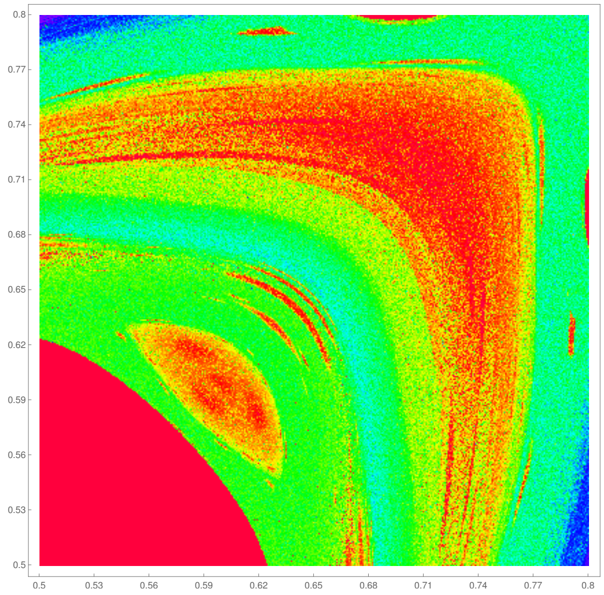

(a) Single Precision

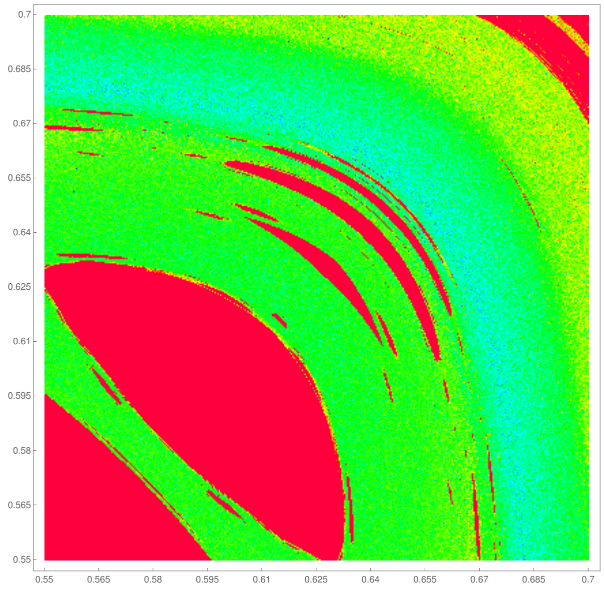

(b) Double Precision

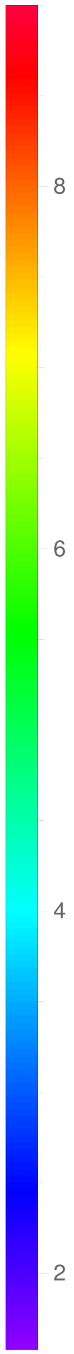

Figure 6.8: Single vs. double precision Form_2 (II). Zoom of the previous figure. Note the difference in the axes between top and bottom, but particularly the difference between orbits.

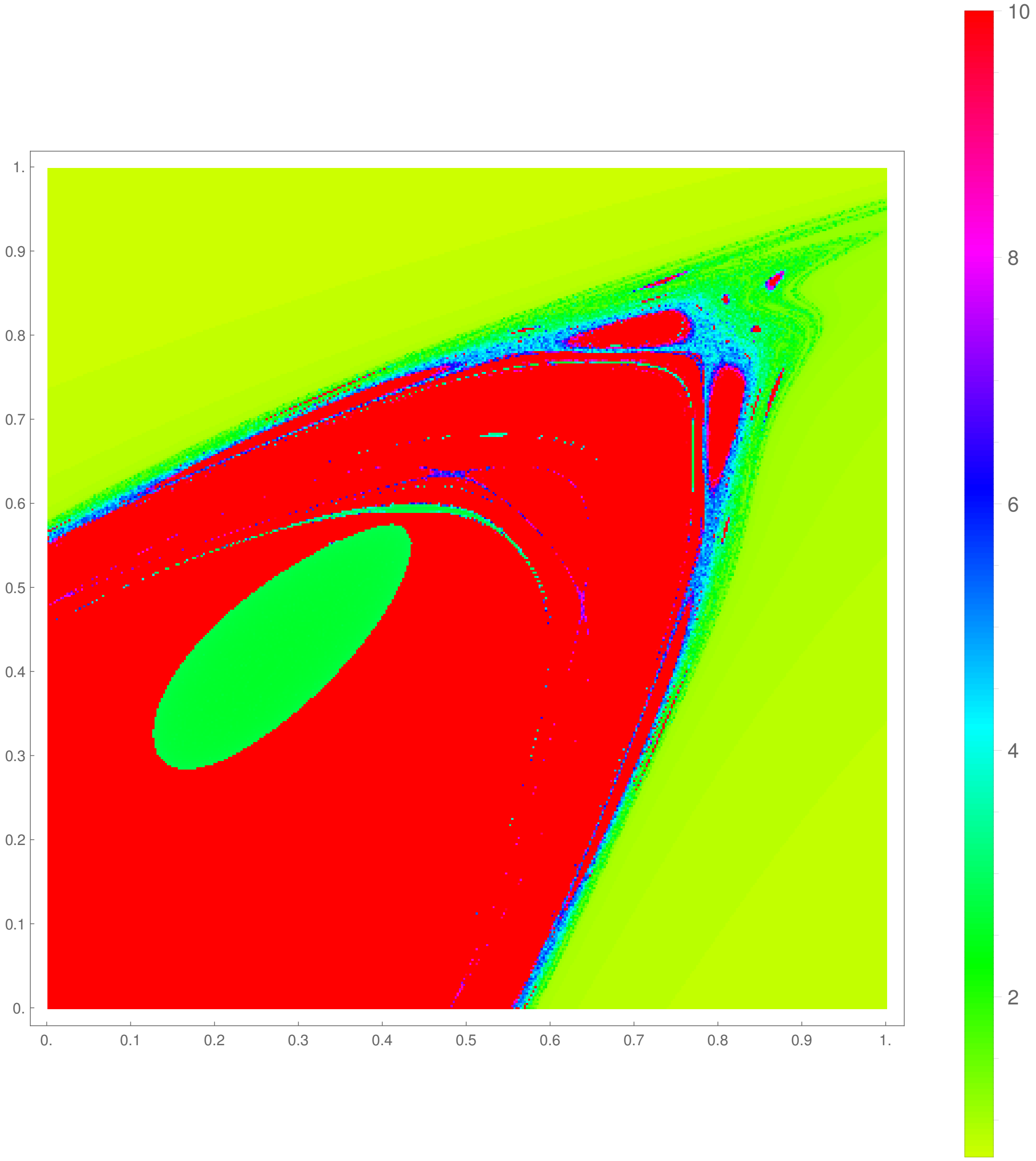

Figure 6.9: Exploring the structure of phase space (I). Numbers in the legend indicate Log_{10} of the escape time for Form_1 of the mapping. Although we find stable orbits up to 10^{13}, here we obtain a more general picture of the phase space by iterating 16,000 initial condition in the $p-q$ plane corresponding to $(p, q, 0, 0)$ and $a = 0.008$.

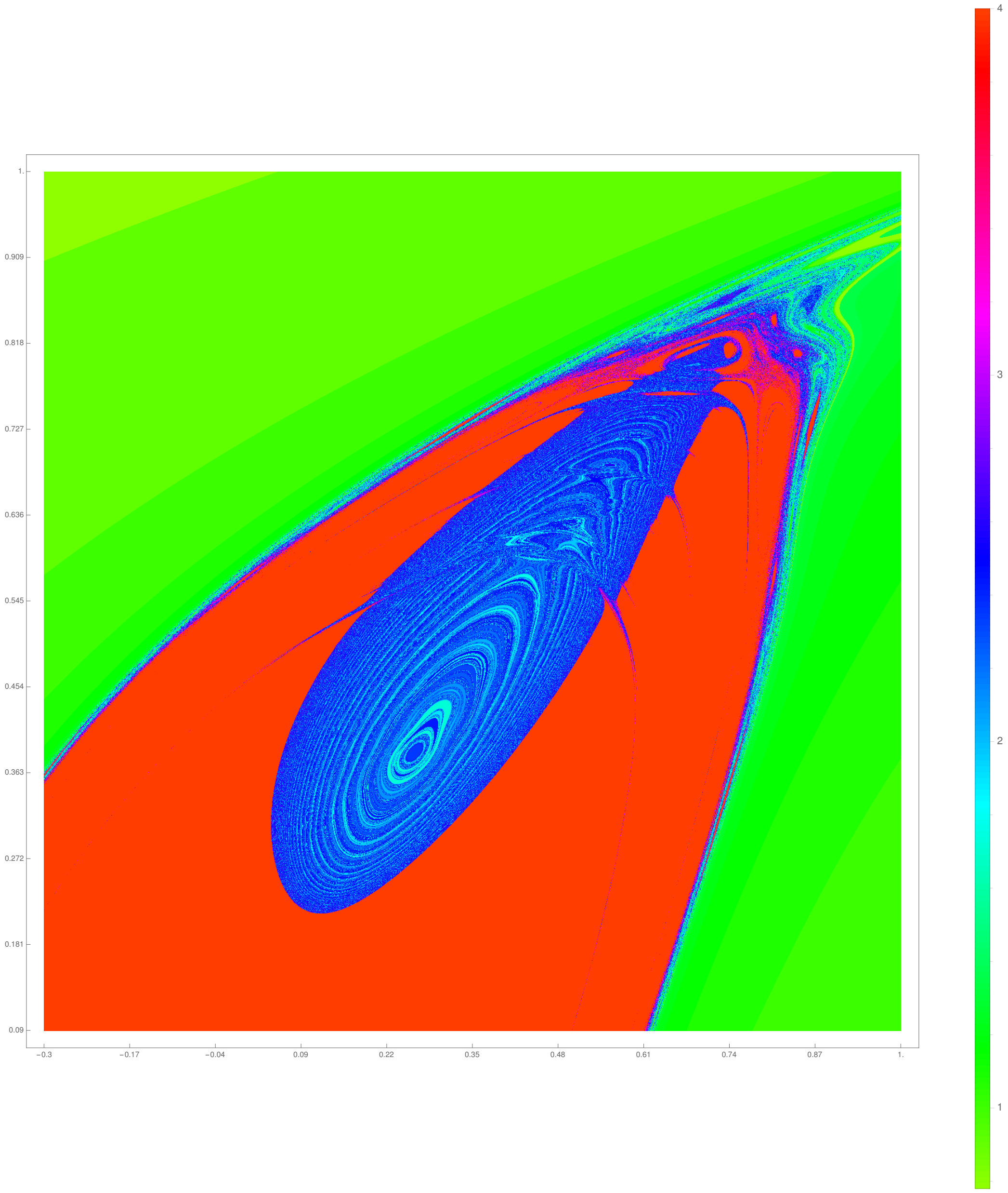

Figure 6.10: Exploring the structure of phase space (II). Results were obtained as in Figure 6.9. By exploring different time scales, different structures are observed in the sub-plane. This case is likely the result of strong resonance overlap (cf. Figures 6.5 and 6.6)

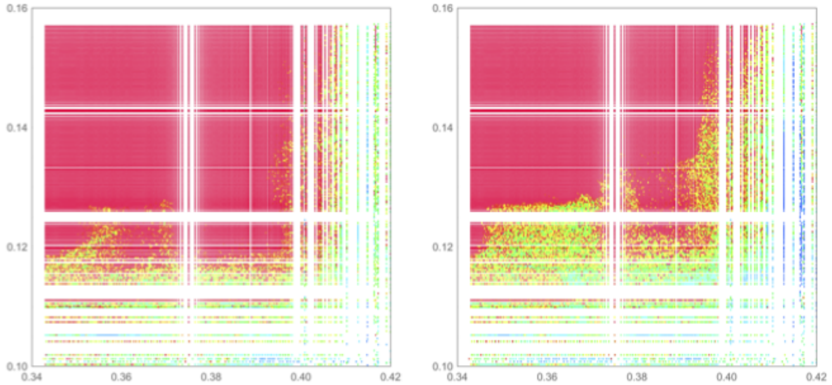

(a) a = 0.01 (b) a = 0.025

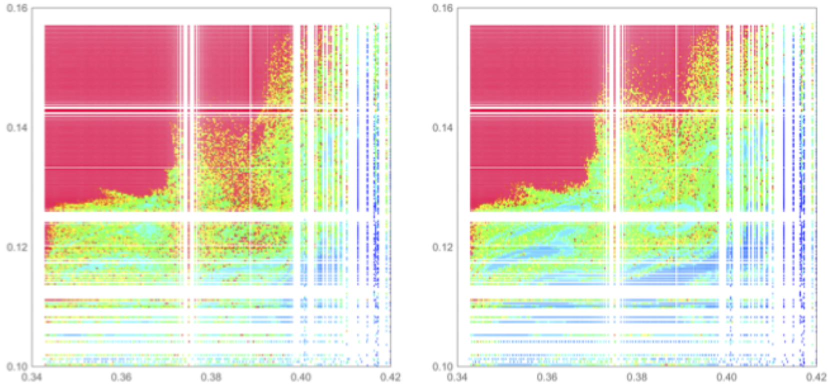

(c) a = 0.05 (d) a = 0.075

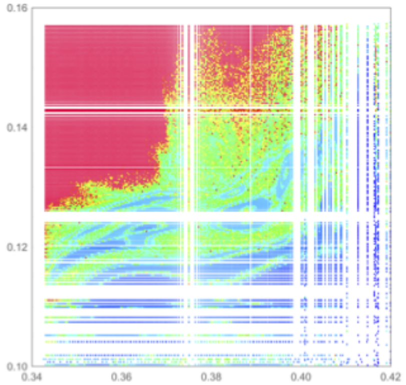

(e) a = 0.1

Figure 6.11: Escape times of the frequency map (I). Maximum time is 10^4; color scale is similar to other legends in this chapter.

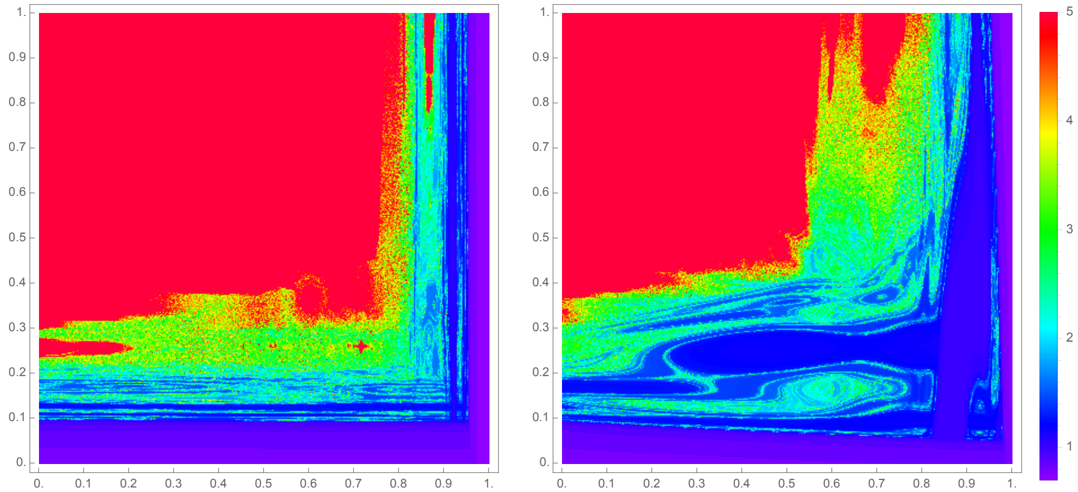

(c) a = 0.01 (d) a = 0.1

Figure 6.12: Escape times of the frequency map (II). The exit times of the initial conditions of the frequency map are plotted without the Arnol'd Web superimposition (see text).

Chapter 7

Conclusion and Summary of Results

In Chap. 1, we introduced Hamiltonian Dynamics, the KAM theory, and symplectic mappings. Hamiltonian systems fall into two categories, integrable and non-integrable, and in fact integrable systems are the exception. However, integrable systems provide a natural starting point, and illustrate fundamental properties of the dynamcis in phase space, such as motion on invariant tori and frequencies on the torus. Natural questions arise concerning the stabilty of non-integrable systems. The KAM (Kolmogorov, Arnol'd, and Moser) theory [68, 4, 108] guarantees the survival of invariant tori that for Hamiltonian systems subject to sufficiently small perturbations. Arnol'd [5] described a type of instability that arises from the merging of stochastic regions into a single, connected web that permeates all of phase space. This is the Arnol'd Web, and the motion that can occur in higher dimensional phase spaces due to its existence is the Arnol'd Diffusion [134, 135, 18, 126, 116, 82]. In two dimensions, invariant tori divide the phase space, but in higher dimensions, stochastic trajectories can undergo motion around tori due to the additional dimensionality. Symplectic mappings (surfaces of section) are used to study dynamical systems due to their theoretical and computational advantages. Many mathematical results exist concerning symplectic maps, and maps are computationally less expensive to iterate than a full set of differential equations while still retaining the essential feautres of the dynamics. The Standard Mapping (also known as the Chirikov-Taylor Mapping [18, 98, 99, 42]) is analyzed to illustrate the fundamental properties of mappings. The Froeschle Map [29, 33, 76, 63], essentially two coupled inverse standard mappings, is used to demonstrate the complicated pictures of dynamics that can emerge from higher dimensional mappings.

In Chap. 2, we defined different types of stability in dynamical systems and introduced the concept of Negative Energy Modes (NEMs) [101, 137, 103, 71, 73, 90, 102, 106, 22, 43]. These are modes of oscillations that are driven unstable by the dissipation of energy. NEMs occur in fluids and plasmas from wave-wave resonance, such as the three-wave problem, in mechanical systems with gyroscopic forces, and in the dynamics governing the motion of particles in magnetic fields. To illustrate the concept, we introduced Cherry's Hamiltonian [17] and discussed its relevance to the wave-wave and three wave problems of plasma physics [137, 70, 70, 71].

The coupled Cubic-Quadratic Mapping was derived in Chap. 3 by coupling the symplectic (area-preserving) two-dimensional cubic and quadratic mappings with a linear coupling. We derive the mapping via a type 1 generating function and write down two equivalent forms of the mapping which are used throughout this work. Hénon [51] derived a one-parameter form for the simplest general quadratic mapping. We revisit the simplest quadratic mapping and use the result of [24, 25] that any polynomial mapping may be put into a generalized polynomial form to demonstrate that the cubic map is in fact, a special case of the simplest general cubic mapping. Chapter 3 concludes with a brief discussion of the geometry of the higher dimensional phase space of the coupled mapping.

In Chap. 4, we introduced the method of frequency analysis and applied it to the standard, cubic, quadratic, and coupled cubic-quadratic mappings. We discussed the method of frequency analysis for dynamical systems [80, 77, 78, 76, 75, 74, 127] and a method recently introduced by Gomez et al. [39, 40]. Using Gomez's method, we constructed the frequency map for various cases of the coupled cubic-quadratic, and used it to demonstrate the existence of orbits with constant (to the degree of numerical accuracy) frequencies, something we would expect to see for orbits that lie on invariant tori. The existence of invariant tori is central to the idea of motion around tori in higher dimensions.

Also in Chap. 4, we examined the different types of orbits that occur in a four-dimensional mapping and plotted the frequencies obtained via the FFT method. Diffusion in the frequency space was observed.

Chapter 5 introduced the data analysis and visualization of the higher-dimensional phase space of the coupled cubic-quadratic mapping. We use the open source software package GGOBI to obtain preliminary results for a projection matrix that unwinds the complicated pictures in the usual $p_i - q_i$ sub-planes that emerge upon coupling. On a torus, there should be a perspective in four-space that reveals simple, closed curves with constant frequencies in the sub-planes. We use the preliminary data from GGOBI to solve the symplectic condition for a canonical transformation for the remaining coefficients of a projection matrix. We then apply the projection matrix and demonstrate that the tori are “unwound” by the transformation, revealing simple, closed curves in appropriate sub-planes. This is good evidence of the existence of tori, a requirement for the Arnol’d Diffusion.

Additionally in Chap. 5, we use the Poincaré surface of section technique for the four-dimensional mapping to demonstrate the existence of simple, closed curves. We obtain a simple, closed curve in the surface of section that closely resembles the uncoupled orbit in the usual $P - Q$ sub-plane.

Further methods to investigate the stability of orbits and transport phenomena in higher dimensional systems were introduced in Chap. 6. We use the escape times [64, 97, 100, 91] of the map to color different initial conditions in the sub-planes. This method is an improvement in some ways to the method of frequency analysis, as it allows us to manipulate the parameters and initial conditions of the mapping in real time to obtain new insights into the structure of phase space. Additionally, while the frequency method can only reveal stability over the time of the analysis (typically only a few hundred or few thousand iterations), tracking the escape time of orbits allows us to gain insight into stabilty over long time scales ($10^{10} - 10^{12}$). Further, since the escape time procedure is a massively parallel computing task, it can be easily implemented on an ordinary graphics processing unit

(GPU) that is common to modern computers. GPUs typically are capable of hundreds of GigaFLOPs or TeraFLOPS, while CPUs manage only around 25 GigaFLOPS when all cores are utilized. The GPU implementation allows real-time investigation of the phase space. In real-time, we can typically manipulate 16,000 initial conditions for up to 10^8 iterations. This is not possible with CPUs unless hundreds if not thousands of cores are involved; even with supercomputer resources, the problem of collating and visualizing the data in real-time remains.

Bibliography

[1] SS Abdullaev, KH Finken, M Jakubowski, and M Lehnen. Mappings of stochastic field lines in poloidal divertor tokamaks. *Nuclear Fusion*, 46(4):S113, 2006.

[2] Ralph Abraham and Jerrold E Marsden. *Foundations of Mechanics.* Benjamin/Cummings Publishing Company, 1978.

[3] Edward Anderson, Zhaojun Bai, Christian Bischof, Susan Blackford, Jack Dongarra, Jeremy Du Croz, Anne Greenbaum, Sven Hammarling, A McKenney, and D Sorensen. *LAPACK Users' Guide*, volume 9. Siam, 1999.

[4] Vladimir I Arnol'd. Proof of a theorem of A.N. Kolmogorov on the invariance of quasi-periodic motions under small perturbations of the hamiltonian. *Russian Mathematical Surveys*, 18(5):9–36, 1963.

[5] Vladimir I Arnold. Instability of dynamical systems with several degrees of freedom. *Soviet Mathematics*, 5:581–585, 1964.

[6] Vladimir Igorevich Arnol'd. Small denominators and problems of stability of motion in classical and celestial mechanics. *Russian Mathematical Surveys*, 18(6):85–191, 1963.

[7] Vladimir Igorevich Arnol'd. *Mathematical Methods of Classical Mechanics*. Springer Science and Business Media, 2013.

[8] David H Bailey, Roberto Barrio, and Jonathan M Borwein. High-precision computation: Mathematical physics and dynamics. *Applied Mathematics and Computation*, 218(20):10106–10121, 2012.

[9] Konstantin Batygin, Alessandro Morbidelli, and Matthew J Holman. Chaotic disintegration of the inner solar system. *The Astrophysical Journal*, 799(2):120, 2015.

[10] S Benkadda, S Kassibrakis, RB White, and GM Zaslavsky. Self-similarity and transport in the standard map. *Physical Review E*, 55(5):4909, 1997.

[11] Michael Victor Berry. Regular and irregular motion. In *AIP Conference proceedings*, volume 46, page 16, 1978.

[12] E.O. Brigham. *The Fast Fourier Transform and Its Applications*. Prentice Hall Englewood Cliffs, NJ, 1988.

[13] Ibere Luiz Caldas, Ricardo Luiz Viana, JD Szezech, Jefferson Stafusa Elias Portela, J Fonseca, Marisa Roberto, Caroline Gameiro Lopes Martins, and EJ Da Silva. Nontwist symplectic maps in tokamaks. *Communications in Nonlinear Science and Numerical Simulation*, 17(5):2021–2030, 2012.

[14] MP Calvo. *Numerical Hamiltonian Problems*. CRC Press, 1994.

[15] PJ Channell and C Scovel. Symplectic integration of Hamiltonian systems. *Nonlinearity*, 3(2):231, 1990.

[16] Q Chen, RS Mackay, and JD Meiss. Cantori for symplectic maps. *Journal of Physics A: Mathematical and General*, 23(21):L1093, 1990.

[17] T. M. Cherry. On periodic solutions of Hamiltonian systems of differential equations. *Philosophical Transactions of the Royal Society of London. Series A, Containing Papers of a Mathematical or Physical Character*, 227:137–221, 1928.

[18] Boris V Chirikov. A universal instability of many-dimensional oscillator systems. *Physics Reports*, 52(5):263–379, 1979.

[19] BV Chirikov. Resonance processes in magnetic traps. *Atomnaya Energ.*, 6, 1959.

[20] Pablo M. Cincotta. Arnol'd diffusion: An overview through dynamical astronomy. *New Astronomy Reviews*, 46(1):13–39, 2002.

[21] Robert Conte, Micheline Musette, and Caroline Verhoeven. Explicit integration of the Hénon-Heiles Hamiltonians. *Journal of Nonlinear Mathematical Physics*, 12(sup1):212–227, 2005.

[22] B Coppi, MN Rosenbluth, and RN Sudan. Nonlinear interactions of positive and negative energy modes in rarefied plasmas (I). *Annals of Physics*, 55(2):207–247, 1969.

[23] G Lejeune Dirichlet. Über die stabilität des gleichgewichts. *Journal für die reine und angewandte Mathematik*, 32:85–88, 1846.

[24] Wolfgang Engel. Ein satz über ganze Cremona-transformationen der ebene. *Mathematische Annalen*, 130(1):11–19, 1955.

[25] Wolfgang Engel. Ganze Cremona-transformationen von primzahlgrad in der ebene. *Mathematische Annalen*, 136(4):319–325, 1958.

[26] Laurent Fousse, Guillaume Hanrot, Vincent Lefèvre, Patrick Pélissier, and Paul Zimmermann. MPFR: A multiple-precision binary floating-point library with correct rounding. *ACM Transactions on Mathematical Software (TOMS)*, 33(2):13, 2007.

[27] Matteo Frigo and Steven G Johnson. The design and implementation of FFTW3. *Proceedings of the IEEE*, 93(2):216–231, 2005.

[28] C Froeschlé. Numerical study of dynamical systems with three degrees of freedom. II. Numerical displays of four-dimensional sections. *Astronomy and Astrophysics*, 5:177, 1970.

[29] C Froeschlé and J.-P. Scheidecker. Numerical study of a four-dimensional mapping. II. *Astronomy and Astrophysics*, 22:431, 1973.

[30] C Froeschlé and J.-P. Scheidecker. On the disappearance of isolating integrals in dynamical systems with more than two degrees of freedom. *Astrophysics and Space Science*, 25(2):373–386, 1973.

[31] Cl Froeschlé. Numerical study of dynamical systems with three degrees of freedom. I. Graphical displays of four-dimensional sections. *Astronomy and Astrophysics*, 4:115, 1970.

[32] Cl Froeschlé. A numerical study of the stochasticity of dynamical systems with two degrees of freedom. *Astronomy and Astrophysics*, 9:15, 1970.

[33] Cl Froeschlé. Numerical study of a four-dimensional mapping. *Astronomy and Astrophysics*, 16:172, 1972.

[34] Cl Froeschlé and E Lega. On the measure of the structure around the last kam torus before and after its break-up. *Celestial Mechanics and Dynamical Astronomy*, 64(1-2):21–31, 1996.

[35] Claude Froeschlé. On the number of isolating integrals in systems with three degrees of freedom. *Astrophysics and Space Science*, 14(1):110–117, 1971.

[36] Claude Froeschlé and Elena Lega. On the structure of symplectic mappings. The fast Lyapunov indicator: a very sensitive tool. In *New Developments in the Dynamics of Planetary Systems*, pages 167–195. Springer, 2001.

[37] Claude Froeschlé, Elena Lega, and Robert Gonczi. Fast Lyapunov indicators. Application to asteroidal motion. *Celestial Mechanics and Dynamical Astronomy*, 67(1):41–62, 1997.

[38] David Goldberg. What every computer scientist should know about floating-point arithmetic. *ACM Computing Surveys (CSUR)*, 23(1):5–48, 1991.

[39] Gerard Gómez, Josep–Maria Mondelo, and Carles Simó. A collocation method for the numerical Fourier analysis of quasi-periodic functions. I: Numerical tests and examples. *Discrete and Continuous Dynamical Systems - Series B*, 14(1):41–74, April 2010.

[40] Gerard Gómez, Josep-Maria Mondelo, and Carles Simó. A collocation method for the numerical Fourier analysis of quasi-periodic functions. II. Analytical error estimates. *Discrete Contin. Dyn. Syst. Ser. B*, 14(1):75–109, 2010.

[41] John M Greene. Two-dimensional measure-preserving mappings. *Journal of Mathematical Physics*, 9(5):760–768, 1968.

[42] John M Greene. A method for determining a stochastic transition. *Journal of Mathematical Physics*, 20(6):1183–1201, 1979.

[43] John M Greene and Bruno Coppi. Dissipative instability in mirror containment systems. *Physics of Fluids (1958-1988)*, 8(9):1745–1747, 1965.

[44] G Haller. Diffusion at intersecting resonances in Hamiltonian systems. *Physics Letters A*, 200(1):34–42, 1995.

[45] Stephen M Hammel, James A Yorke, and Celso Grebogi. Do numerical orbits of chaotic dynamical processes represent true orbits? *Journal of Complexity*, 3(2):136–145, 1987.

[46] Stephen M Hammel, James A Yorke, Celso Grebogi, et al. Numerical orbits of chaotic processes represent true orbits. *American Mathematical Society*, 19(2), 1988.

[47] Boris Hasselblatt and Anatole Katok. *A First Course in Dynamics: with a Panorama of Recent Developments*. Cambridge University Press, 2003.

[48] Robert HG Helleman. Dynamics revisited, a glossary. In *Topics in Nonlinear Dynamics: A Tribute to Sir Edward Bullard*, volume 46, pages 400–404. AIP Publishing, 1978.

[49] M Hénon. Exploration numérique du problème restreint. i. masses égales; orbites périodiques. In *Annales d'Astrophysique*, volume 28, page 499, 1965.

[50] M Hénon. Exploration numérique du problème restreint. ii. masses égales, stabilité des orbites périodiques. In *Annales d'Astrophysique*, volume 28, page 992, 1965.

[51] Michel Hénon. Numerical study of quadratic area-preserving mappings. *Quarterly of applied mathematics*, pages 291–312, 1969.

[52] Michel Hénon. A two-dimensional mapping with a strange attractor. *Communications in Mathematical Physics*, 50(1):69–77, 1976.

[53] Michel Hénon. Numerical exploration of Hamiltonian systems. *Chaotic Behavior of Deterministic Systems (Les Houches, 1981)*, pages 53–170, 1983.

[54] Michel Hénon and Carl Heiles. The applicability of the third integral of motion: some numerical experiments. *The Astronomical Journal*, 69:73, 1964.

[55] Philip Holmes. A nonlinear oscillator with a strange attractor. *Philosophical Transactions of the Royal Society of London A: Mathematical, Physical and Engineering Sciences*, 292(1394):419–448, 1979.

[56] Philip Holmes. Poincaré, celestial mechanics, dynamical-systems theory and "chaos". *Physics Reports*, 193(3):137–163, 1990.

[57] W Horton and Yoshi H Ichikawa. *Chaos and Structures in Nonlinear Plasmas*. World Scientific, 1996.

[58] JE Howard, AJ Lichtenberg, MA Lieberman, and RH Cohen. Four-dimensional mapping model for two-frequency electron cyclotron resonance heating. *Physica D: Nonlinear Phenomena*, 20(2-3):259–284, 1986.

[59] B Hu and JM Mao. Universal metric properties of an approximate Poincaré map for Duffing's equation with negative stiffness. *Physical Review A*, 27(3):1700, 1983.

[60] E Atlee Jackson. *Perspectives of Nonlinear Dynamics*, volume 1. Cambridge University Press, 1989.

[61] E Atlee Jackson. *Perspectives of Nonlinear Dynamics*, volume 2. Cambridge University Press, 1990.

[62] Jorge V José and Eugene J Saletan. *Classical Dynamics: A Contemporary Approach*. Cambridge University Press, 1998.

[63] Kunihiko Kaneko and Richard J Bagley. Arnol'd diffusion, ergodicity and intermittency in a coupled standard mapping. *Physics Letters A*, 110(9):435–440, 1985.

[64] Charles FF Karney. Long-time correlations in the stochastic regime. *Physica D: Nonlinear Phenomena*, 8(3):360–380, 1983.

[65] Charles FF Karney, Alexander B Rechester, and Roscoe B White. Effect of noise on the standard mapping. *Physica D: Nonlinear Phenomena*, 4(3):425–438, 1982.

[66] Anatole Katok and Boris Hasselblatt. *Introduction to the Modern Theory of Dynamical Systems*. Cambridge University Press, 1997.

[67] AN Kolmogorov. The general theory of dynamical systems and classical mechanics. In *Proc. Intl. Congress of Math., Amsterdam*, volume 1, pages 315–333, 1954.

[68] AN Kolmogorov. On conservation of conditionally periodic motions under small perturbations of the Hamiltonian. In *Dokl. Akad. Nauk SSSR*, volume 98, pages 527–530, 1954.

[69] Hyung-tae Kook and James D Meiss. Diffusion in symplectic maps. *Physical Review A*, 41(8):4143, 1990.

[70] Christopher Shane Kueny. *Nonlinear instability and chaos in plasma wave-wave interactions.* PhD thesis, 1993.

[71] CS Kueny and PJ Morrison. Nonlinear instability and chaos in plasma wave-wave interactions. I. Introduction. *Physics of Plasmas*, 2:1926–1940, 1995.

[72] CS Kueny and PJ Morrison. Nonlinear instability and chaos in plasma wave-wave interactions. II. Numerical methods and results. *Physics of Plasmas*, 2:4149, 1995.

[73] Horace. Lamb. *Hydrodynamics.* Dover publications, 1945.

[74] J Laskar et al. Frequency map analysis and particle accelerators. *Portland, PAC*, 3:378–382, 2003.

[75] Jacques Laskar. The chaotic motion of the solar system: A numerical estimate of the size of the chaotic zones. *Icarus*, 88(2):266–291, 1990.

[76] Jacques Laskar. Frequency analysis for multi-dimensional systems. Global dynamics and diffusion. *Physica D: Nonlinear Phenomena*, 67(1):257–281, 1993.

[77] Jacques Laskar. Frequency analysis of a dynamical system. *Celestial Mechanics and Dynamical Astronomy*, 56(1-2):191–196, 1993.

[78] Jacques Laskar. Introduction to frequency map analysis. In *Hamiltonian systems with three or more degrees of freedom*, pages 134–150. Springer, 1999.

[79] Jacques Laskar. Michel Hénon and the stability of the solar system. *arXiv preprint arXiv:1411.4930*, 2014.

[80] Jacques Laskar, Claude Froeschlé, and Alessandra Celletti. The measure of chaos by the numerical analysis of the fundamental frequencies. application to the standard mapping. *Physica D: Nonlinear Phenomena*, 56(2):253–269, 1992.

[81] Elena Lega, Massimiliano Guzzo, and Claude Froeschlé. Detection of Arnol'd diffusion in Hamiltonian systems. *Physica D: Nonlinear Phenomena*, 182(3):179–187, 2003.

[82] Allan J Lichtenberg and Michael A Lieberman. *Regular and Stochastic Motion*. Springer-Verlag New York, 1983.

[83] M. A. Lieberman. Arnol'd diffusion in Hamiltonian systems with three degrees of freedom. *Annals of the New York Academy of Sciences*, 357(1):119–142, 1980.

[84] MA Lieberman and Jeffrey L Tennyson. Chaotic motion along resonance layers in near-integrable hamiltonian systems with three or more degrees of freedom. In *Long-Time Prediction in Dynamics*, volume 1, page 179, 1983.

[85] Edward N Lorenz. Deterministic nonperiodic flow. *Journal of the Atmospheric Sciences*, 20(2):130–141, 1963.

[86] Aleksandr Mikhailovich Lyapunov. The general problem of the stability of motion. *International Journal of Control*, 55(3):531–534, 1992.

[87] R. S. MacKay. Greene's residue criterion. *Nonlinearity*, 5(1):161, 1992.

[88] Robert Sinclair MacKay. *Renormalisation in Area-Preserving Maps.* World Scientific Publishing Company Incorporated, 1993.

[89] RS MacKay, JD Meiss, and IC Percival. Transport in Hamiltonian systems. *Physica D: Nonlinear Phenomena*, 13(1-2):55–81, 1984.

[90] RS MacKay and PG Saffman. Stability of water waves. In *Proceedings of the Royal Society of London A: Mathematical, Physical and Engineering Sciences*, volume 406, pages 115–125. The Royal Society, 1986.

[91] Benoit B Mandelbrot. *The fractal geometry of nature*, volume 173. Macmillan, 1983.

[92] Caroline GL Martins, R Egydio De Carvalho, Ibere Luiz Caldas, and Marisa Roberto. The non-twist standard map with robust tori. *Journal of Physics A: Mathematical and Theoretical*, 43(17):175501, 2010.

[93] Caroline GL Martins, R Egydio De Carvalho, Ibere Luiz Caldas, and Marisa Roberto. Plasma confinement in tokamaks with robust torus. *Physica A: Statistical Mechanics and its Applications*, 390(5):957–962, 2011.

[94] Robert M. May. Simple mathematical models with very complicated dynamics. *Nature*, 261(5560):459–467, 1976.

[95] Robert M May and George F Oster. Bifurcations and dynamic complexity in simple ecological models. *American Naturalist*, pages 573–599, 1976.

[96] Edwin M McMillan. A problem in the stability of periodic systems. *Topics in modern physics, a tribute to EV Condon*, pages 219–244, 1971.

[97] James D Meiss. Average exit time for volume-preserving maps. *Chaos: An Interdisciplinary Journal of Nonlinear Science*, 7(1):139–147, 1997.

[98] JD Meiss. Symplectic maps, variational principles, and transport. *Reviews of Modern Physics*, 64(3):795, 1992.

[99] JD Meiss. Visual explorations of dynamics: The standard map. *Pramana*, 70(6):965–988, 2008.

[100] Michael Michelitsch and Otto E Rössler. A new feature in Hénon's map. *Computers and Graphics*, 13(2):263–265, 1989.

[101] Philip J Morrison and S Eliezer. Spontaneous symmetry breaking and neutral stability in the noncanonical hamiltonian formalism. *Physical Review A*, 33(6):4205, 1986.

[102] P.J. Morrison. The free energy principle and negative energy waves. *Invited Talk, UC-Berkeley*, 1987.

[103] P.J. Morrison. Hamiltonian description of an ideal fluid. *Reviews of Modern Physics*, 70(2), 1998.

[104] PJ Morrison. Magnetic field lines, Hamiltonian dynamics, and nontwist systems. *Physics of Plasmas*, 7(6):2279–2289, 2000.

[105] P.J. Morrison. Deterministic dynamics. Unpublished Lecture Notes, 2016.

[106] PJ Morrison and M Kotschenreuther. The Free Energy Principle, Negative Energy Modes, and Stability (IFSR no. 280). Institute for

Fusion Studies, The University of Texas at Austin, Austin, TX (USA). 1989.

[107] PJ Morrison and M Kotschenreuther. The free energy principle, negative energy modes, and stability. In *Nonlinear world*. 1990.

[108] Jürgen Moser. On invariant curves of area-preserving mappings of an annulus. *Nachr. Akad. Wiss. Göttingen, II*, pages 1–20, 1962.

[109] Jürgen Moser. Convergent series expansions for quasi-periodic motions. *Mathematische Annalen*, 169(1):136–176, 1967.

[110] Jürgen Moser. *Lectures on Hamiltonian systems.* Number 81. American Mathematical Soc., 1968.

[111] Jürgen Moser. *Stable and Random Motions in Dynamical Systems: with Special Emphasis on Celestial Mechanics.* Princeton University Press, 1973.

[112] Jürgen Moser. Nearly integrable and integrable systems. In *Topics in Nonlinear Dynamics: A Tribute to Sir Edward Bullard*, volume 46, pages 1–15. AIP Publishing, 1978.

[113] Jürgen Moser. Monotone twist mappings and the calculus of variations. *Ergodic Theory and Dynamical Systems*, 6(03):401–413, 1986.

[114] Nikolai Nikolaevich Nekhoroshev. Behavior of Hamiltonian systems close to integrable. *Functional Analysis and Its Applications*, 5(4):338–339, 1971.

[115] Nikolai Nikolaevich Nekhoroshev. An exponential estimate of the time of stability of nearly-integrable Hamiltonian systems. *Russian Mathematical Surveys*, 32(6):1–65, 1977.

[116] Edward Ott. *Chaos in Dynamical Systems.* Cambridge university press, 2002.

[117] Adrian Patrascioiu. The ergodic-hypothesis: a complicated problem in mathematics and physics. *Los Alamos Science*, 15:263–279, 1987.

[118] Ian C Percival and Derek Richards. *Introduction to Dynamics.* Cambridge University Press, 1982.

[119] E Pina and L Jiménez Lara. On the symmetry lines of the standard mapping. *Physica D: Nonlinear Phenomena*, 26(1-3):369–378, 1987.

[120] Henri Poincaré. *Les méthodes nouvelles de la mécanique céleste: Méthodes de MM. Newcomb, Glydén, Lindstedt et Bohlin. 1893*, volume 2. Gauthier-Villars it fils, 1893.

[121] Henri Poincaré. *New Methods of Celestial Mechanics.* Springer Science and Business Media, 1992.

[122] Jürgen Pöschel. A lecture on the classical KAM theorem. *Proceedings Symp Pure Math*, 2009.

[123] F Rannou. Numerical study of discrete plane area-preserving mappings. *Astronomy and Astrophysics*, 31:289, 1974.

[124] S Neil Rasband. *Chaotic dynamics of nonlinear systems.* Courier Dover Publications, 2015.

[125] AB Rechester and Roscoe B White. Calculation of turbulent diffusion for the Chirikov-Taylor model. *Physical Review Letters*, 44(24):1586, 1980.

[126] Linda E Reichl. *The Transition to Chaos in Conservative Classical Systems: Quantum Manifestations.* Springer Verlag, 1992.

[127] Philippe Robutel and Jacques Laskar. Frequency map and global dynamics in the solar system i: Short period dynamics of massless particles. *Icarus*, 152(1):4–28, 2001.

[128] Shawn C Shadden, Francois Lekien, and Jerrold E Marsden. Definition and properties of lagrangian coherent structures from finite-time lyapunov exponents in two-dimensional aperiodic flows. *Physica D: Nonlinear Phenomena*, 212(3):271–304, 2005.

[129] Carl L Siegel and Jürgen K Moser. *Lectures on Celestial Mechanics.* Springer Verlag, 1971.

[130] Deborah F. Swayne, Duncan Temple Lang, Andreas Buja, and Dianne Cook. GGobi: evolving from XGobi into an extensible framework for interactive data visualization. *Computational Statistics & Data Analysis*, 43:423–444, 2003.

[131] J. D. Szezech, I. L. Caldas, S. R. Lopes, R. L. Viana, and P. J. Morrison. Transport properties in nontwist area-preserving maps. *Chaos: An Interdisciplinary Journal of Nonlinear Science*, 19(4):043108, 2009.

[132] JD Szezech, AB Schelin, IL Caldas, SR Lopes, PJ Morrison, and RL Viana. Finite-time rotation number: A fast indicator for chaotic dynamical structures. *Physics Letters A*, 377(6):452–456, 2013.

[133] JD Szezech Jr, Ibere Luiz Caldas, Sergio Roberto Lopes, PJ Morrison, and Ricardo Luiz Viana. Effective transport barriers in nontwist systems. *Physical Review E*, 86(3):036206, 2012.

[134] J. L. Tennyson, M. A. Lieberman, and A. J. Lichtenberg. Diffusion in near-integrable Hamiltonian systems with three degrees of freedom. In *AIP Conference Proceedings*, volume 57, page 272, 1980.

[135] Jeffrey Tennyson. Resonance transport in near-integrable systems with many degrees of freedom. *Physica D: Nonlinear Phenomena*, 5(1):123–135, 1982.

[136] GR Wang, B Hu, and SG Chen. Arnol'd diffusion in a four-dimensional standard map. *Physics Letters A*, 151(1):37–42, 1990.

[137] Jan Weiland and Hans Wilhelmsson. *Coherent Non-Linear Interaction of Waves in Plasmas*. Pergamon Press, New York, 1977.

[138] Edmund Taylor Whittaker. *A Treatise on the Analytical Dynamics of Particles and Rigid Bodies*. Cambridge University Press, 1988.

[139] Jack Wisdom. The origin of the Kirkwood gaps - A mapping for asteroidal motion near the 3/1 commensurability. *The Astronomical Journal*, 87:577–593, 1982.

[140] Jack Wisdom. Chaotic behavior and the origin of the 3/1 Kirkwood gap. *Icarus*, 56(1):51–74, 1983.

[141] Blake P Wood, Allan J Lichtenberg, and Michael A Lieberman. Arnol'd diffusion in weakly coupled standard maps. *Physical Review A*, 42(10):5885, 1990.

[142] Y Yamaguchi and N Mishima. Fractal basin boundary of a two-dimensional cubic map. *Physics Letters A*, 109(5):196–200, 1985.